US 20050251039A1

(19) United States

(12) Patent Application Publication (10) Pub. No.: US 2005/0251039 A1

Chalana et al. (43) Pub. Date: Nov. 10, 2005

(54) 3D ULTRASOUND-BASED INSTRUMENT FOR NON-INVASIVE MEASUREMENT OF AMNIOTIC FLUID VOLUME

(76) Inventors: **Vikram Chalana**, Mill Creek, WA (US); **Stephen Dudycha**, Bothell, WA (US); **Gerald McMorrow**, Kirkland, WA (US)

Correspondence Address:
**BLACK LOWE & GRAHAM, PLLC**
**701 FIFTH AVENUE**
**SUITE 4800**
**SEATTLE, WA 98104 (US)**

(21) Appl. No.: **11/119,355**

(22) Filed: **Apr. 29, 2005**

**Related U.S. Application Data**

(63) Continuation-in-part of application No. 10/701,955, filed on Nov. 5, 2003, which is a continuation-in-part of application No. 10/443,126, filed on May 20, 2003. Continuation-in-part of application No. PCT/US03/24368, filed on Aug. 1, 2003. Continuation-in-part of application No. PCT/US03/14785, filed on May 9, 2003, which is a continuation of application No. 10/165,556, filed on Jun. 7, 2002, now Pat. No. 6,676,605. Continuation-in-part of application No. 10/633,186, filed on Jul. 31, 2003.

(60) Provisional application No. 60/566,823, filed on Apr. 30, 2004. Provisional application No. 60/423,881, filed on Nov. 5, 2002. Provisional application No. 60/400,624, filed on Aug. 2, 2002. Provisional application No. 60/423,881, filed on Nov. 5, 2002. Provisional application No. 60/423,881, filed on Nov. 5, 2002. Provisional application No. 60/400,624, filed on Aug. 2, 2002.

**Publication Classification**

(51) **Int. Cl.**[7] ..... **A61B 5/00**; A61B 8/00; A61B 8/12; A61B 8/14

(52) **U.S. Cl.** ..... **600/437**

(57) **ABSTRACT**

A hand-held 3D ultrasound instrument is disclosed which is used to non-invasively and automatically measure amniotic fluid volume in the uterus requiring a minimum of operator intervention. Using a 2D image-processing algorithm, the instrument gives automatic feedback to the user about where to acquire the 3D image set. The user acquires one or more 3D data sets covering all of the amniotic fluid in the uterus and this data is then processed using an optimized 3D algorithm to output the total amniotic fluid volume corrected for any fetal head brain volume contributions.

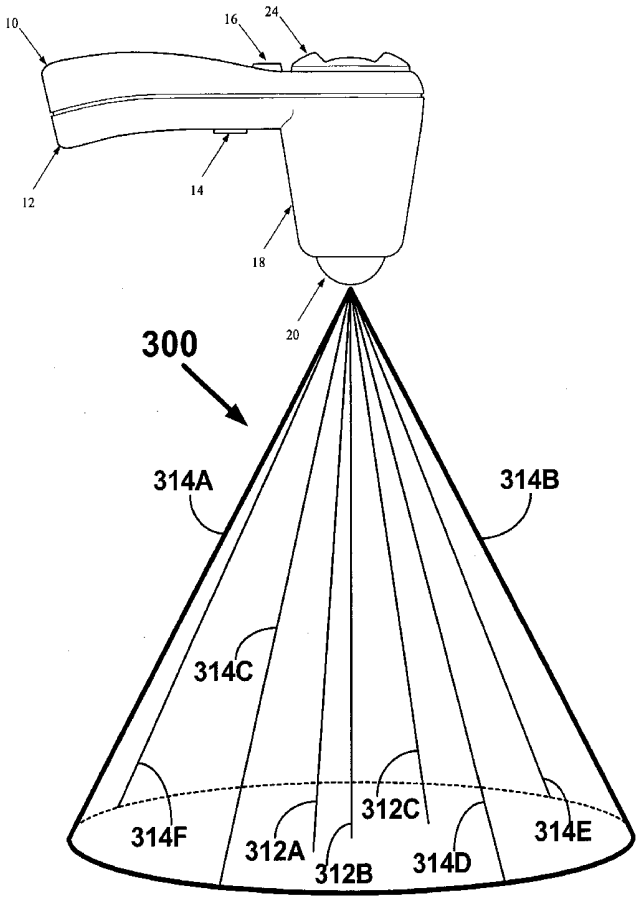

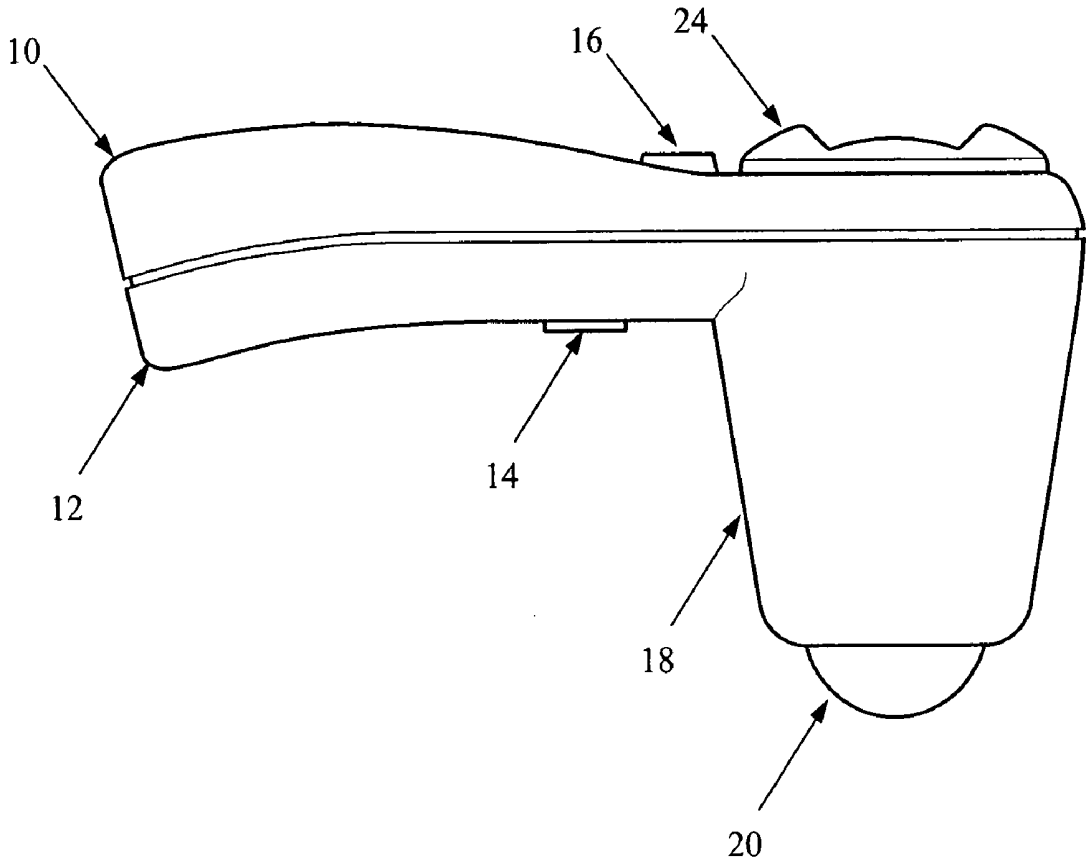


FIG. 1

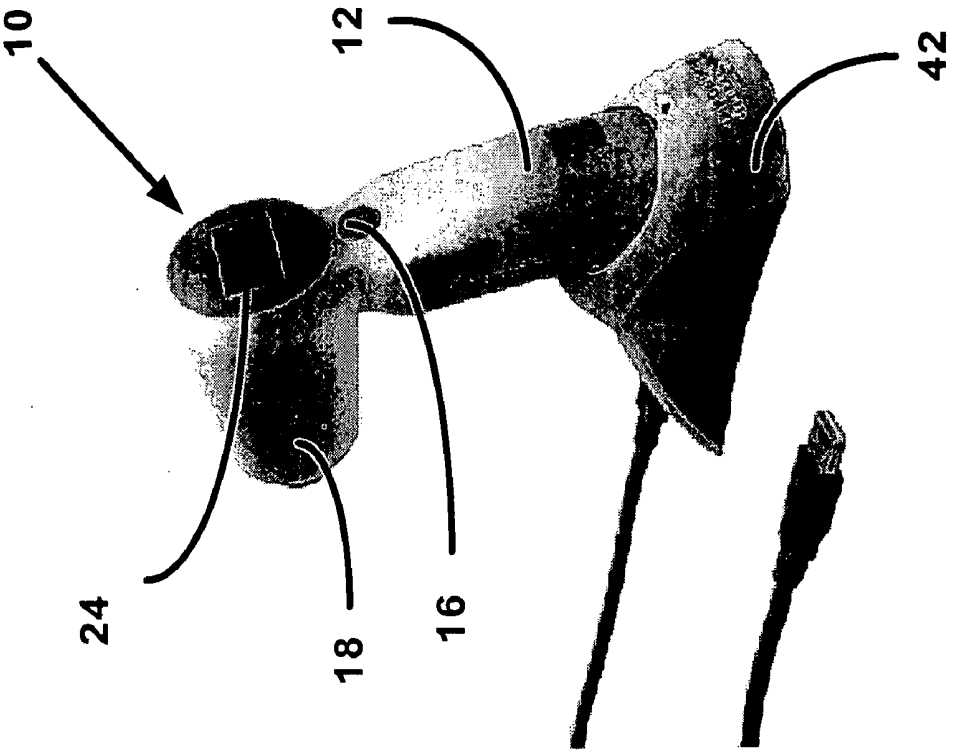


FIG. 2B

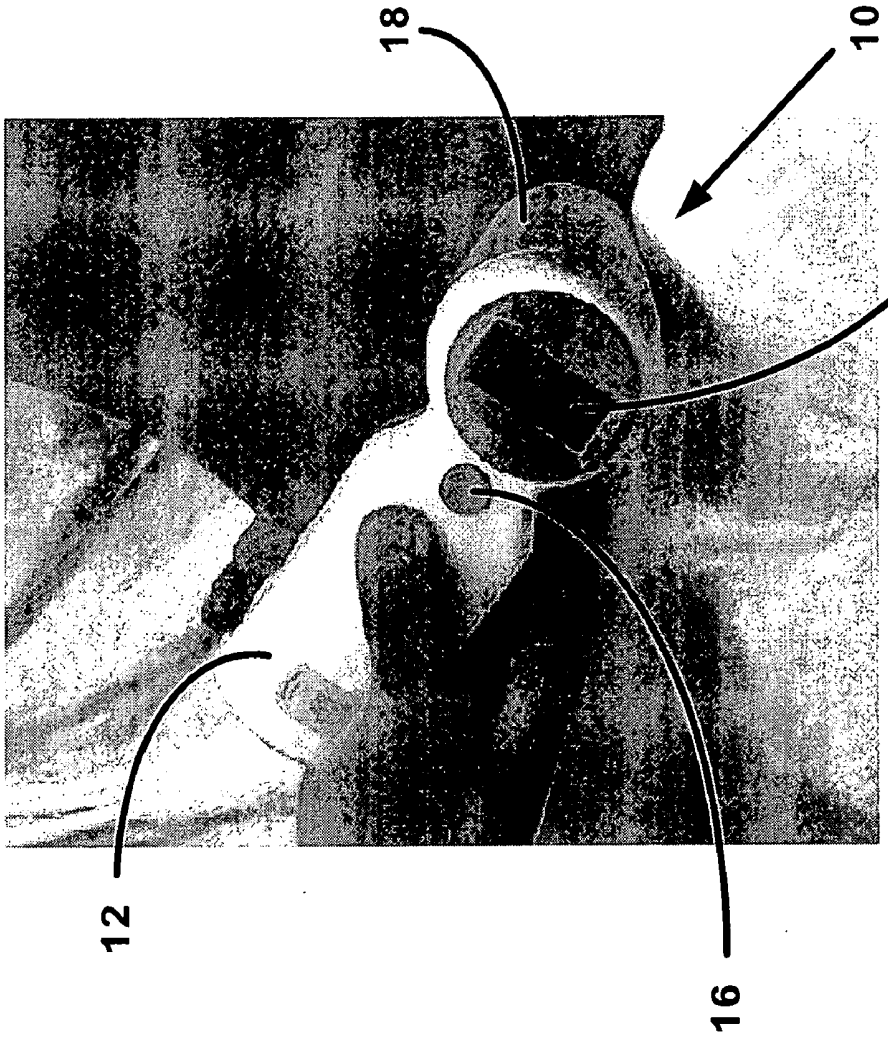


FIG. 2A

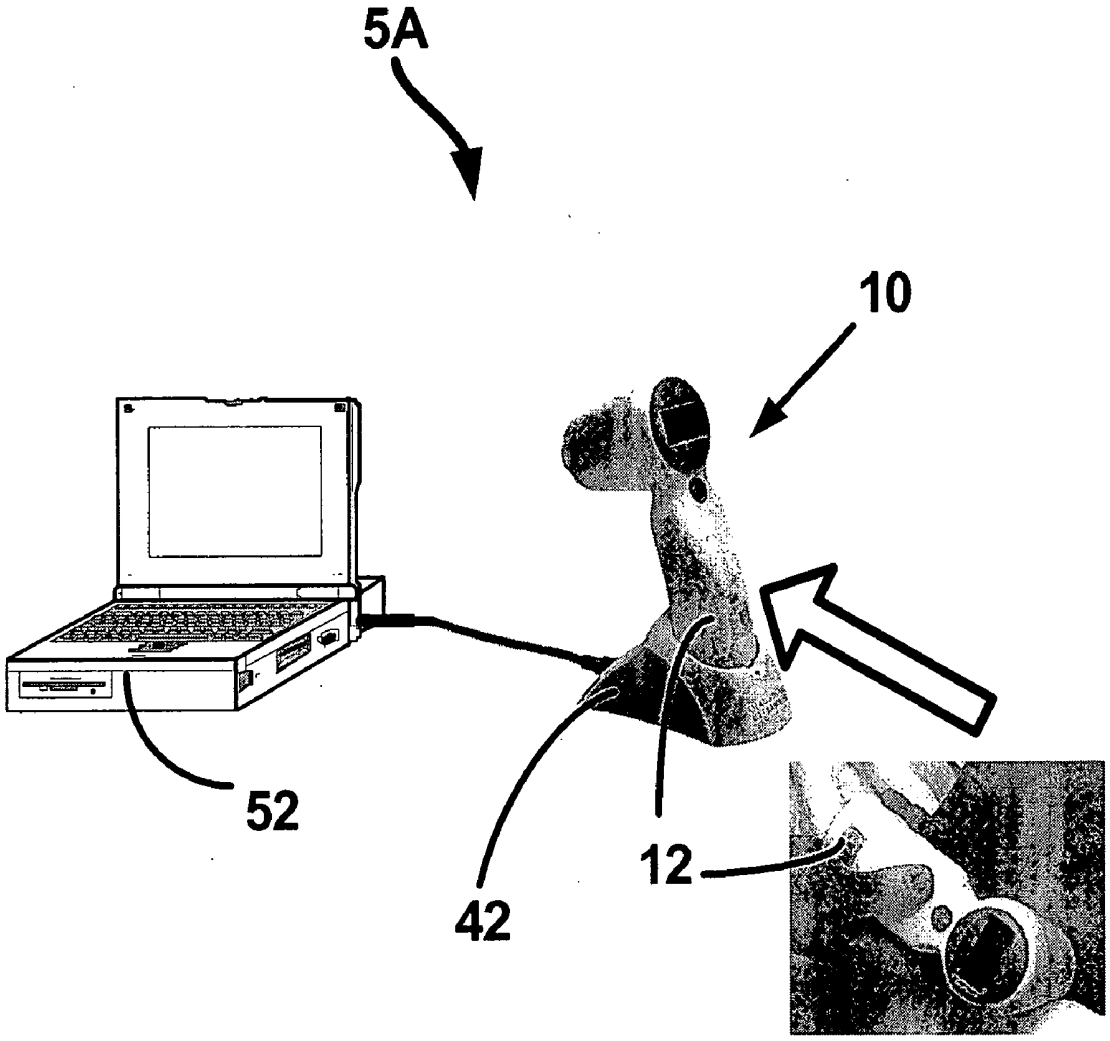


FIG. 2C

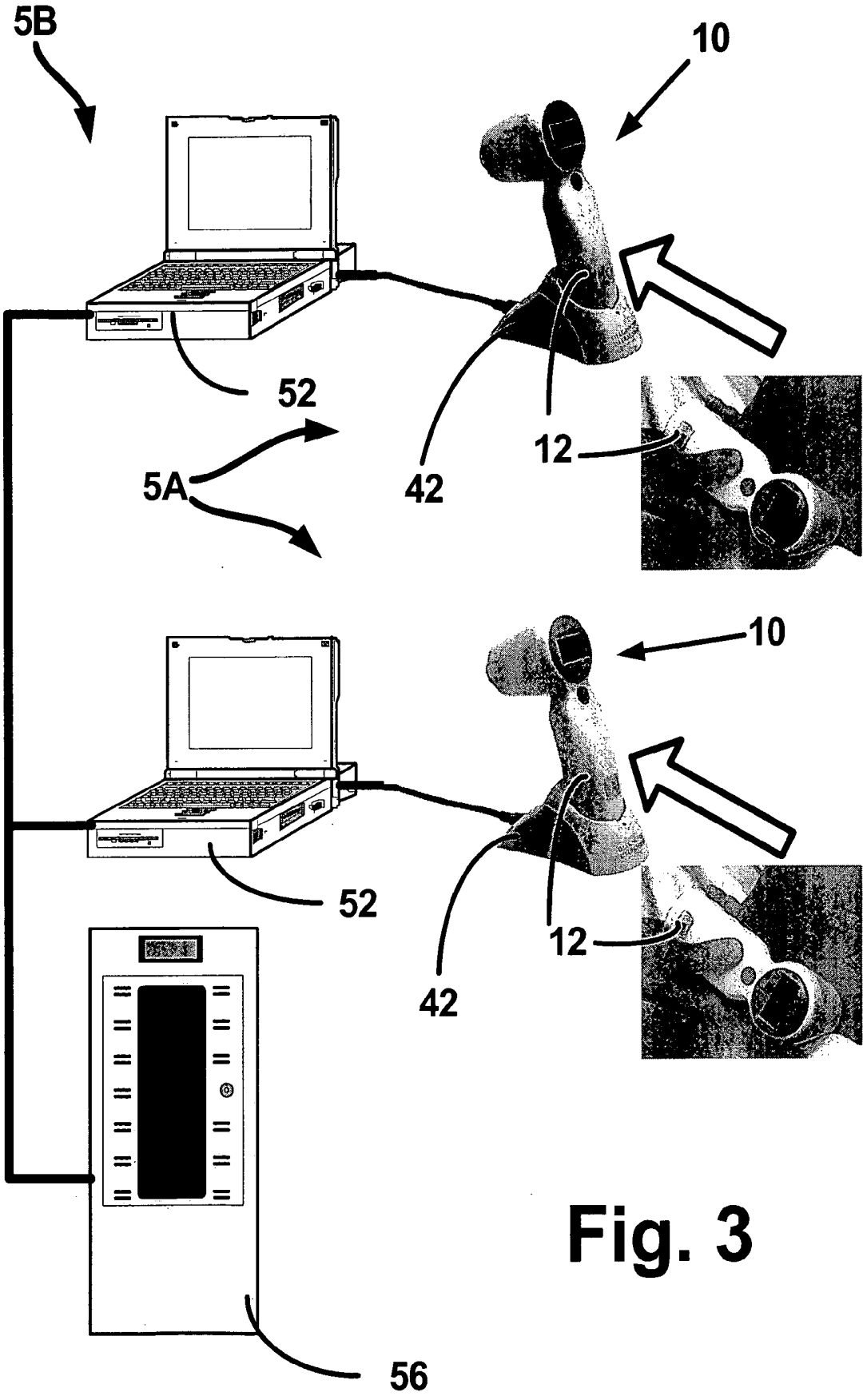


Fig. 3

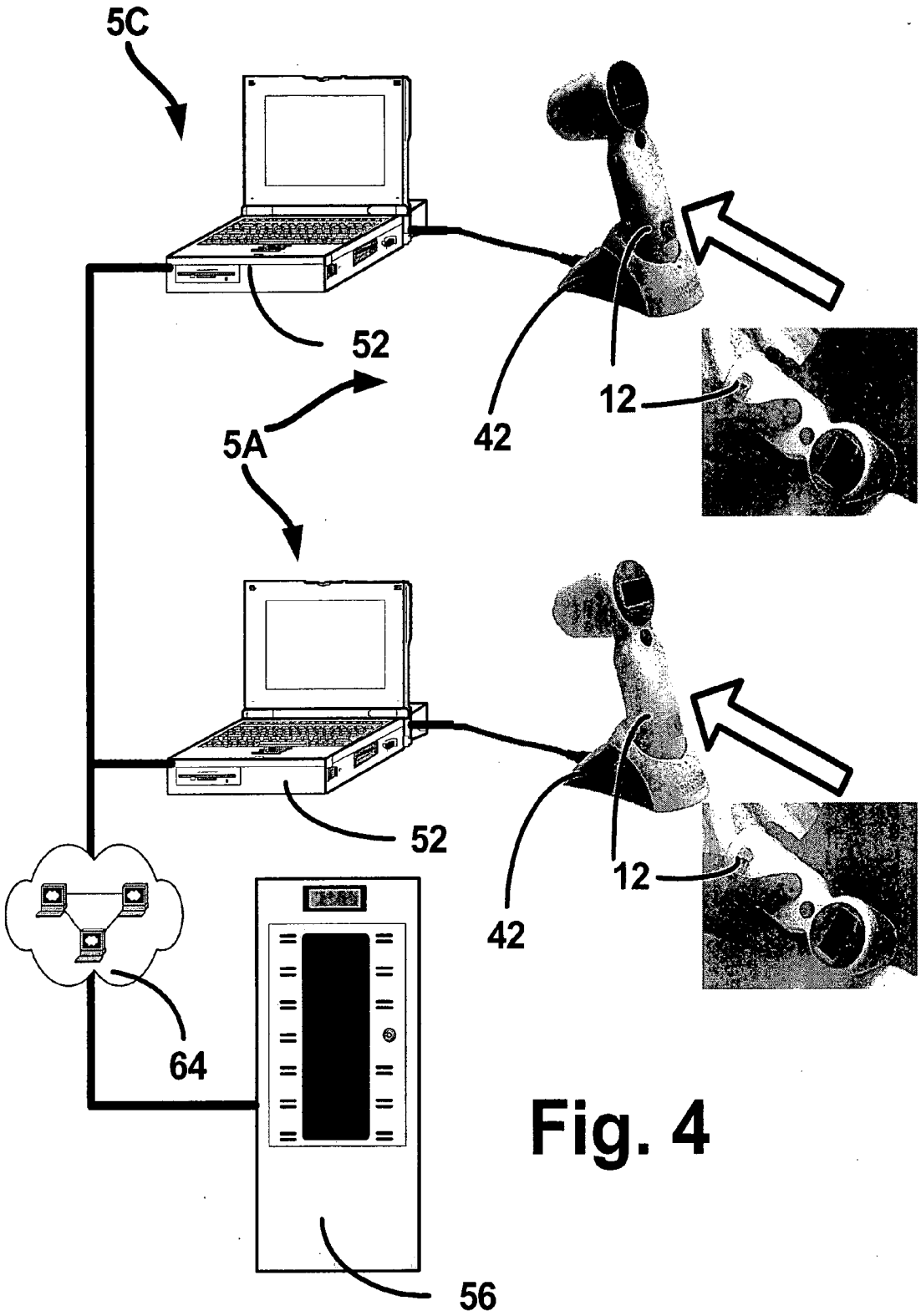


Fig. 4

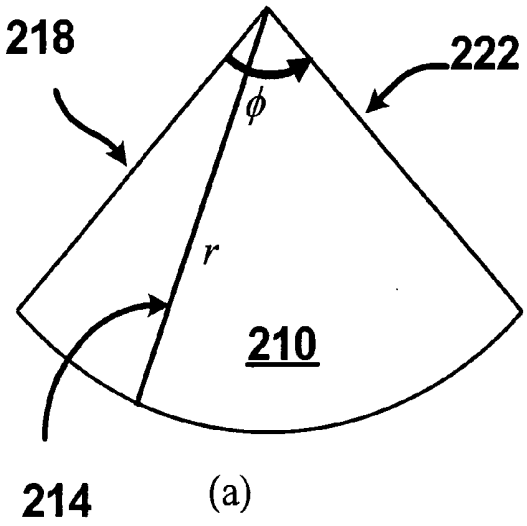


FIG. 5A

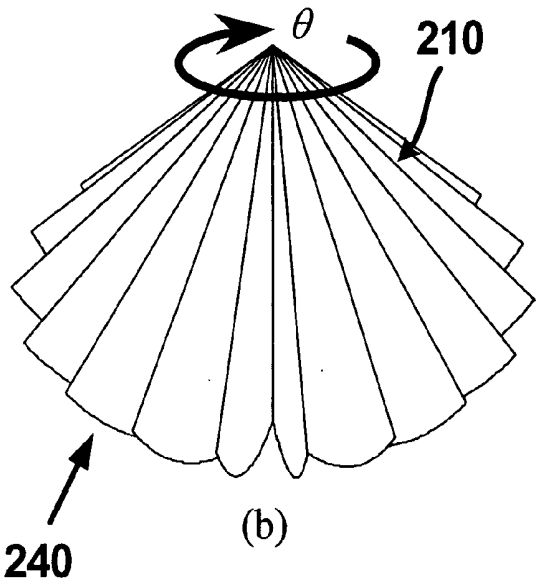


FIG. 5B

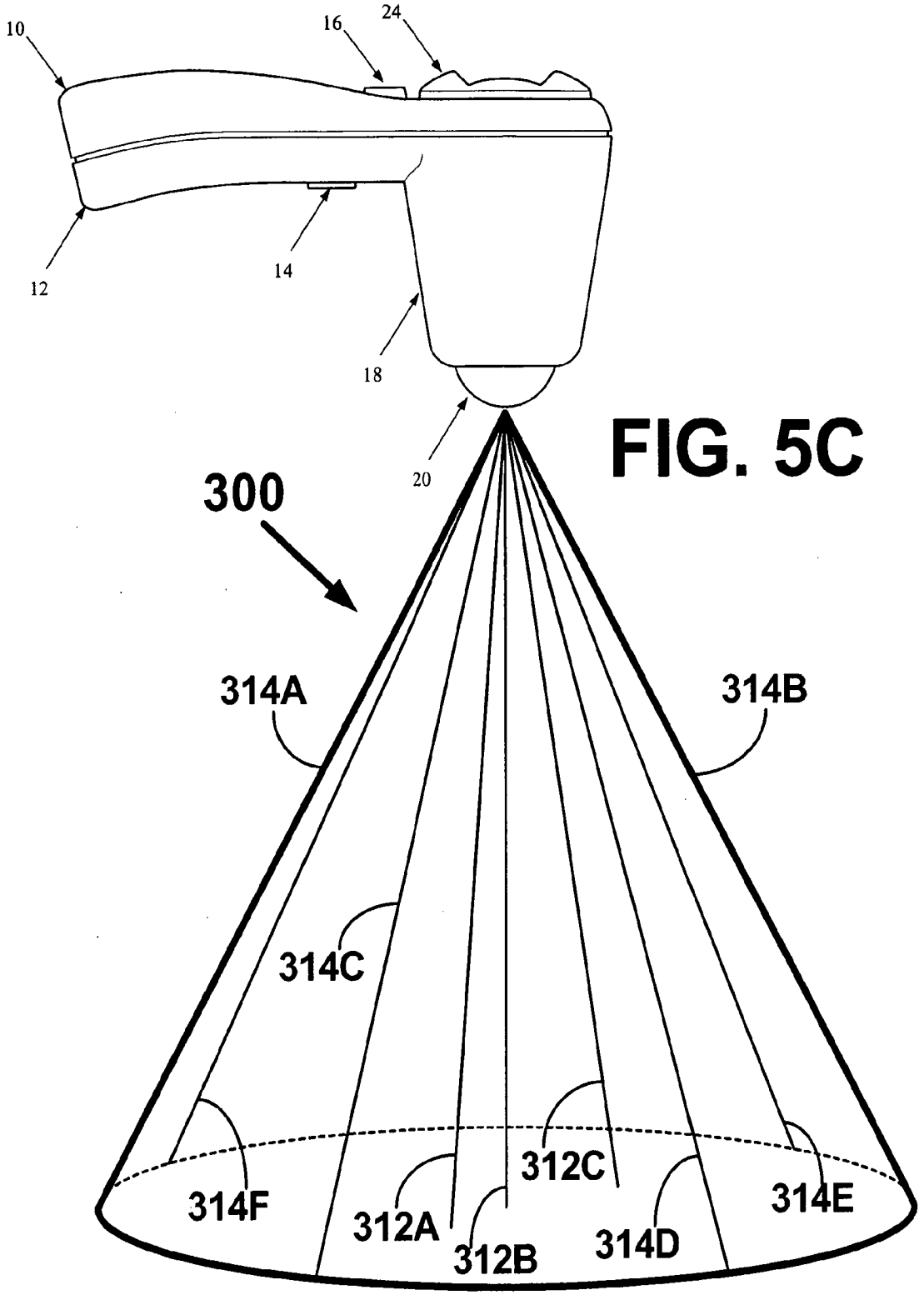
10
16
24
12
14
18
20
300
314A
314B
314C
314F
312A
312B
312C
314D
314E

FIG. 5C

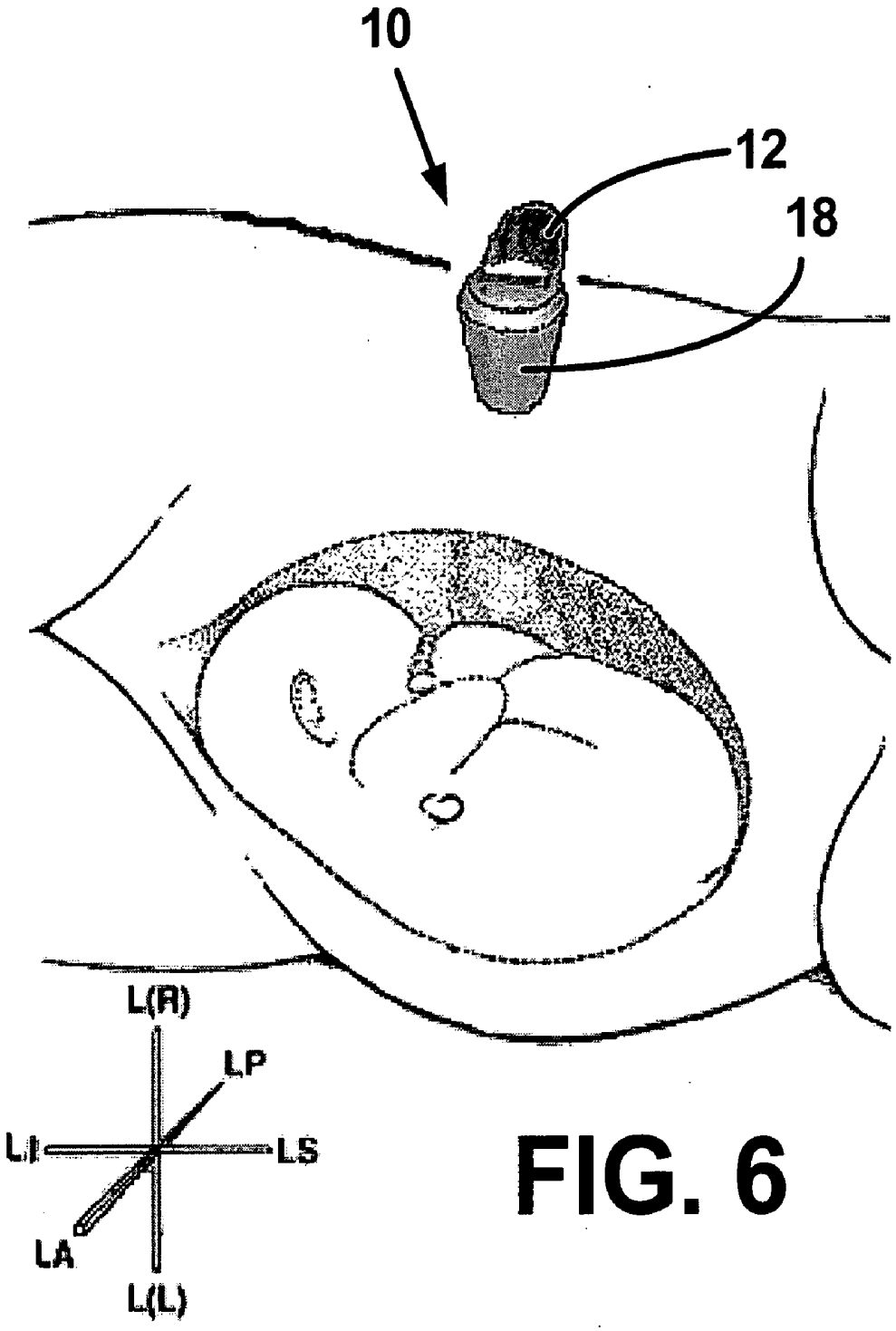


FIG. 6

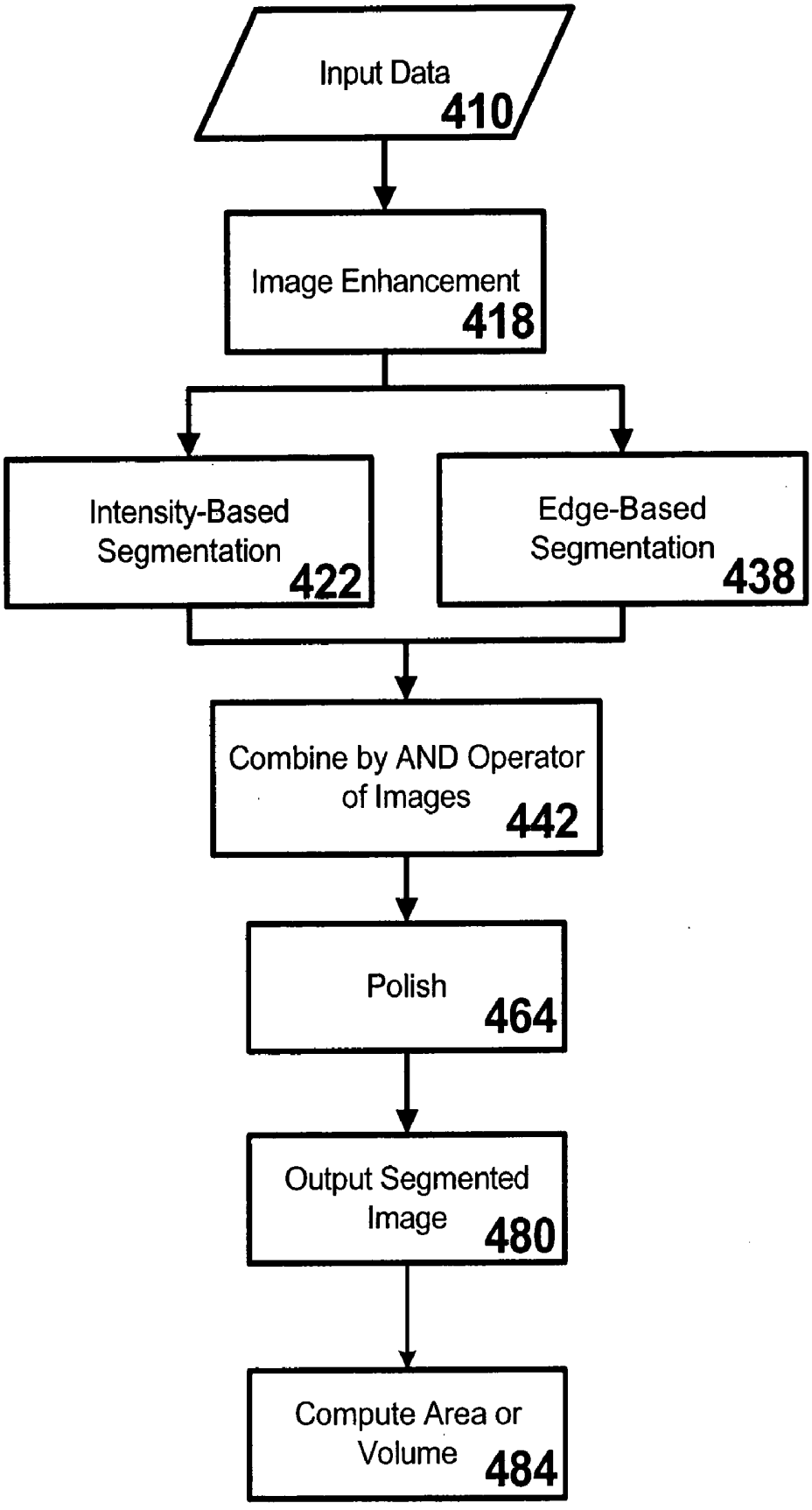
Input Data
410
Image Enhancement
418
Intensity-Based
Segmentation
422
Edge-Based
Segmentation
438
Combine by AND Operator
of Images
442
Polish
464
Output Segmented
Image
480
Compute Area or
Volume
484

FIG. 7

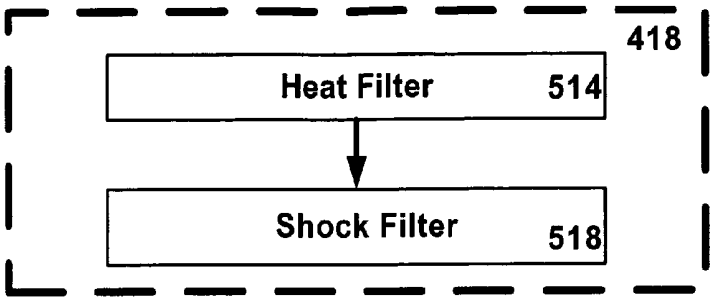


FIG. 8A

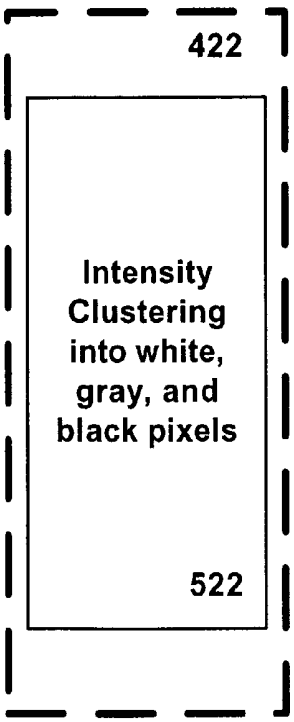


FIG. 8B

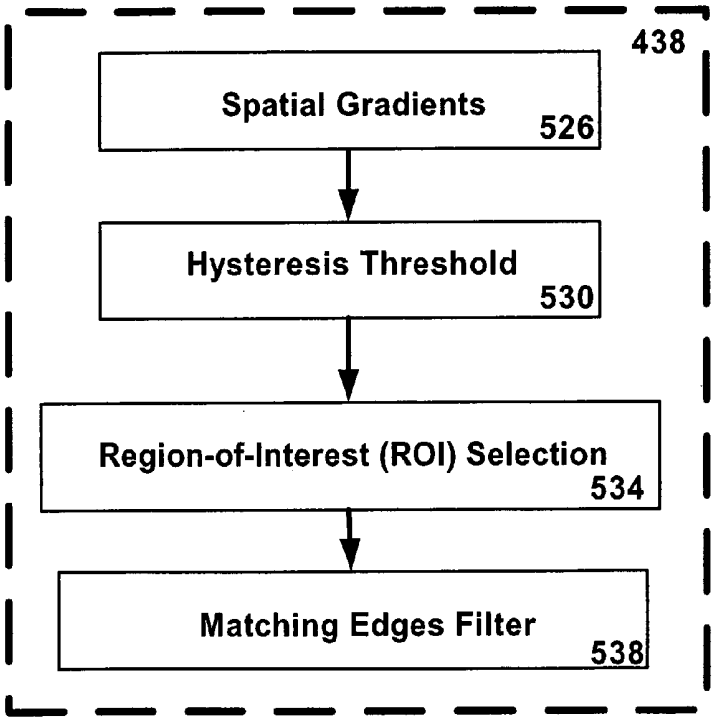


FIG. 8C

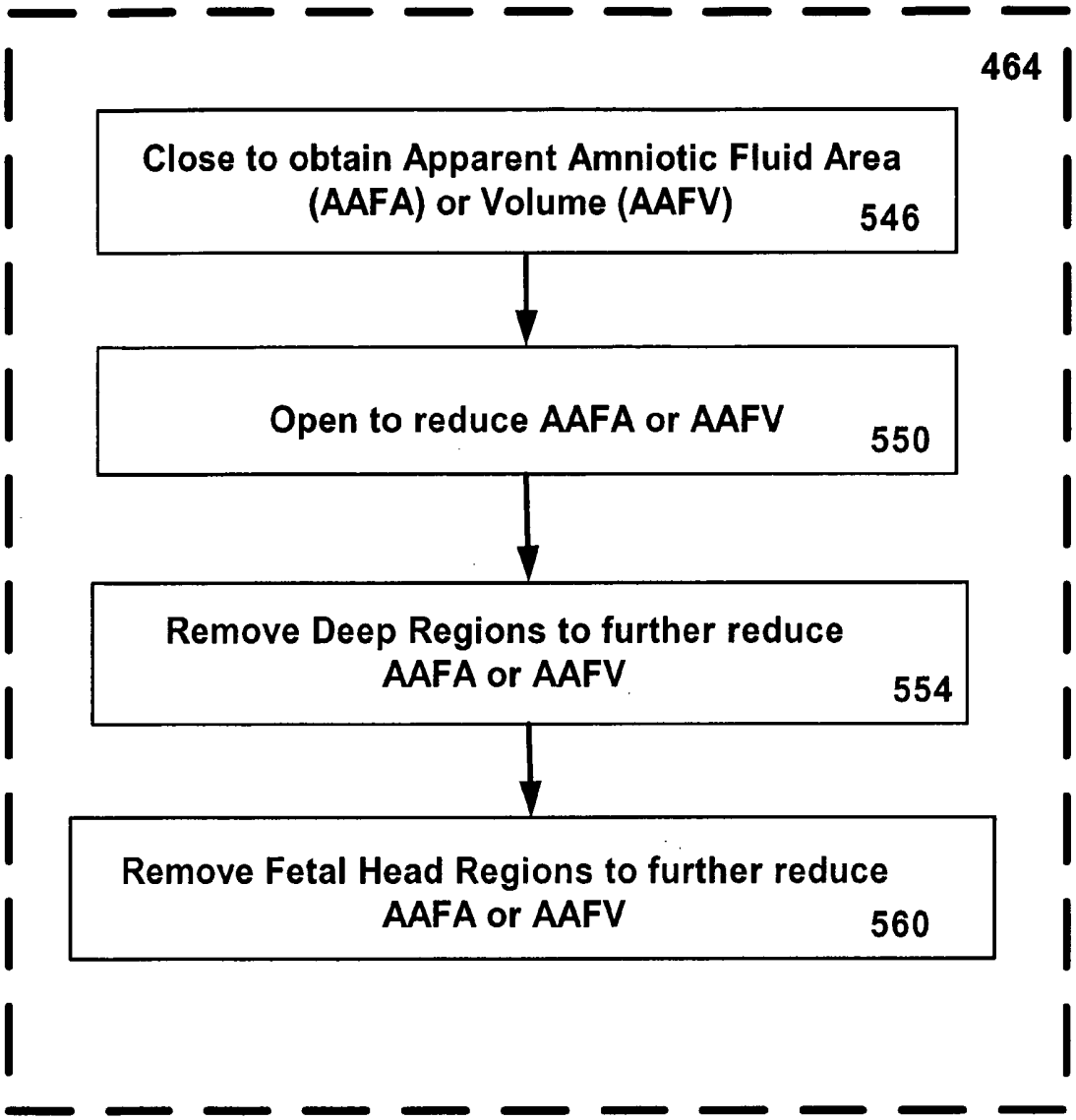
464
Close to obtain Apparent Amniotic Fluid Area (AAFA) or Volume (AAFV)
546
Open to reduce AAFA or AAFV
550
Remove Deep Regions to further reduce AAFA or AAFV
554
Remove Fetal Head Regions to further reduce AAFA or AAFV
560

FIG. 8D

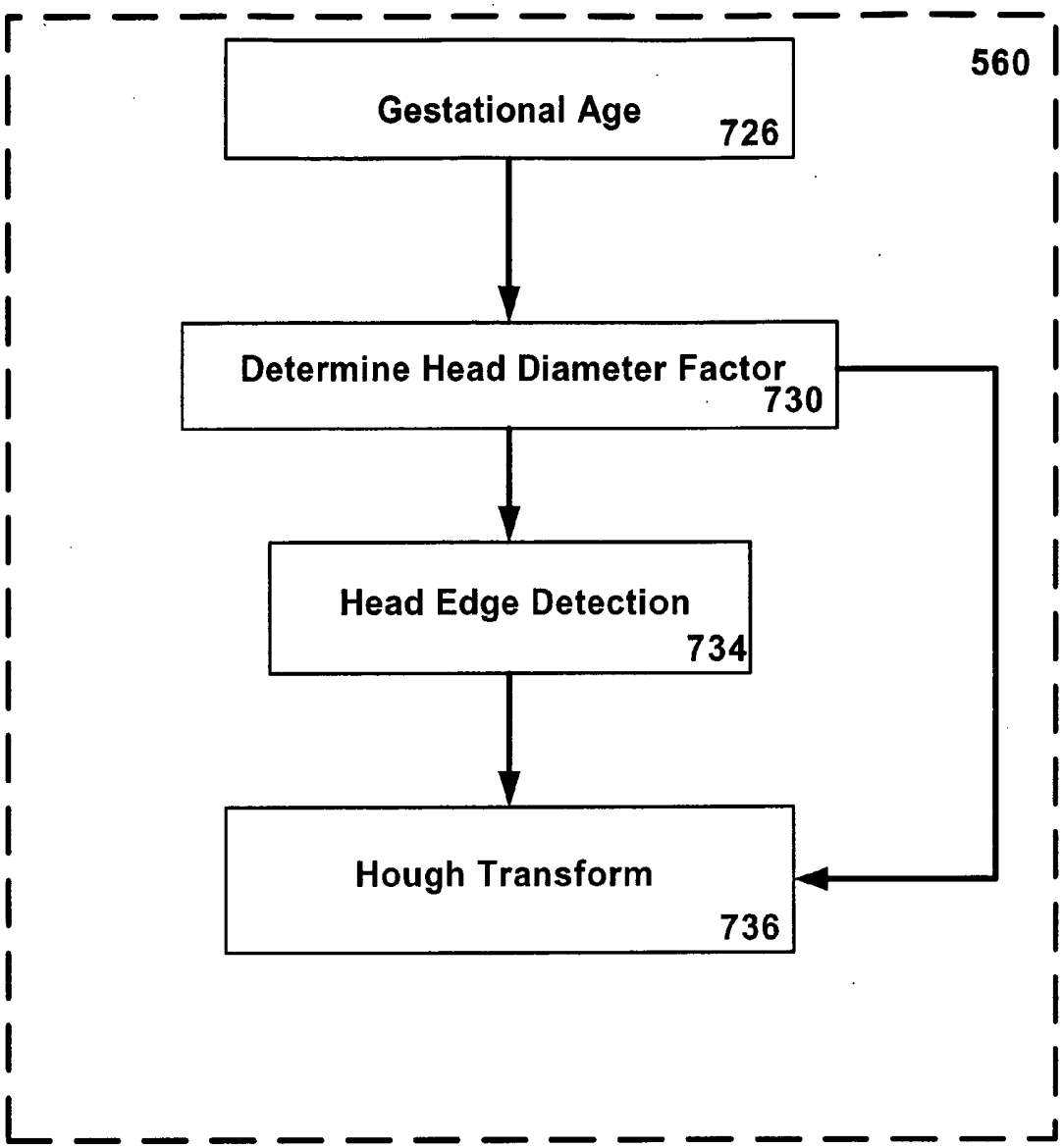
560
Gestational Age
726
Determine Head Diameter Factor
730
Head Edge Detection
734
Hough Transform
736

FIG. 8E

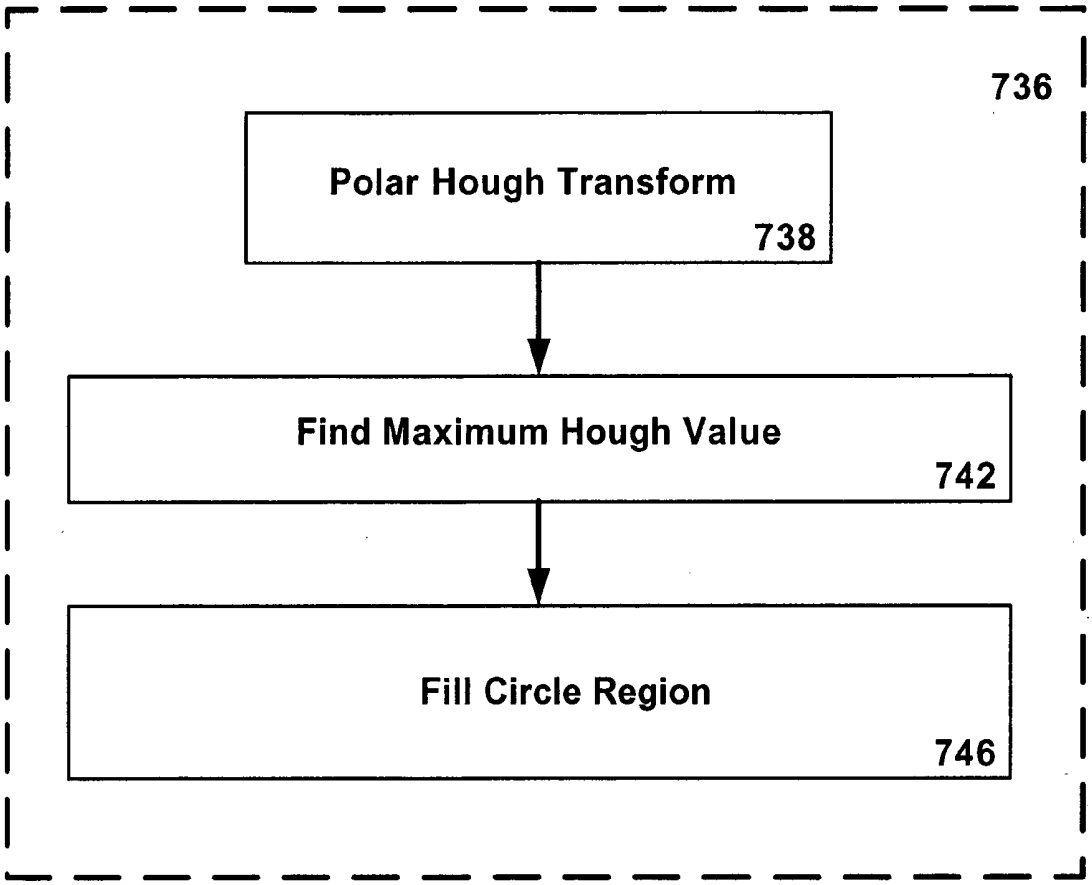
736
Polar Hough Transform
738
Find Maximum Hough Value
742
Fill Circle Region
746

FIG. 8F

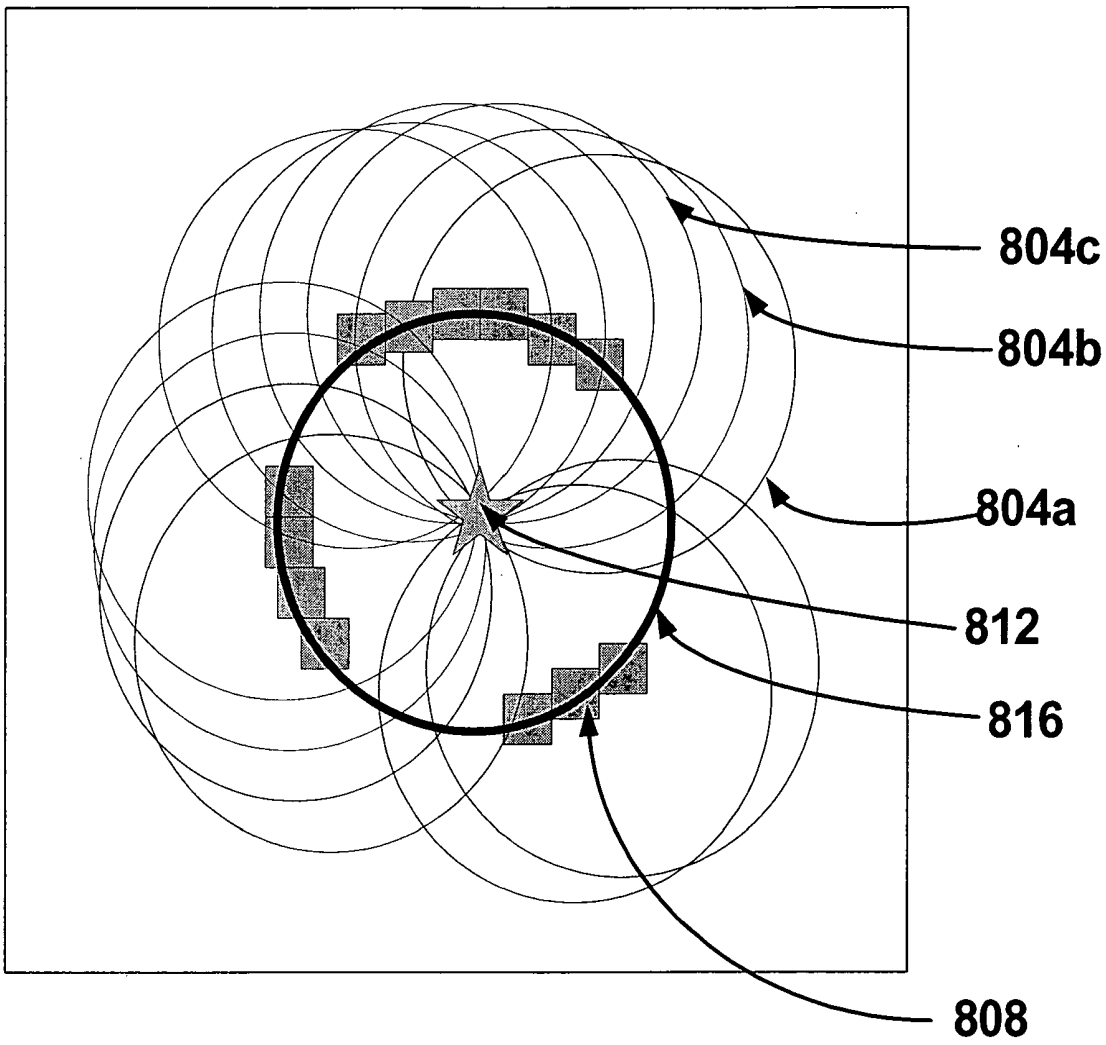


FIG. 9

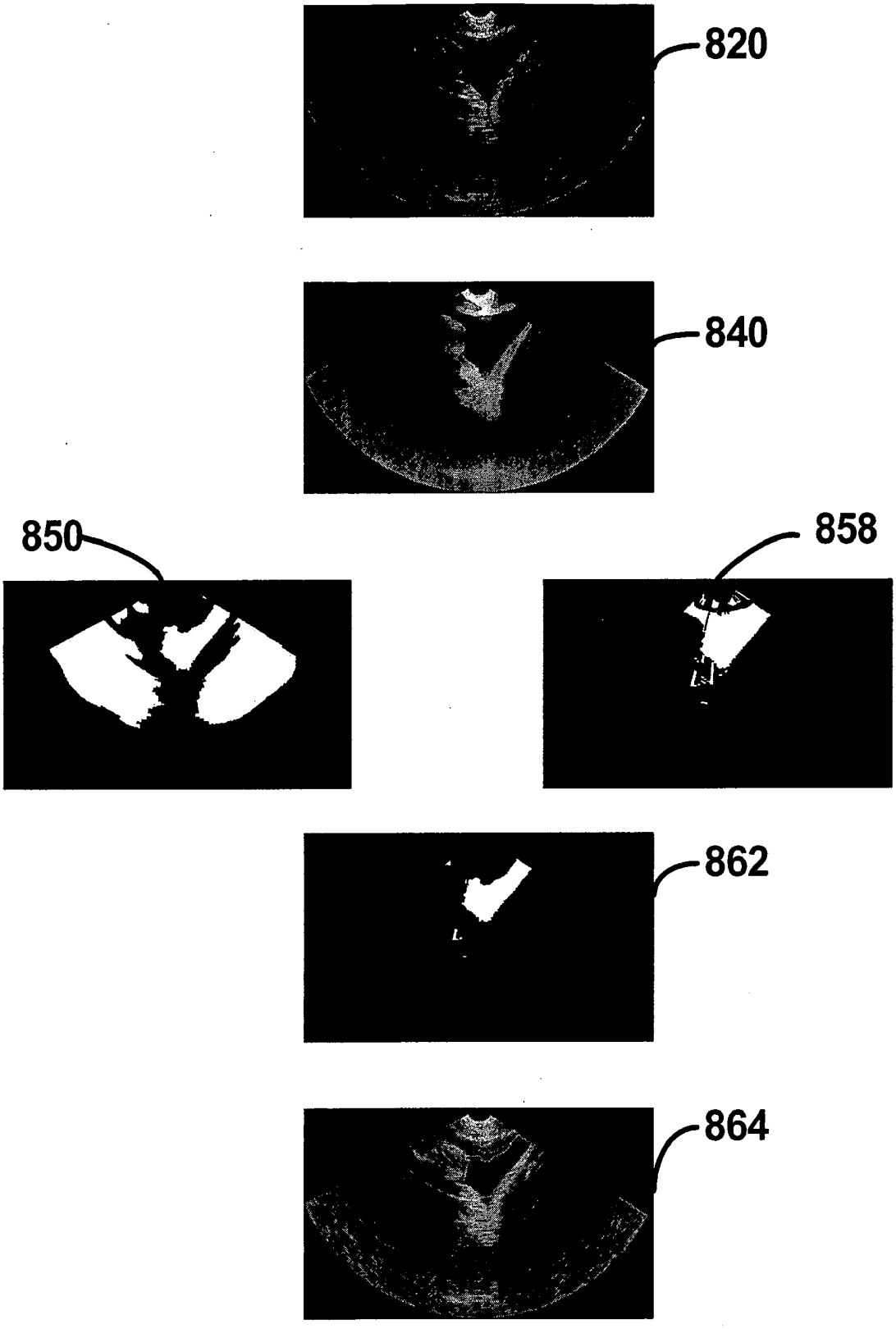


FIG. 10

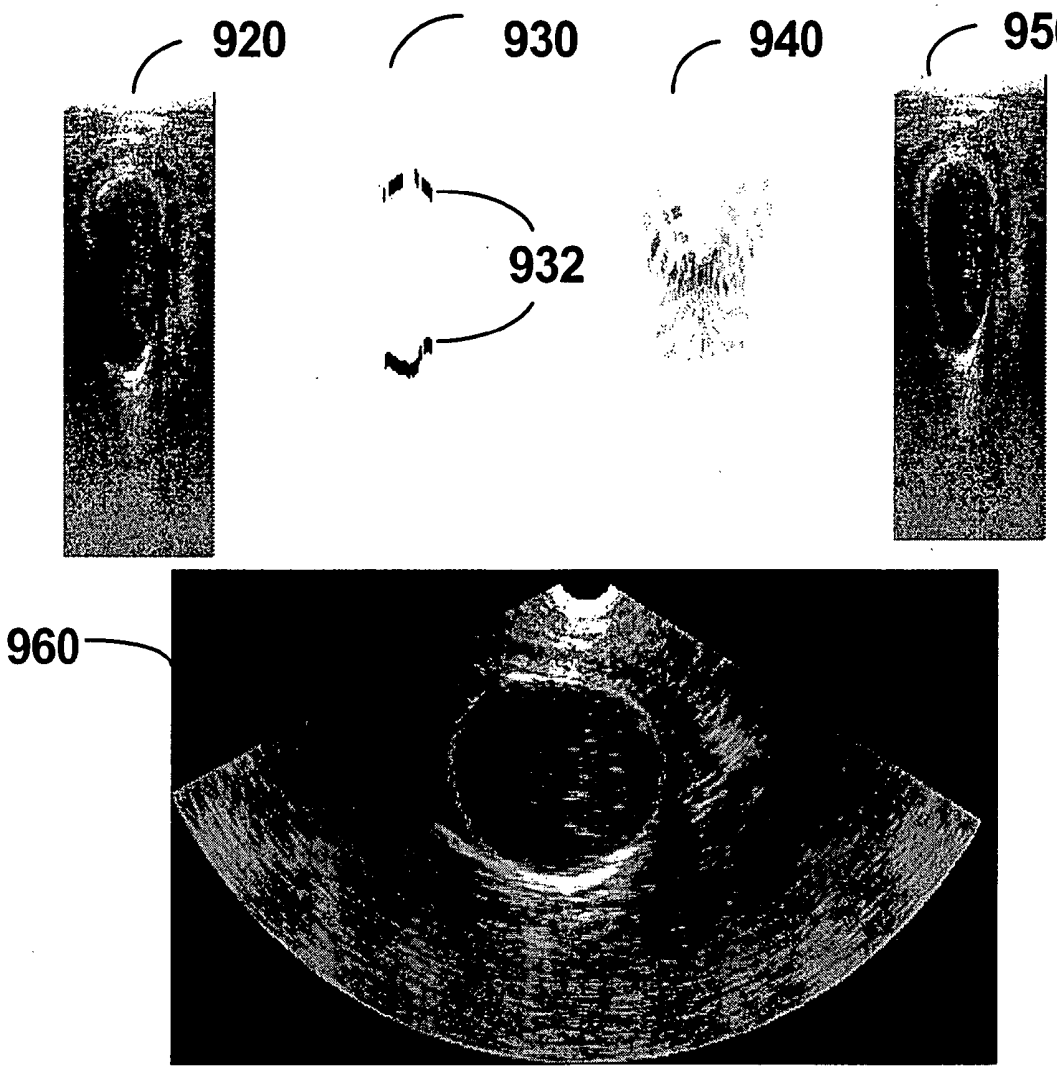


FIG. 11

FIG. 12

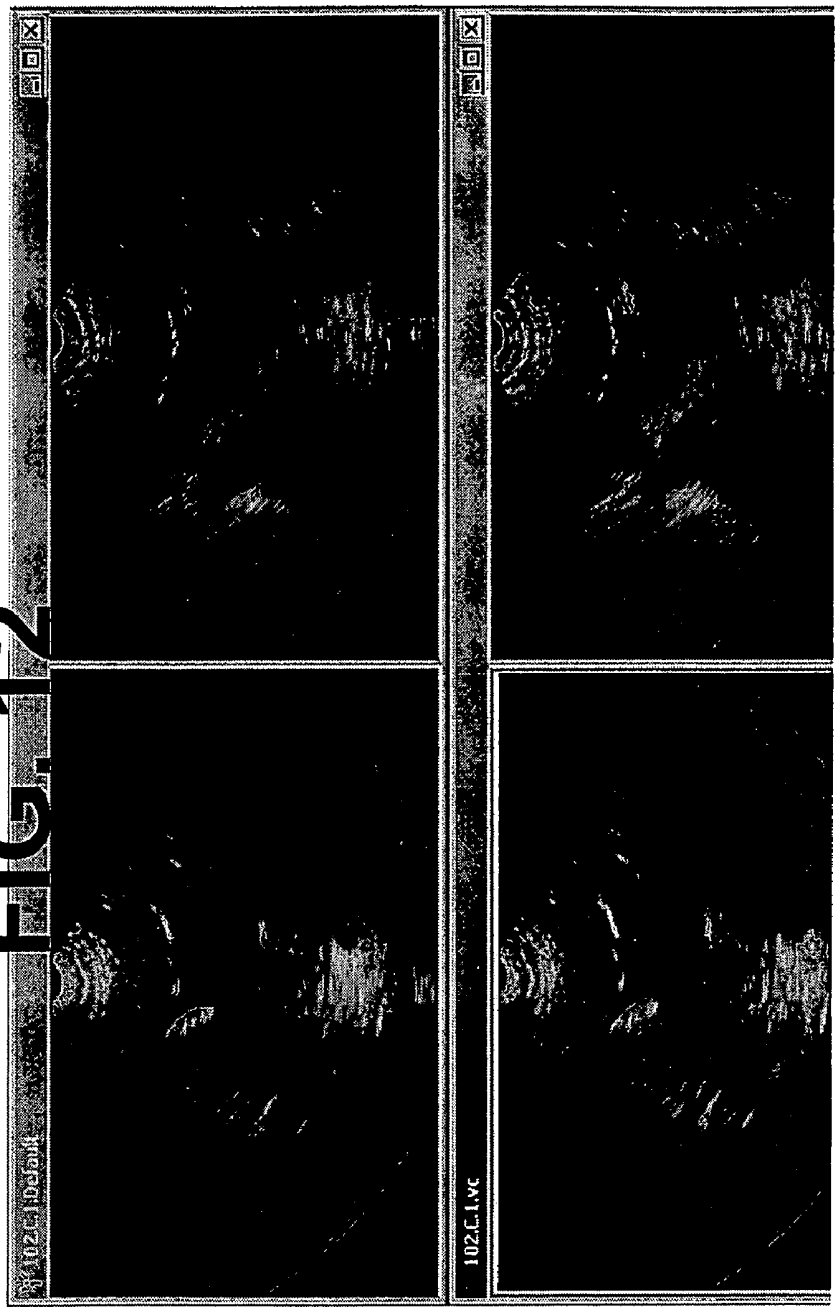

# Fig. 13

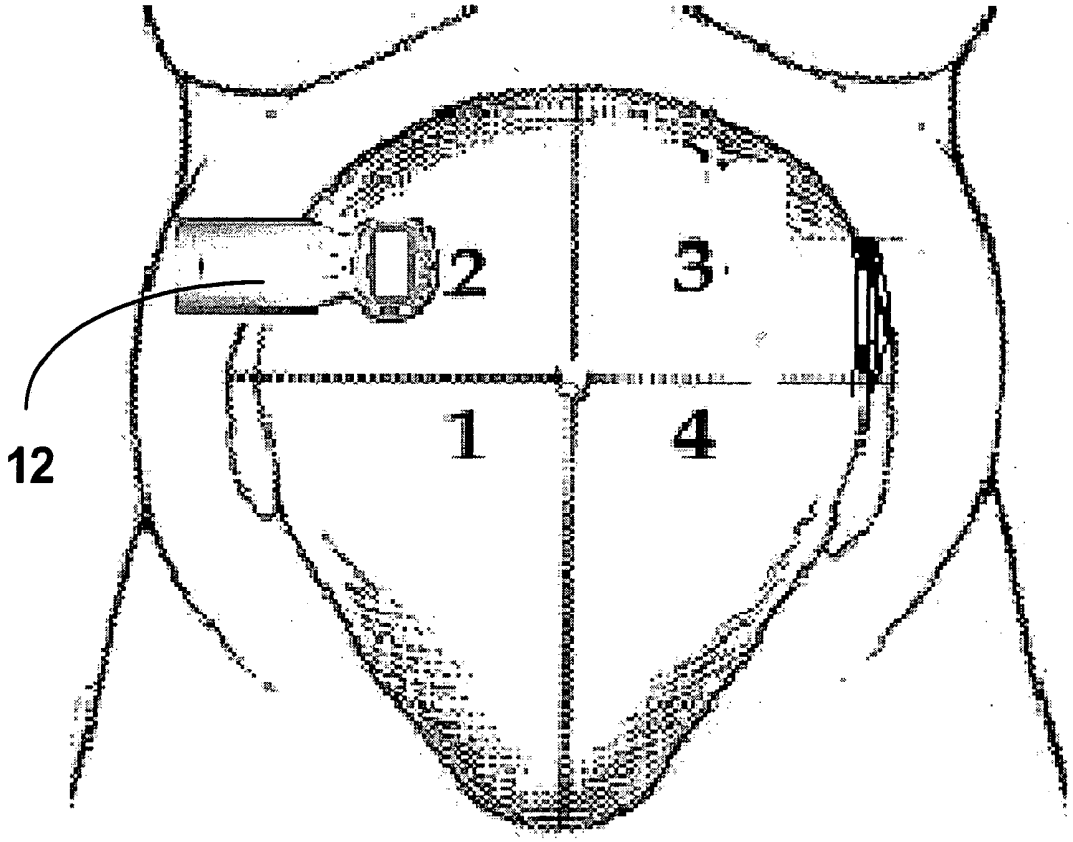

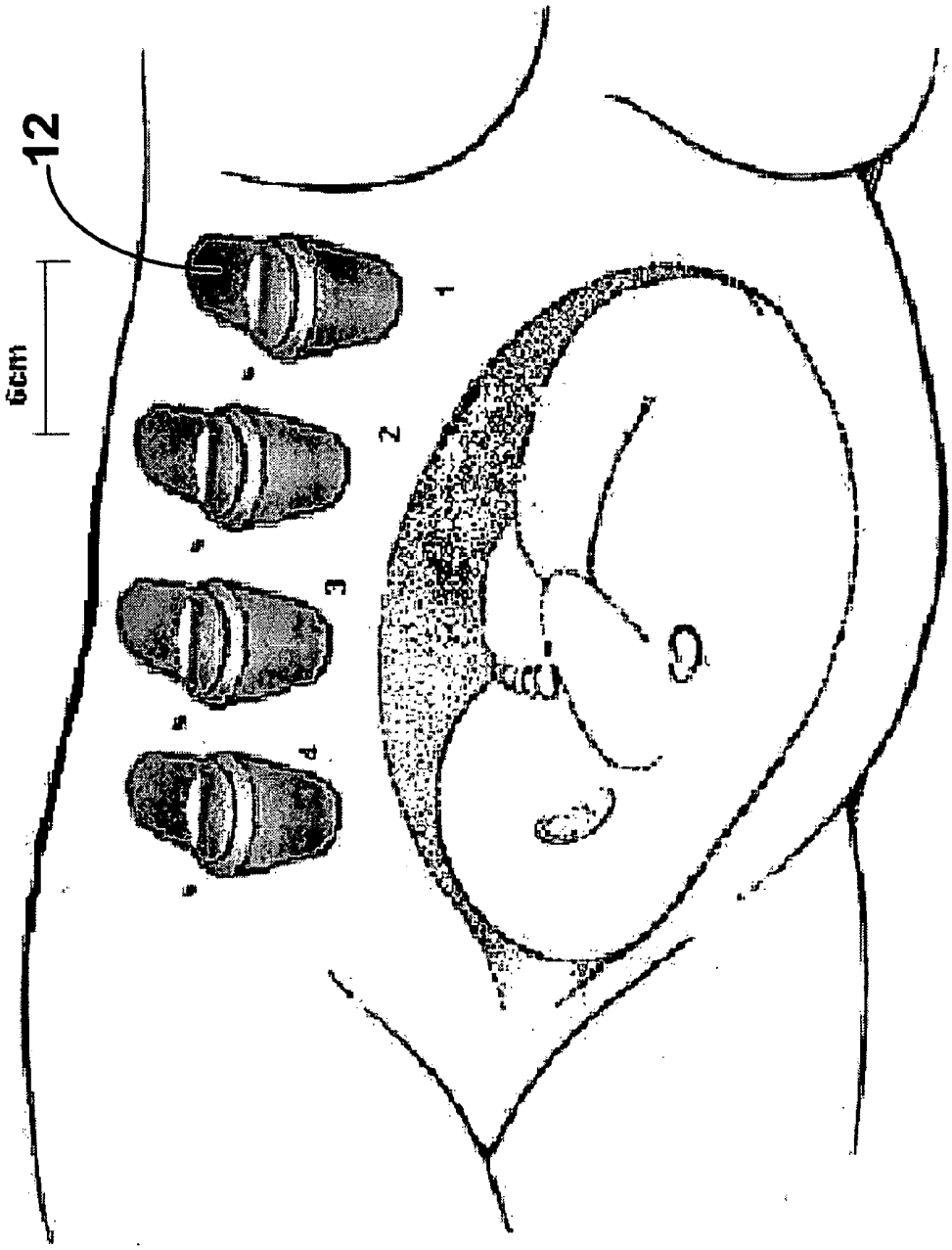


Fig. 14

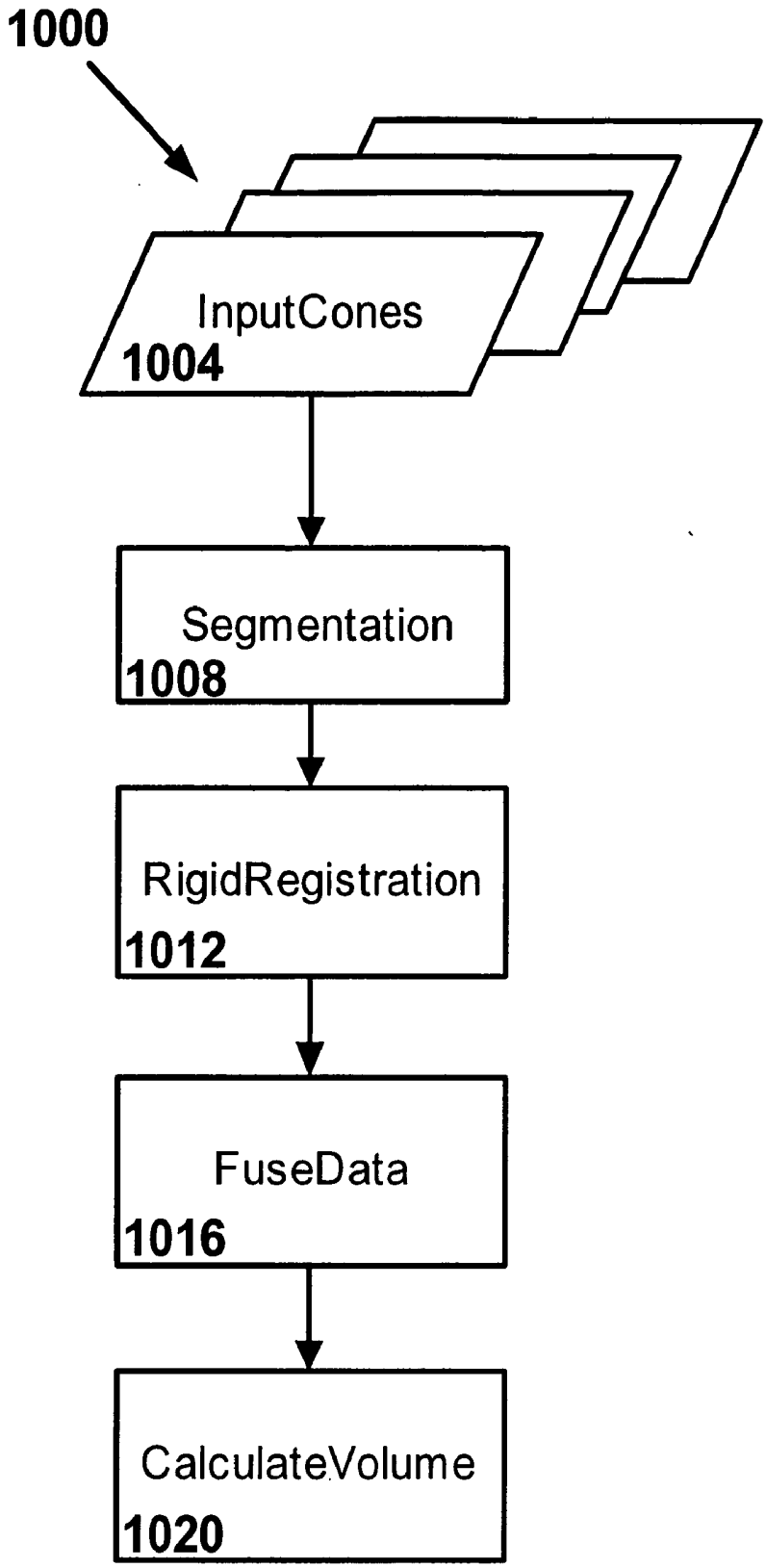
1000
InputCones
1004
Segmentation
1008
RigidRegistration
1012
FuseData
1016
CalculateVolume
1020

Fig. 15

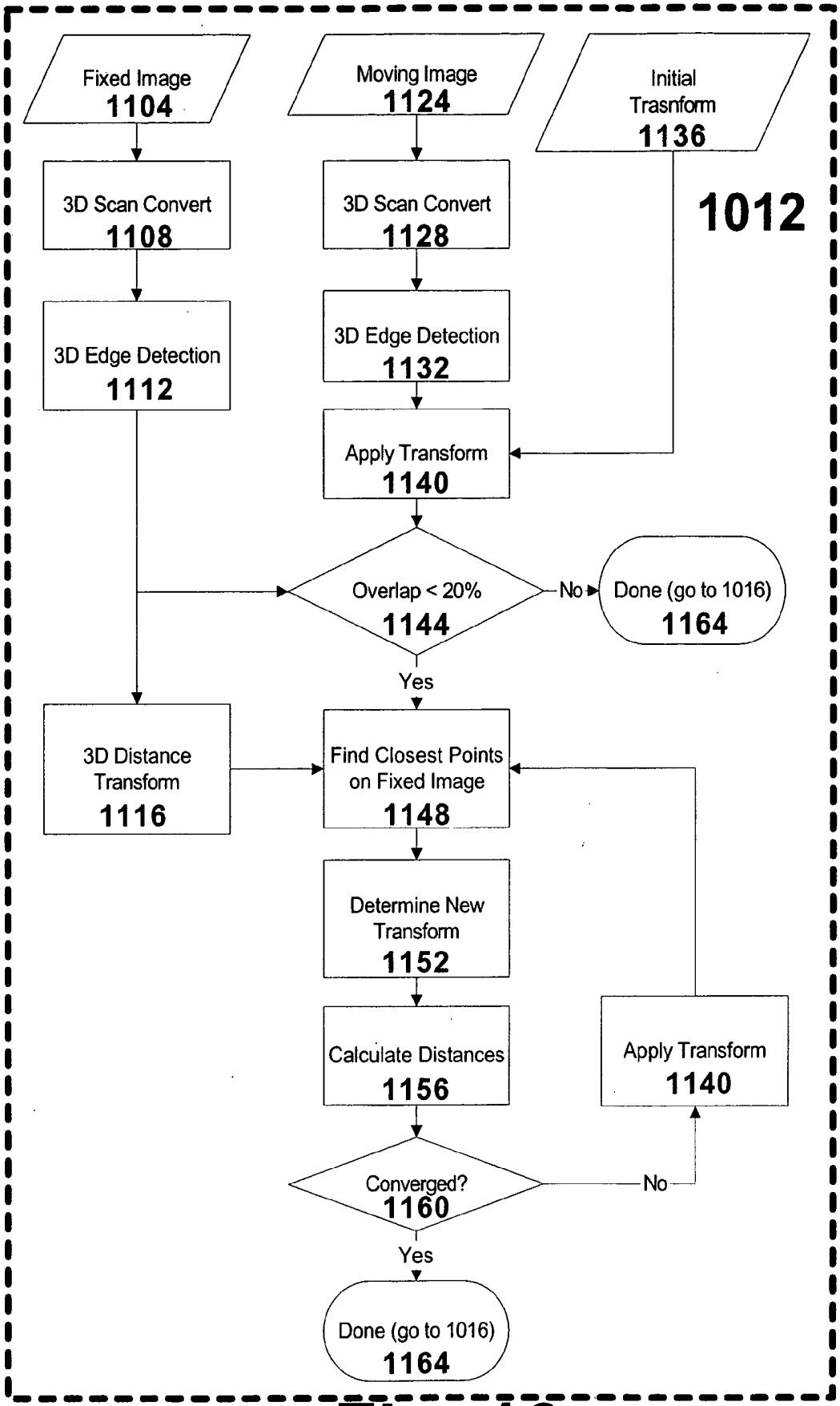
Fixed Image
1104
Moving Image
1124
Initial
Trasnform
1136
1012
3D Scan Convert
1108
3D Scan Convert
1128
3D Edge Detection
1112
3D Edge Detection
1132
Apply Transform
1140
Overlap < 20%
1144
No
Done (go to 1016)
1164
Yes
3D Distance
Transform
1116
Find Closest Points
on Fixed Image
1148
Determine New
Transform
1152
Calculate Distances
1156
Apply Transform
1140
Converged?
1160
No
Yes
Done (go to 1016)
1164

Fig. 16

Fig. 17A

Fig. 17B

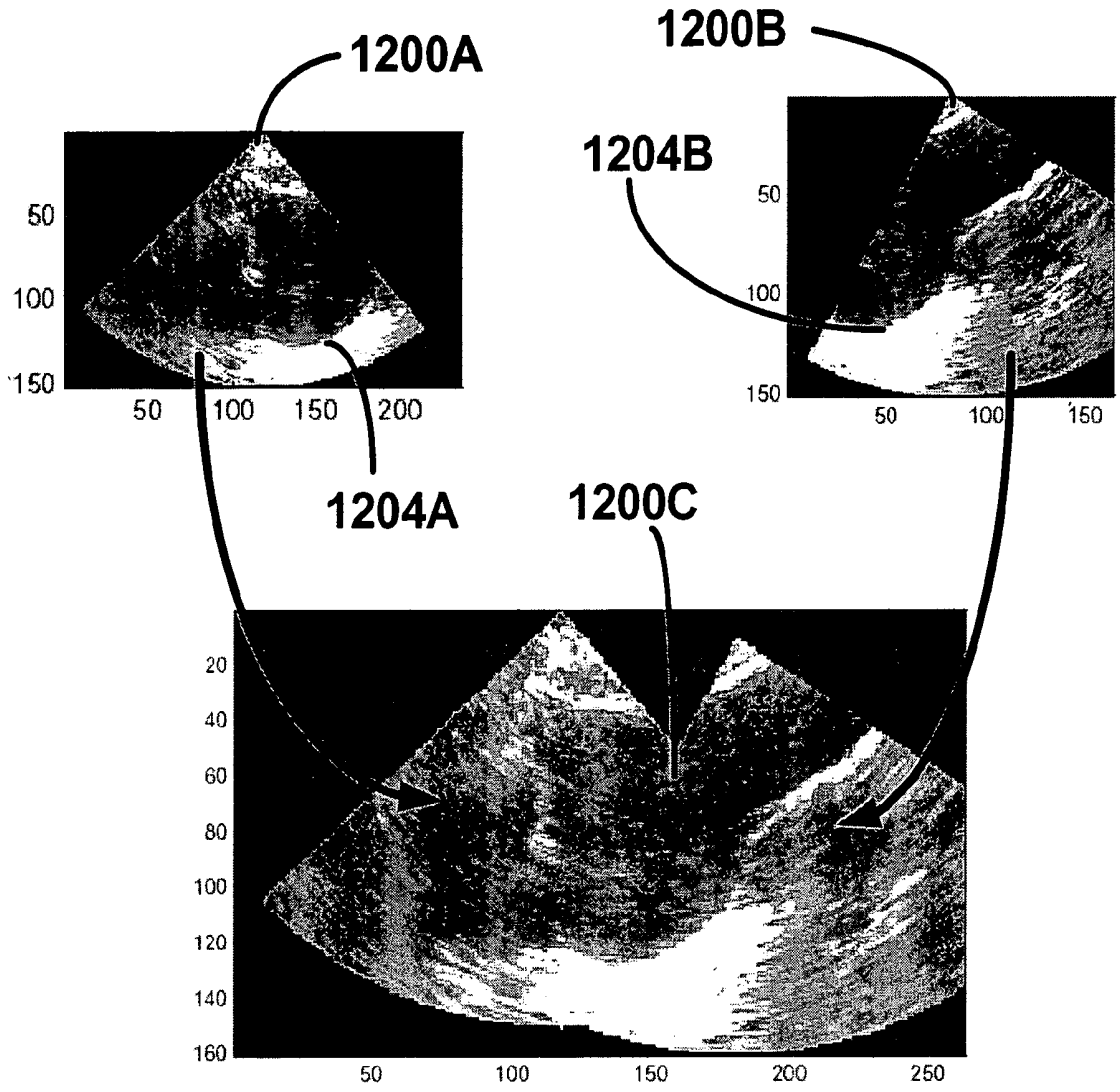


Fig. 17C

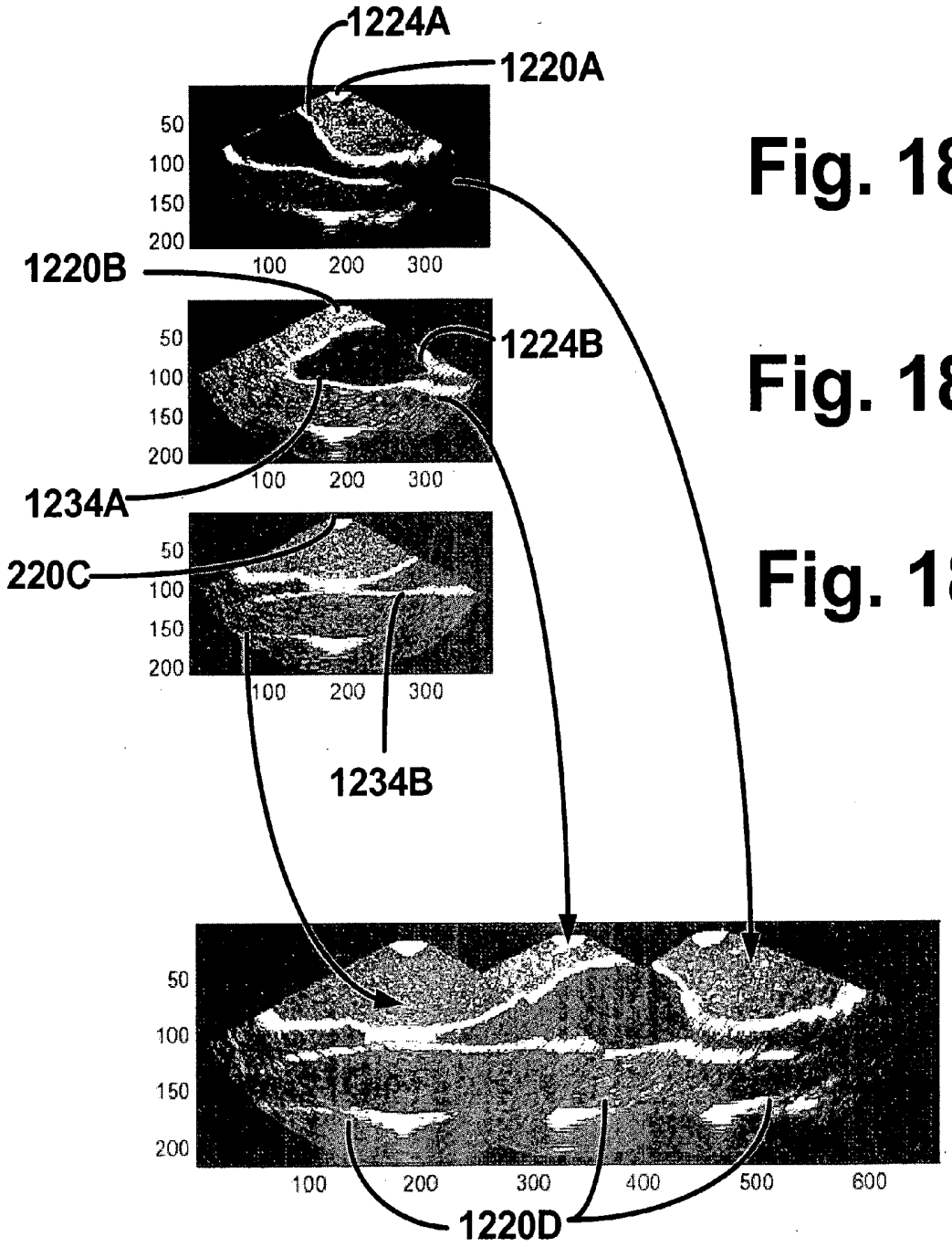


Fig. 18A

Fig. 18B

Fig. 18C

Fig. 18D

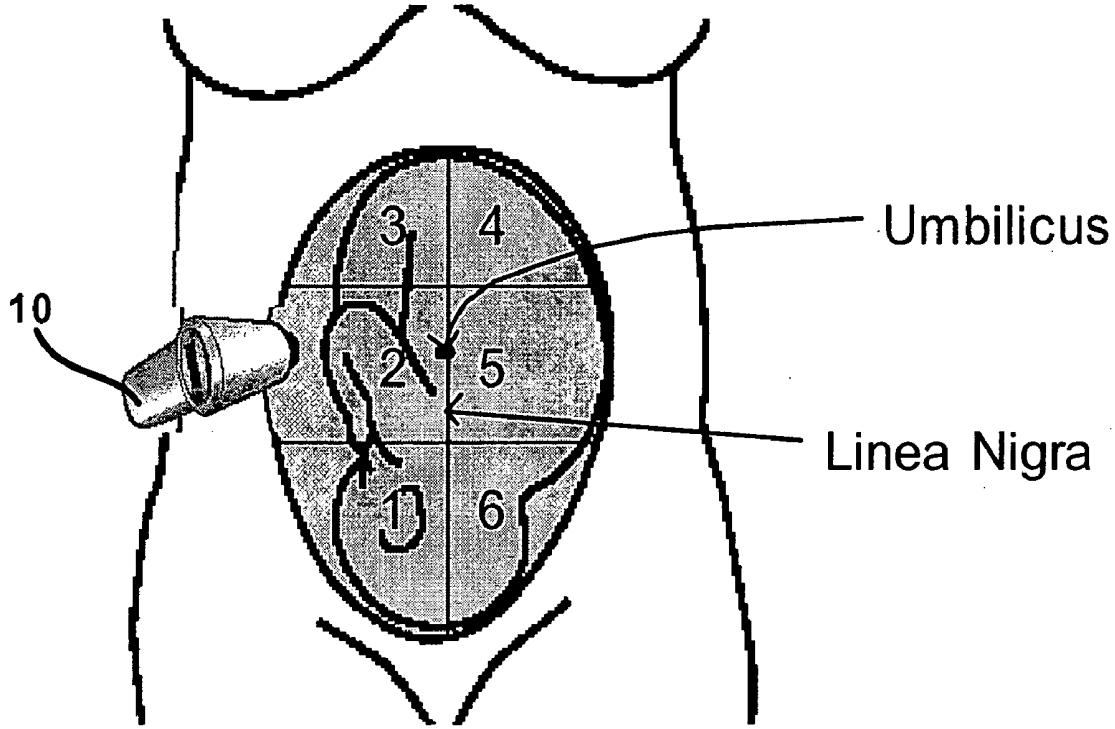


Fig. 19

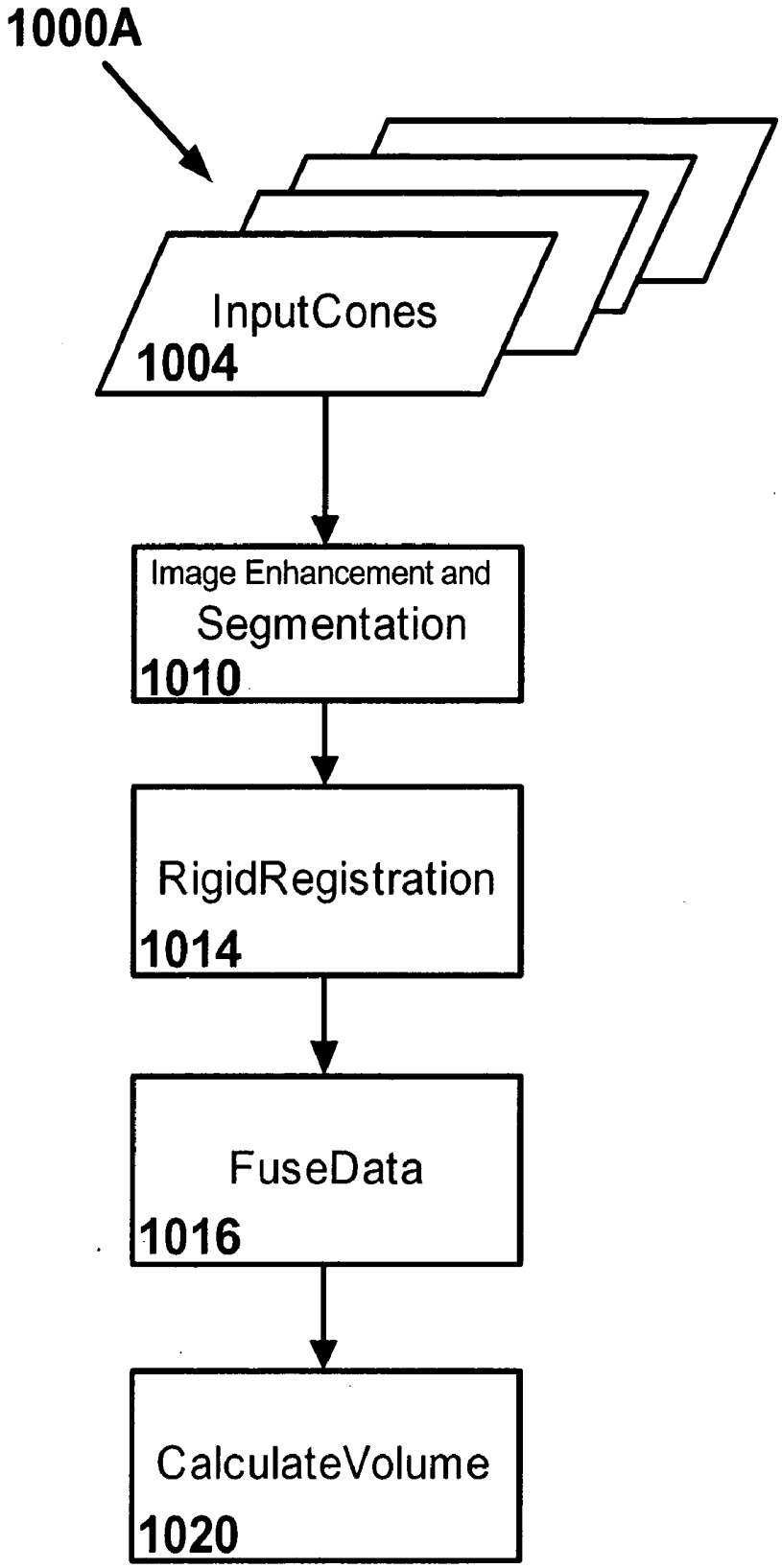
1000A
InputCones
1004
Image Enhancement and
Segmentation
1010
RigidRegistration
1014
FuseData
1016
CalculateVolume
1020

Fig. 20

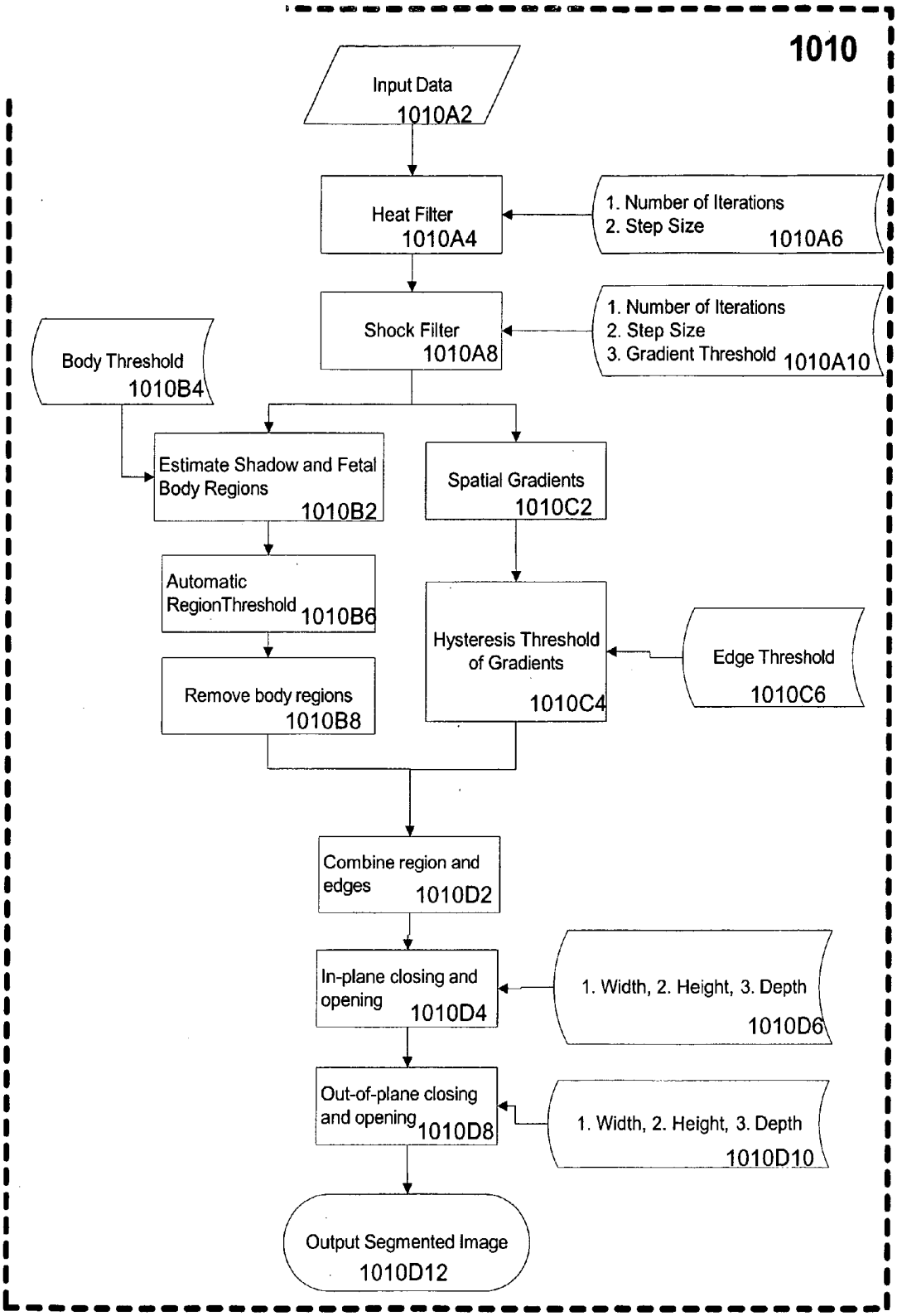
1010
Input Data
1010A2
Heat Filter
1010A4
1. Number of Iterations
2. Step Size
1010A6
Shock Filter
1010A8
1. Number of Iterations
2. Step Size
3. Gradient Threshold
1010A10
Body Threshold
1010B4
Estimate Shadow and Fetal Body Regions
1010B2
Spatial Gradients
1010C2
Automatic RegionThreshold
1010B6
Hysteresis Threshold of Gradients
1010C4
Edge Threshold
1010C6
Remove body regions
1010B8
Combine region and edges
1010D2
In-plane closing and opening
1010D4
1. Width, 2. Height, 3. Depth
1010D6
Out-of-plane closing and opening
1010D8
1. Width, 2. Height, 3. Depth
1010D10
Output Segmented Image
1010D12

Fig. 21

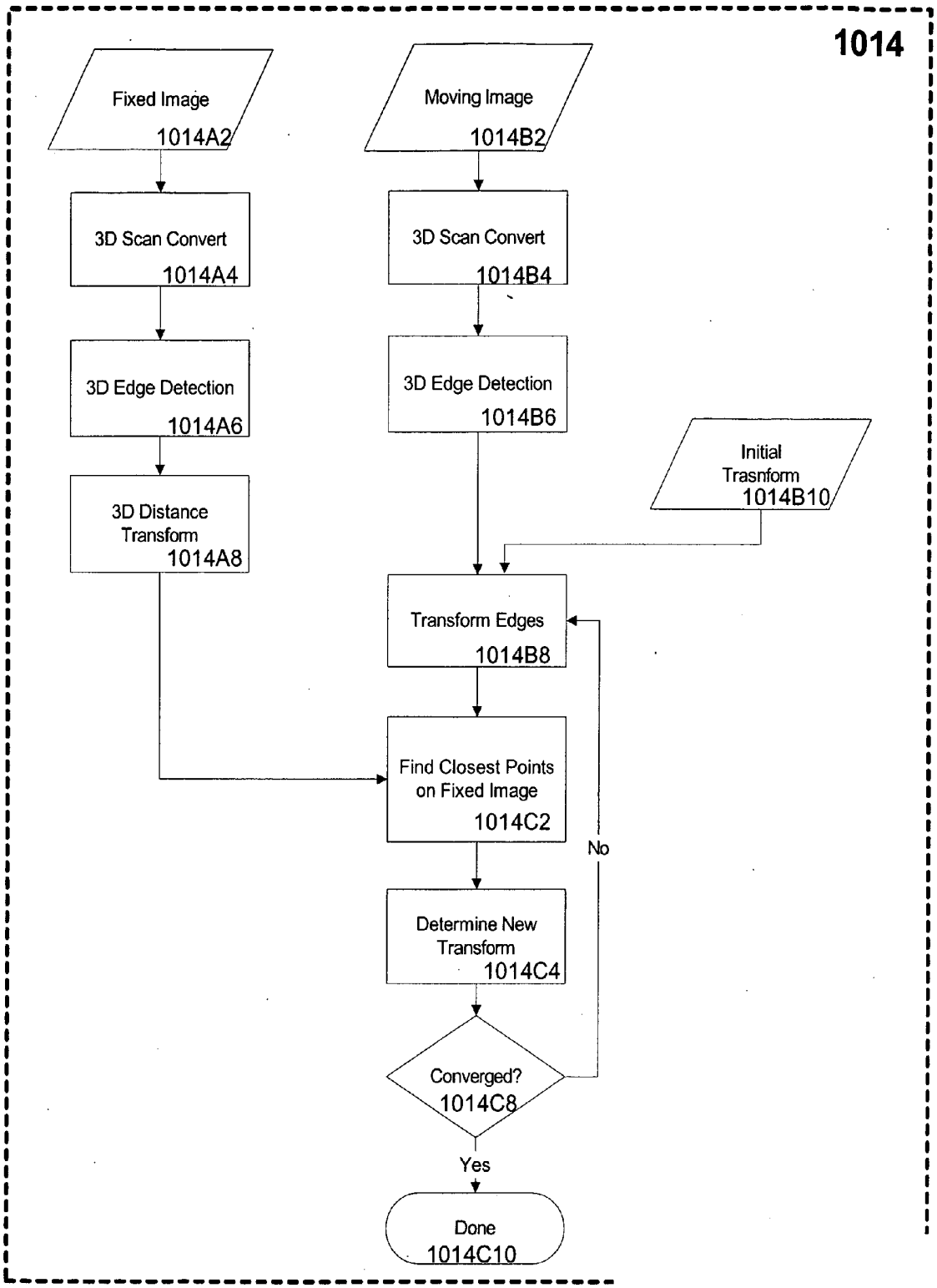
1014
Fixed Image
1014A2
Moving Image
1014B2
3D Scan Convert
1014A4
3D Scan Convert
1014B4
3D Edge Detection
1014A6
3D Edge Detection
1014B6
Initial
Trasnform
1014B10
3D Distance
Transform
1014A8
Transform Edges
1014B8
Find Closest Points
on Fixed Image
1014C2
No
Determine New
Transform
1014C4
Converged?
1014C8
Yes
Done
1014C10

Fig. 22

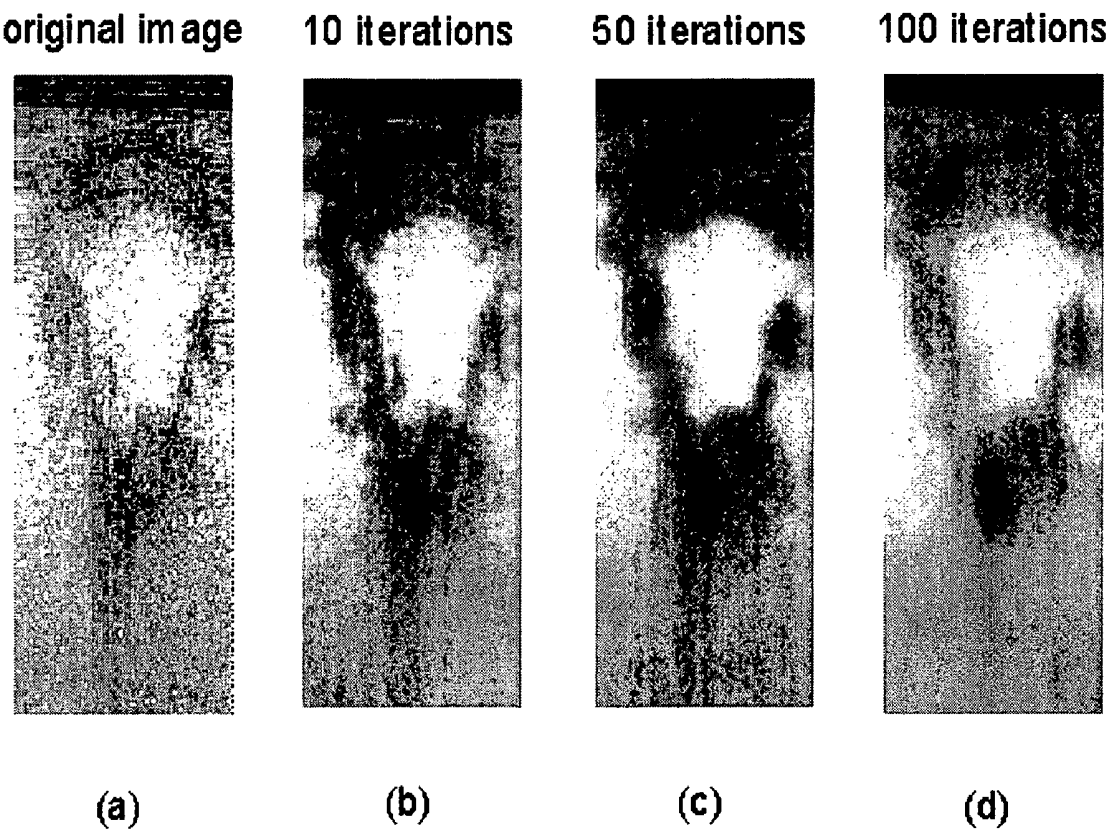
original image
10 iterations
50 iterations
100 iterations
(a)
(b)
(c)
(d)

Fig. 23

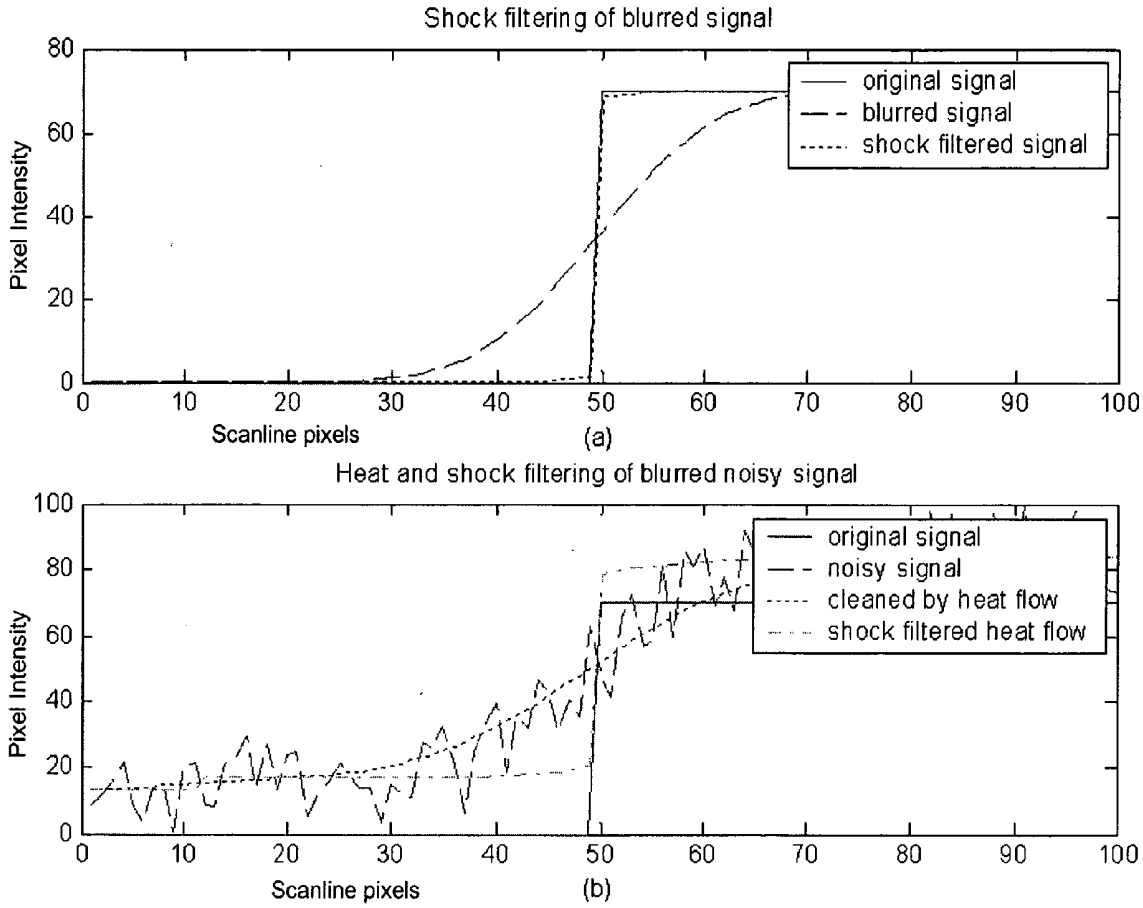
Shock filtering of blurred signal
original signal
blurred signal
shock filtered signal
Pixel Intensity
Scanline pixels
(a)
Heat and shock filtering of blurred noisy signal
original signal
noisy signal
cleaned by heat flow
shock filtered heat flow
Pixel Intensity
Scanline pixels
(b)

Fig. 24

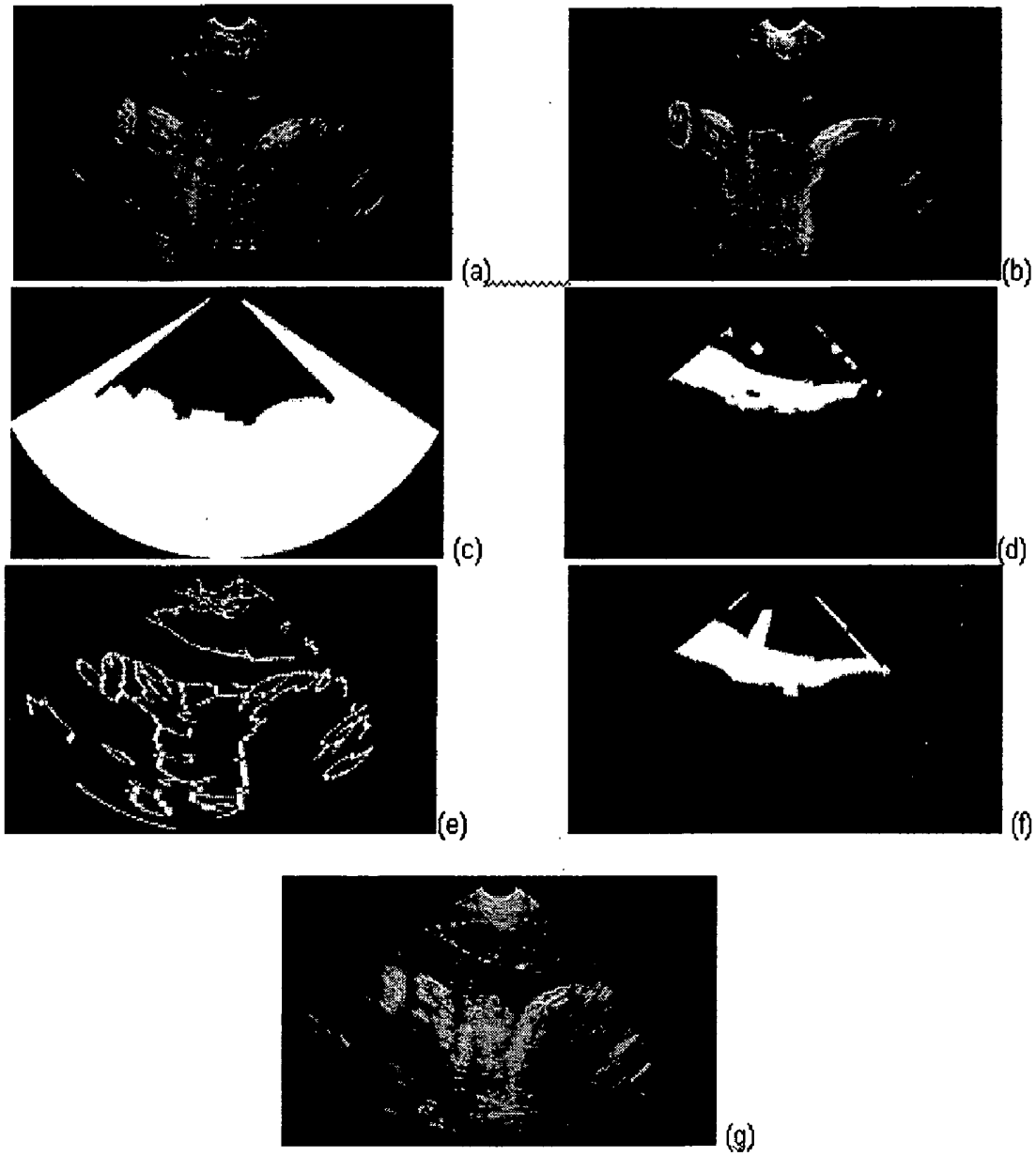


Fig. 25

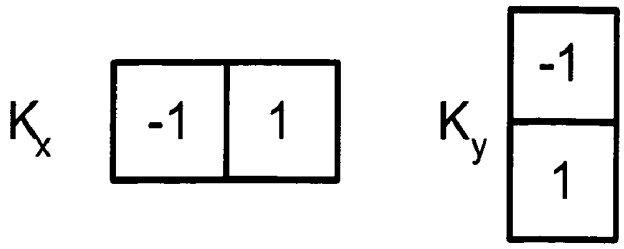


Fig. 26

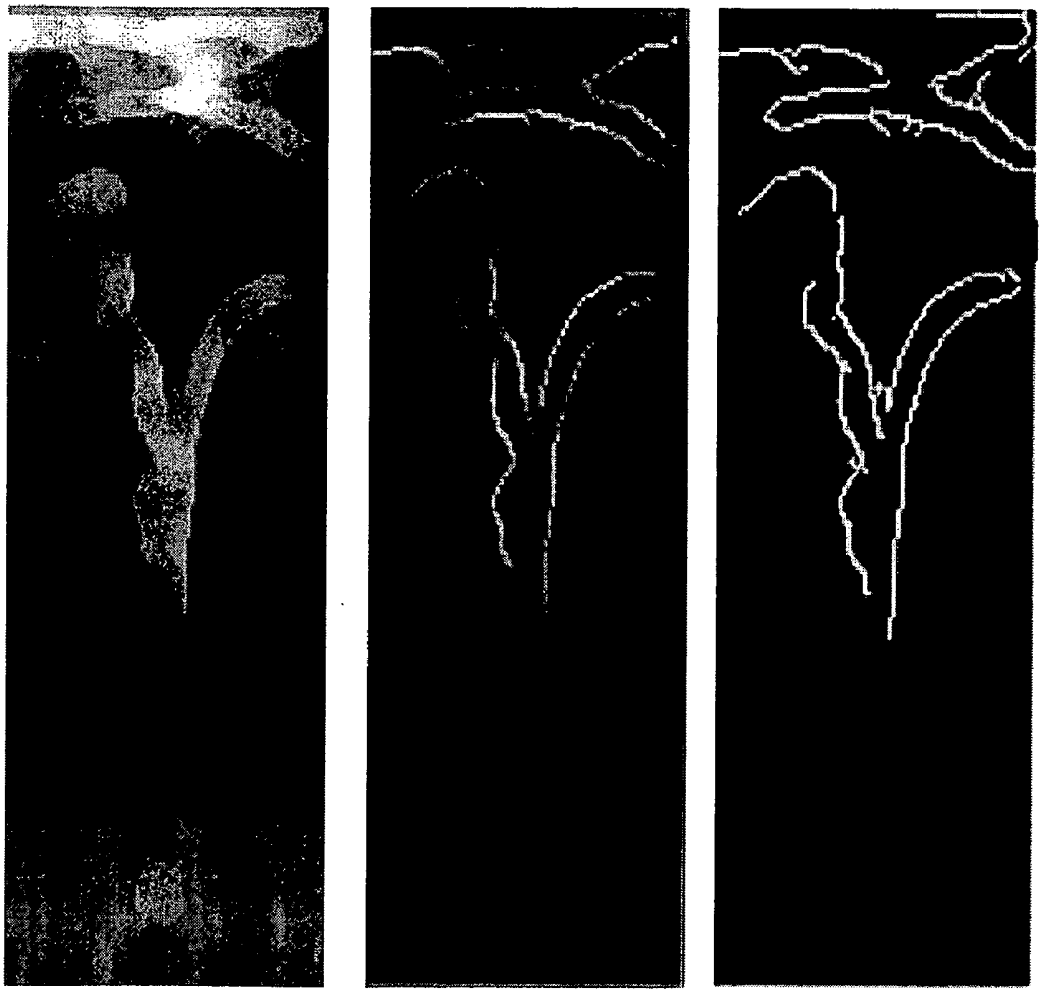

(a) (b) (c)

Fig. 27

# 3D ULTRASOUND-BASED INSTRUMENT FOR NON-INVASIVE MEASUREMENT OF AMNIOTIC FLUID VOLUME

## PRIORITY CLAIM

[0001] This application claims priority to U.S. provisional patent application Ser. No. 60/566,823 filed Apr. 30, 2004.

[0002] This application claims priority to and is a continuation-in-part of U.S. patent application Ser. No. 10/701,955 filed Nov. 5, 2003, which in turn claims priority to and is a continuation-in-part of U.S. patent application Ser. No. 10/443,126 filed May 20, 2003.

[0003] This application is a continuation-in-part of and claims priority to PCT application serial number PCT/US03/24368 filed Aug. 1, 2003, which claims priority to U.S. provisional patent application Ser. No. 60/423,881 filed Nov. 5, 2002 and U.S. provisional patent application Ser. No. 60/400,624 filed Aug. 2, 2002.

[0004] This application is also a continuation-in-part of and claims priority to PCT Application Serial No. PCT/US03/14785 filed May 9, 2003, which is a continuation of U.S. patent application Ser. No. 10/165,556 filed Jun. 7, 2002.

[0005] This application is also a continuation-in-part of and claims priority to U.S. patent application Ser. No. 10/633,186 filed Jul. 7, 2003 which claims priority to U.S. provisional patent application Ser. No. 60/423,881 filed Nov. 5, 2002 and U.S. provisional patent application Ser. No. 60/423,881 filed Aug. 2, 2002, and to U.S. patent application Ser. No. 10/443,126 filed May 20, 2003 which claims priority to U.S. provisional patent application Ser. No. 60/423,881 filed Nov. 5, 2002 and to U.S. provisional application No. 60/400,624 filed Aug. 2, 2002.

[0006] This application also claims priority to U.S. provisional patent application Ser. No. 60/470,525 filed May 12, 2003, and to U.S. patent application Ser. No. 10/165,556 filed Jun. 7, 2002. All of the above applications are herein incorporated by reference in their entirety as if fully set forth herein.

## FIELD OF THE INVENTION

[0007] This invention pertains to the field of obstetrics, particularly to ultrasound-based non-invasive obstetric measurements.

## BACKGROUND OF THE INVENTION

[0008] Measurement of the amount of Amniotic Fluid (AF) volume is critical for assessing the kidney and lung function of a fetus and also for assessing the placental function of the mother. Amniotic fluid volume is also a key measure to diagnose conditions such as polyhydramnios (too much AF) and oligohydramnios (too little AF). Polyhydramnios and oligohydramnios are diagnosed in about 7-8% of all pregnancies and these conditions are of concern because they may lead to birth defects or to delivery complications. The amniotic fluid volume is also one of the important components of the fetal biophysical profile, a major indicator of fetal well-being.

[0009] The currently practiced and accepted method of quantitatively estimating the AF volume is from two-dimensional (2D) ultrasound images. The most commonly used measure is known as the use of the amniotic fluid index (AFI). AFI is the sum of vertical lengths of the largest AF pockets in each of the 4 quadrants. The four quadrants are defined by the umbilicus (the navel) and the linea nigra (the vertical mid-line of the abdomen). The transducer head is placed on the maternal abdomen along the longitudinal axis with the patient in the supine position. This measure was first proposed by Phelan et al (Phelan J P, Smith C V, Broussard P, Small M., "Amniotic fluid volume assessment with the four-quadrant technique at 36-42 weeks' gestation," J Reprod Med Jul; 32(7): 540-2, 1987) and then recorded for a large normal population over time by Moore and Cayle (Moore T R, Cayle J E. "The amniotic fluid index in normal human pregnancy," Am J Obstet Gynecol May; 162(5): 1168-73, 1990).

[0010] Even though the AFI measure is routinely used, studies have shown a very poor correlation of the AFI with the true AF volume (Sepulveda W, Flack N J, Fisk N M., "Direct volume measurement at midtrimester amnioinfusion in relation to ultrasonographic indexes of amniotic fluid volume," Am J Obstet Gynecol Apr; 170(4): 1160-3, 1994). The correlation coefficient was found to be as low as 0.55, even for experienced sonographers. The use of vertical diameter only and the use of only one pocket in each quadrant are two reasons why the AFI is not a very good measure of AF Volume (AFV). Some of the other methods that have been used to estimate AF volume include:

[0011] Dye dilution technique. This is an invasive method where a dye is injected into the AF during amniocentesis and the final concentration of dye is measured from a sample of AF removed after several minutes. This technique is the accepted gold standard for AF volume measurement; however, it is an invasive and cumbersome method and is not routinely used.

[0012] Subjective interpretation from ultrasound images. This technique is obviously dependent on observer experience and has not been found to be very good or consistent at diagnosing oligo- or poly-hydramnios.

[0013] Vertical length of the largest single cord-free pocket. This is an earlier variation of the AFI where the diameter of only one pocket is measured to estimate the AF volume.

[0014] Two-diameter areas of the largest AF pockets in the four quadrants. This is similar to the AFI; however, in this case, two diameters are measured instead of only one for the largest pocket. This two diameter area has been recently shown to be better than AFI or the single pocket measurement in identifying oligohydramnios (Magann E F, Perry K G Jr, Chauhan S P, Anfanger P J, Whitworth N S, Morrison J C., "The accuracy of ultrasound evaluation of amniotic fluid volume in singleton pregnancies: the effect of operator experience and ultrasound interpretative technique," J Clin Ultrasound, Jun; 25(5):249-53, 1997).

[0015] See also: U.S. Pat. No. 6,346,124 to Geiser, et al. (Autonomous Boundary Detection System For Echocardiographic Images). Similarly, the measurement of bladder structures are covered in U.S. Pat. No. 6,213,949 to Ganguly, et al. (System For Estimating Bladder Volume) and U.S. Pat. No. 5,235,985 to McMorrow, et al., (Automatic Bladder Scanning Apparatus). The measurement of fetal

head structures is described in U.S. Pat. No. 5,605,155 to Chalana, et al., (Ultrasound System For Automatically Measuring Fetal Head Size). The measurement of fetal weight is described in U.S. Pat. No. 6,375,616 to Soferman, et al. (Automatic Fetal Weight Determination), Segiv et al. (in Segiv C, Akselrod S, Tepper R., "Application of a semiautomatic boundary detection algorithm for the assessment of amniotic fluid quantity from ultrasound images", Ultrasound Med Biol, May; 25(4): 515-26, 1999), Grover et al. (Grover J, Mentakis E A, Ross M G, "Three-dimensional method for determination of amniotic fluid volume in intrauterine pockets."Obstet Gynecol, Dec; 90(6): 1007-10, 1997). None of the currently used methods for AF volume estimation are ideal. Therefore, there is a need for better, non-invasive, and easier ways to accurately measure amniotic fluid volume.

## SUMMARY OF THE INVENTION

[0016] A preferred form of the invention utilizes a three dimensional (3D) ultrasound-based system and method preferably using a hand-held 3D ultrasound device to acquire at least one 3D data set of a uterus and having one or more, or preferably a plurality of automated processes optimized to accurately and precisely locate and measure the volume of amniotic fluid in the uterus without resorting to pre-supposed models of the shapes of amniotic fluid pockets in ultrasound images. The automated process uses one or more, or preferably a plurality, of algorithms, preferably in a sequence that includes steps for image enhancement, segmentation, and polishing.

## BRIEF DESCRIPTION OF THE DRAWINGS

[0017] **FIG. 1** is a side view of a microprocessor-controlled, hand-held ultrasound transceiver;

[0018] **FIG. 2A** is a is depiction of the hand-held transceiver in use for scanning a patient;

[0019] **FIG. 2B** is a perspective view of the hand-held transceiver device sitting in a communication cradle;

[0020] **FIG. 2C** is a perspective view of an amniotic fluid volume measuring system;

[0021] **FIG. 3** is an alternate embodiment of an amniotic fluid volume measuring system in schematic view of a plurality of transceivers in connection with a server;

[0022] **FIG. 4** is another alternate embodiment of an amniotic fluid volume measuring system in a schematic view of a plurality of transceivers in connection with a server over a network;

[0023] **FIG. 5A** a graphical representation of a plurality of scan lines forming a single scan plane;

[0024] **FIG. 5B** is a graphical representation of a plurality of scanplanes forming a three-dimensional array having a substantially conic shape;

[0025] **FIG. 5C** is a graphical representation of a plurality of 3D distributed scanlines emanating from the transceiver forming a scancone;

[0026] **FIG. 6** is a depiction of the hand-held transceiver placed laterally on a patient trans-abdominally to transmit ultrasound and receive ultrasound echoes for processing to determine amniotic fluid volumes;

[0027] **FIG. 7** shows a block diagram overview of the two-dimensional and three-dimensional Input, Image Enhancement, Intensity-Based Segmentation, Edge-Based Segmentation, Combine, Polish, Output, and Compute algorithms to visualize and determine the volume or area of amniotic fluid;

[0028] **FIG. 8A** depicts the sub-algorithms of Image Enhancement;

[0029] **FIG. 8B** depicts the sub-algorithms of Intensity-Based Segmentation;

[0030] **FIG. 8C** depicts the sub-algorithms of Edge-Based Segmentation;

[0031] **FIG. 8D** depicts the sub-algorithms of the Polish algorithm, including Close, Open, Remove Deep Regions, and Remove Fetal Head Regions;

[0032] **FIG. 8E** depicts the sub-algorithms of the Remove Fetal Head Regions sub-algorithm;

[0033] **FIG. 8F** depicts the sub-algorithms of the Hough Transform sub-algorithm;

[0034] **FIG. 9** depicts the operation of a circular Hough transform algorithm;

[0035] **FIG. 10** shows results of sequentially applying the algorithm steps on a sample image;

[0036] **FIG. 11** illustrates a set of intermediate images of the fetal head detection process;

[0037] **FIG. 12** presents a 4-panel series of sonographer amniotic fluid pocket outlines and the algorithm output amniotic fluid pocket outlines;

[0038] **FIG. 13** illustrates a 4-quadrant supine procedure to acquire multiple image cones;

[0039] **FIG. 14** illustrates an in-line lateral line procedure to acquire multiple image cones;

[0040] **FIG. 15** is a block diagram overview of the rigid registration and correcting algorithms used in processing multiple image cone data sets;

[0041] **FIG. 16** is a block diagram of the steps in the rigid registration algorithm;

[0042] **FIG. 17A** is an example image showing a first view of a fixed scanplane;

[0043] **FIG. 17B** is an example image showing a second view view of a moving scanplane having some voxels in common with the first scanplane;

[0044] **FIG. 17C** is a composite image of the first (fixed) and second (moving) images;

[0045] **FIG. 18A** is an example image showing a first view of a fixed scanplane;

[0046] **FIG. 18B** is an example image showing a second view of a moving scanplane having some voxels in common with the first view and a third view;

[0047] **FIG. 18C** is a third view of a moving scanplane having some voxels in common with the second view;

[0048] **FIG. 18D** is a composite image of the first (fixed), second (moving), and third (moving) views;

[0049] **FIG. 19** illustrates a 6-section supine procedure to acquire multiple image cones around the center point of uterus of a patient in a supine procedure;

[0050] **FIG. 20** is a block diagram algorithm overview of the registration and correcting algorithms used in processing the 6-section multiple image cone data sets depicted in **FIG. 19**;

[0051] **FIG. 21** is an expansion of the Image Enhancement and Segmentation block **1010** of **FIG. 20**;

[0052] **FIG. 22** is an expansion of the RigidRegistration block **1014** of **FIG. 20**;

[0053] **FIG. 23** is a 4-panel image set that shows the effect of multiple iterations of the heat filter applied to an original image;

[0054] **FIG. 24** shows the affect of shock filtering and a combination heat-and-shock filtering to the pixel values of the image;

[0055] **FIG. 25** is a 7-panel image set progressively receiving application of the image enhancement and segmentation algorithms of **FIG. 21**;

[0056] **FIG. 26** is a pixel difference kernel for obtaining X and Y derivatives to determine pixel gradient magnitudes for edge-based segmentation; and

[0057] **FIG. 27** is a 3-panel image set showing the progressive demarcation or edge detection of organ wall interfaces arising from edge-based segmentation algorithms.

## DETAILED DESCRIPTION OF THE PREFERRED EMBODIMENT

[0058] Preferably, a hand-held 3D ultrasound device is used to image the uterus trans-abdominally. The user moves the device around on the maternal abdomen and, using 2D image processing to locate the amniotic fluid areas, the device gives feedback to the user about where to acquire the 3D image data sets. The user acquires one or more 3D image data sets covering all of the amniotic fluid in the uterus and the data sets are then stored in the device or transferred to a host computer.

[0059] The 3D ultrasound device is configured to acquire the 3D image data sets in two formats. The first format is a collection of two-dimensional scanplanes, each scanplane being separated from the other and representing a portion of the uterus being scanned. Each scanplane is formed from one-dimensional ultrasound A-lines confined within the limits of the 2D scanplane. The 3D data sets is then represented as a 3D array of 2D scanplanes. The 3D array of 2D scanplanes is an assembly of scanplanes, and may be assembled into a translational array, a wedge array, or a rotatational array.

[0060] Alternatively, the 3D ultrasound device is configured to acquire the 3D image data sets from one-dimensional ultrasound A-lines distributed in 3D space of the uterus to form a 3D scancone of 3D-distributed scanline. The 3D scancone is not an assembly of 2D scanplanes.

[0061] The 3D image datasets, either as discrete scanplanes or 3D distributed scanlines, are then subjected to image enhancement and analysis processes. The processes are either implemented on the device itself or are implemented on the host computer. Alternatively, the processes can also be implemented on a server or other computer to which the 3D ultrasound data sets are transferred.

[0062] In a preferred image enhancement process, each 2D image in the 3D dataset is first enhanced using non-linear filters by an image pre-filtering step. The image pre-filtering step includes an image-smoothing step to reduce image noise followed by an image-sharpening step to obtain maximum contrast between organ wall boundaries.

[0063] A second process includes subjecting the resulting image of the first process to a location method to identify initial edge points between amniotic fluid and other fetal or maternal structures. The location method automatically determines the leading and trailing regions of wall locations along an A-mode one-dimensional scan line.

[0064] A third process includes subjecting the image of the first process to an intensity-based segmentation process where dark pixels (representing fluid) are automatically separated from bright pixels (representing tissue and other structures).

[0065] In a fourth process, the images resulting from the second and third step are combined to result in a single image representing likely amniotic fluid regions.

[0066] In a fifth process, the combined image is cleaned to make the output image smooth and to remove extraneous structures such as the fetal head and the fetal bladder.

[0067] In a sixth process, boundary line contours are placed on each 2D image. Thereafter, the method then calculates the total 3D volume of amniotic fluid in the uterus.

[0068] In cases in which uteruses are too large to fit in a single 3D array of 2D scanplanes or a single 3D scancone of 3D distributed scanlines, especially as occurs during the second and third trimester of pregnancy, preferred alternate embodiments of the invention allow for acquiring at least two 3D data sets, preferably four, each 3D data set having at least a partial ultrasonic view of the uterus, each partial view obtained from a different anatomical site of the patient.

[0069] In one embodiment a 3D array of 2D scanplanes is assembled such that the 3D array presents a composite image of the uterus that displays the amniotic fluid regions to provide the basis for calculation of amniotic fluid volumes. In a preferred alternate embodiment, the user acquires the 3D data sets in quarter sections of the uterus when the patient is in a supine position. In this 4-quadrant supine procedure, four image cones of data are acquired near the midpoint of each uterine quadrant at substantially equally spaced intervals between quadrant centers. Image processing as outlined above is conducted for each quadrant image, segmenting on the darker pixels or voxels associated with amniotic fluid. Correcting algorithms are applied to compensate for any quadrant-to-quadrant image cone overlap by registering and fixing one quadrant's image to another. The result is a fixed 3D mosaic image of the uterus and the amniotic fluid volumes or regions in the uterus from the four separate image cones.

[0070] Similarly, in another preferred alternate embodiment, the user acquires one or more 3D image data sets of quarter sections of the uterus when the patient is in a lateral position. In this multi-image cone lateral procedure, each

image's cones of data are acquired along a lateral line of substantially equally spaced intervals. Each image cone is subjected to the image processing as outlined above, with emphasis given to segmenting on the darker pixels or voxels associated with amniotic fluid. Scanplanes showing common pixel or voxel overlaps are registered into a common coordinate system along the lateral line. Correcting algorithms are applied to compensate for any image cone overlap along the lateral line. The result is a fixed 3D mosaic image of the uterus and the amniotic fluid volumes or regions in the uterus from the four separate image cones.

[0071] In yet other preferred embodiments, at least two 3D scancone of 3D distributed scanlines are acquired at different anatomical sites, image processed, registered and fused into a 3D mosaic image composite. Amniotic fluid volumes are then calculated.

[0072] The system and method further provides an automatic method to detect and correct for any contribution the fetal head provides to the amniotic fluid volume.

[0073] The preferred portable embodiment of the ultrasound transceiver of the amniotic fluid volume measuring system are shown in **FIGS. 1-4**. The transceiver **10** includes a handle **12** having a trigger **14** and a top button **16**, a transceiver housing **18** attached to the handle **12**, and a transceiver dome **20**. A display **24** for user interaction is attached to the transceiver housing **18** at an end opposite the transceiver dome **20**. Housed within the transceiver **10** is a single element transducer (not shown) that converts ultrasound waves to electrical signals. The transceiver **10** is held in position against the body of a patient by a user for image acquisition and signal processing. In operation, the transceiver **10** transmits a radio frequency ultrasound signal at substantially 3.7 MHz to the body and then receives a returning echo signal. To accommodate different patients having a variable range of obesity, the transceiver **10** can be adjusted to transmit a range of probing ultrasound energy from approximately 2 MHz to approximately 10 MHz radio frequencies.

[0074] The top button **16** selects for different acquisition volumes. The transceiver is controlled by a microprocessor and software associated with the microprocessor and a digital signal processor of a computer system. As used in this invention, the term "computer system" broadly comprises any microprocessor-based or other computer system capable of executing operating instructions and manipulating data, and is not limited to a traditional desktop or notebook computer. The display **24** presents alphanumeric or graphic data indicating the proper or optimal positioning of the transceiver **10** for initiating a series of scans. The transceiver **10** is configured to initiate the series of scans to obtain and present 3D images as either a 3D array of 2D scanplanes or as a single 3D scancone of 3D distributed scanlines. A suitable transceiver is the DCD372 made by Diagnostic Ultrasound. In alternate embodiments, the two- or three-dimensional image of a scan plane may be presented in the display **24**.

[0075] Although the preferred ultrasound transceiver is described above, other transceivers may also be used. For example, the transceiver need not be battery-operated or otherwise portable, need not have a top-mounted display **24**, and may include many other features or differences. The display **24** may be a liquid crystal display (LCD), a light emitting diode (LED), a cathode ray tube (CRT), or any suitable display capable of presenting alphanumeric data or graphic images.

[0076] **FIG. 2A** is a photograph of the hand-held transceiver **10** for scanning a patient. The transceiver **10** is then positioned over the patient's abdomen by a user holding the handle **12** to place the transceiver housing **18** against the patient's abdomen. The top button **16** is centrally located on the handle **12**. Once optimally positioned over the abdomen for scanning, the transceiver **10** transmits an ultrasound signal at substantially 3.7 MHz into the uterus. The transceiver **10** receives a return ultrasound echo signal emanating from the uterus and presents it on the display **24**.

[0077] **FIG. 2B** is a perspective view of the hand-held transceiver device sitting in a communication cradle. The transceiver **10** sits in a communication cradle **42** via the handle **12**. This cradle can be connected to a standard USB port of any personal computer, enabling all the data on the device to be transferred to the computer and enabling new programs to be transferred into the device from the computer.

[0078] **FIG. 2C** is a perspective view of an amniotic fluid volume measuring system **5**A. The system **5**A includes the transceiver **10** cradled in the cradle **42** that is in signal communication with a computer **52**. The transceiver **10** sits in a communication cradle **42** via the handle **12**. This cradle can be connected to a standard USB port of any personal computer **52**, enabling all the data on the transceiver **10** to be transferred to the computer for analysis and determination of amniotic fluid volume.

[0079] **FIG. 3** depicts an alternate embodiment of an amniotic fluid volume measuring system **5**B in a schematic view. The system **5**B includes a plurality systems **5**A in signal communication with a server **56**. As illustrated each transceiver **10** is in signal connection with the server **56** through connections via a plurality of computers **52**. **FIG. 3**, by example, depicts each transceiver **10** being used to send probing ultrasound radiation to a uterus of a patient and to subsequently retrieve ultrasound echoes returning from the uterus, convert the ultrasound echoes into digital echo signals, store the digital echo signals, and process the digital echo signals by algorithms of the invention. A user holds the transceiver **10** by the handle **12** to send probing ultrasound signals and to receive incoming ultrasound echoes. The transceiver **10** is placed in the communication cradle **42** that is in signal communication with a computer **52**, and operates as an amniotic fluid volume measuring system. Two amniotic fluid volume-measuring systems are depicted as representative though fewer or more systems may be used. As used in this invention, a "server" can be any computer software or hardware that responds to requests or issues commands to or from a client. Likewise, the server may be accessible by one or more client computers via the Internet, or may be in communication over a LAN or other network.

[0080] Preferred amniotic fluid volume measuring systems include the transceiver **10** for acquiring data from a patient. The transceiver **10** is placed in the cradle **52** to establish signal communication with the computer **52**. Signal communication as illustrated is, in one embodiment, by a wired connection from the cradle **42** to the computer **52**. Signal communication between the transceiver **10** and the computer **52** may also be by wireless means, for example,

infrared signals or radio frequency signals. The wireless means of signal communication may occur between the cradle **42** and the computer **52**, the transceiver **10** and the computer **52**, or the transceiver **10** and the cradle **42**.

[**0081**] A preferred first embodiment of the amniotic fluid volume measuring system includes each transceiver **10** being separately used on a patient and sending signals proportionate to the received and acquired ultrasound echoes to the computer **52** for storage. Residing in each computer **52** are imaging programs having instructions to prepare and analyze a plurality of one dimensional (1D) images from the stored signals and transforms the plurality of 1D images into the plurality of 2D scanplanes. The imaging programs also present 3D renderings from the plurality of 2D scanplanes. Also residing in each computer **52** are instructions to perform the additional ultrasound image enhancement procedures, including instructions to implement the image processing algorithms.

[**0082**] A preferred second embodiment of the amniotic fluid volume measuring system is similar to the first embodiment, but the imaging programs and the instructions to perform the additional ultrasound enhancement procedures are located on the server **56**. Each computer **52** from each amniotic fluid volume measuring system receives the acquired signals from the transceiver **10** via the cradle **51** and stores the signals in the memory of the computer **52**. The computer **52** subsequently retrieves the imaging programs and the instructions to perform the additional ultrasound enhancement procedures from the server **56**. Thereafter, each computer **52** prepares the 1D images, 2D images, 3D renderings, and enhanced images from the retrieved imaging and ultrasound enhancement procedures. Results from the data analysis procedures are sent to the server **56** for storage.

[**0083**] A preferred third embodiment of the amniotic fluid volume measuring system is similar to the first and second embodiments, but the imaging programs and the instructions to perform the additional ultrasound enhancement procedures are located on the server **56** and executed on the server **56**. Each computer **52** from each amniotic fluid volume measuring system receives the acquired signals from the transceiver **10** and via the cradle **51** sends the acquired signals in the memory of the computer **52**. The computer **52** subsequently sends the stored signals to the server **56**. In the server **56**, the imaging programs and the instructions to perform the additional ultrasound enhancement procedures are executed to prepare the 1D images, 2D images, 3D renderings, and enhanced images from the server **56** stored signals. Results from the data analysis procedures are kept on the server **56**, or alternatively, sent to the computer **52**.

[**0084**] **FIG. 4** is another embodiment of an amniotic volume fluid measuring system **5**C presented in schematic view. The system **5**C includes a plurality of amniotic fluid measuring systems **5**A connected to a server **56** over the Internet or other network **64**. **FIG. 4** represents any of the first, second, or third embodiments of the invention advantageously deployed to other servers and computer systems through connections via the network.

[**0085**] **FIG. 5A** a graphical representation of a plurality of scan lines forming a single scan plane. **FIG. 5A** illustrates how ultrasound signals are used to make analyzable images, more specifically how a series of one-dimensional (1D) scanlines are used to produce a two-dimensional (2D) image. The 1D and 2D operational aspects of the single element transducer housed in the transceiver **10** is seen as it rotates mechanically about an angle $\phi$. A scanline **214** of length r migrates between a first limiting position **218** and a second limiting position **222** as determined by the value of the angle $\phi$, creating a fan-like 2D scanplane **210**. In one preferred form, the transceiver **10** operates substantially at 3.7 MHz frequency and creates an approximately 18 cm deep scan line **214** and migrates within the angle $\phi$ having an angle of approximately 0.027 radians. A first motor tilts the transducer approximately 60° clockwise and then counterclockwise forming the fan-like 2D scanplane presenting an approximate 120° 2D sector image. A plurality of scanlines, each scanline substantially equivalent to scanline **214** is recorded, between the first limiting position **218** and the second limiting position **222** formed by the unique tilt angle $\phi$. The plurality of scanlines between the two extremes forms a scanplane **210**. In the preferred embodiment, each scanplane contains 77 scan lines, although the number of lines can vary within the scope of this invention. The tilt angle $\phi$ sweeps through angles approximately between −60° and +60° for a total arc of approximately 120°.

[**0086**] **FIG. 5B** is a graphical representation of a plurality of scanplanes forming a three-dimensional array (3D) **240** having a substantially conic shape. **FIG. 5B** illustrates how a 3D rendering is obtained from the plurality of 2D scanplanes. Within each scanplane **210** are the plurality of scanlines, each scanline equivalent to the scanline **214** and sharing a common rotational angle $\theta$. In the preferred embodiment, each scanplane contains 77 scan lines, although the number of lines can vary within the scope of this invention. Each 2D sector image scanplane **210** with tilt angle $\phi$ and range r (equivalent to the scanline **214**) collectively forms a 3D conic array **240** with rotation angle $\theta$. After gathering the 2D sector image, a second motor rotates the transducer between 3.75° or 7.5° to gather the next 120° sector image. This process is repeated until the transducer is rotated through 180°, resulting in the cone-shaped 3D conic array **240** data set with 24 planes rotationally assembled in the preferred embodiment. The conic array could have fewer or more planes rotationally assembled. For example, preferred alternate embodiments of the conic array could include at least two scanplanes, or a range of scanplanes from 2 to 48 scanplanes. The upper range of the scanplanes can be greater than 48 scanplanes. The tilt angle $\phi$ indicates the tilt of the scanline from the centerline in 2D sector image, and the rotation angle $\theta$, identifies the particular rotation plane the sector image lies in. Therefore, any point in this 3D data set can be isolated using coordinates expressed as three parameters, $P(r, \phi, \theta)$.

[**0087**] As the scanlines are transmitted and received, the returning echoes are interpreted as analog electrical signals by a transducer, converted to digital signals by an analog-to-digital converter, and conveyed to the digital signal processor of the computer system for storage and analysis to determine the locations of the amniotic fluid walls. The computer system is representationally depicted in **FIGS. 3 and 4** and includes a microprocessor, random access memory (RAM), or other memory for storing processing instructions and data generated by the transceiver **10**.

[**0088**] **FIG. 5C** is a graphical representation of a plurality of 3D-distributed scanlines emanating from the transceiver **10** forming a scancone **300**. The scancone **300** is formed by

a plurality of 3D distributed scanlines that comprises a plurality of internal and peripheral scanlines. The scanlines are one-dimensional ultrasound A-lines that emanate from the transceiver **10** at different coordinate directions, that taken as an aggregate, from a conic shape. The 3D-distributed A-lines (scanlines) are not necessarily confined within a scanplane, but instead are directed to sweep throughout the internal and along the periphery of the scancone **300**. The 3D-distributed scanlines not only would occupy a given scanplane in a 3D array of 2D scanplanes, but also the inter-scanplane spaces, from the conic axis to and including the conic periphery. The transceiver **10** shows the same illustrated features from **FIG. 1**, but is configured to distribute the ultrasound A-lines throughout 3D space in different coordinate directions to form the scancone **300**.

[**0089**] The internal scanlines are represented by scanlines **312**A-C. The number and location of the internal scanlines emanating from the transceiver **10** is the number of internal scanlines needed to be distributed within the scancone **300**, at different positional coordinates, to sufficiently visualize structures or images within the scancone **300**. The internal scanlines are not peripheral scanlines. The peripheral scanlines are represented by scanlines **314**A-F and occupy the conic periphery, thus representing the peripheral limits of the scancone **300**.

[**0090**] **FIG. 6** is a depiction of the hand-held transceiver placed on a patient trans-abdominally to transmit probing ultrasound and receive ultrasound echoes for processing to determine amniotic fluid volumes. The transceiver **10** is held by the handle **12** to position over a patient to measure the volume of amniotic fluid in an amniotic sac over a baby. A plurality of axes for describing the orientation of the baby, the amniotic sac, and mother is illustrated. The plurality of axes includes a vertical axis depicted on the line L(R)-L(L) for left and right orientations, a horizontal axis LI-LS for inferior and superior orientations, and a depth axis LA-LP for anterior and posterior orientations.

[**0091**] **FIG. 6** is representative of a preferred data acquisition protocol used for amniotic fluid volume determination. In this protocol, the transceiver **10** is the hand-held 3D ultrasound device (for example, model DCD372 from Diagnostic Ultrasound) and is used to image the uterus trans-abdominally. Initially during the targeting phase, the patient is in a supine position and the device is operated in a 2D continuous acquisition mode. A 2D continuous mode is where the data is continuously acquired in 2D and presented as a scanplane similar to the scanplane **210** on the display **24** while an operator physically moves the transceiver **10**. An operator moves the transceiver **10** around on the maternal abdomen and the presses the trigger **14** of the transceiver **10** and continuously acquires real-time feedback presented in 2D on the display **24**. Amniotic fluid, where present, visually appears as dark regions along with an alphanumeric indication of amniotic fluid area (for example, in $cm^2$) on the display **24**. Based on this real-time information in terms of the relative position of the transceiver **10** to the fetus, the operator decides which side of the uterus has more amniotic fluid by the presentation on the display **24**. The side having more amniotic fluid presents as regions having larger darker regions on the display **24**. Accordingly, the side displaying a large dark region registers greater alphanumeric area while the side with less fluid shows displays smaller dark regions and proportionately registers smaller alphanumeric area on the display **24**. While amniotic fluid is present throughout the uterus, its distribution in the uterus depends upon where and how the fetus is positioned within the uterus. There is usually less amniotic fluid around the fetus's spine and back and more amniotic fluid in front of its abdomen and around the limbs.

[**0092**] Based on fetal position information acquired from data gathered under continuous acquisition mode, the patient is placed in a lateral recumbent position such that the fetus is displaced towards the ground creating a large pocket of amniotic fluid close to abdominal surface where the transceiver **10** can be placed as shown in **FIG. 6**. For example, if large fluid pockets are found on the right side of the patient, the patient is asked to turn with the left side down and if large fluid pockets are found on the left side, the patient is asked to turn with the right side down.

[**0093**] After the patient has been placed in the desired position, the transceiver **10** is again operated in the 2D continuous acquisition mode and is moved around on the lateral surface of the patient's abdomen. The operator finds the location that shows the largest amniotic fluid area based on acquiring the largest dark region imaged and the largest alphanumeric value displayed on the display **24**. At the lateral abdominal location providing the largest dark region, the transceiver **10** is held in a fixed position, the trigger **14** is released to acquire a 3D image comprising a set of arrayed scanplanes. The 3D image presents a rotational array of the scanplanes **210** similar to the 3D array **240**.

[**0094**] In a preferred alternate data acquisition protocol, the operator can reposition the transceiver **10** to different abdominal locations to acquire new 3D images comprised of different scanplane arrays similar to the 3D array **240**. Multiple scan cones obtained from different positions provide the operator the ability to image the entire amniotic fluid region from different view points. In the case of a single image cone being too small to accommodate a large AFV measurement, obtaining multiple 3D array **240** image cones ensures that the total volume of large AFV regions is determined. Multiple 3D images may also be acquired by pressing the top bottom **16** to select multiple conic arrays similar to the 3D array **240**.

[**0095**] Depending on the position of the fetus relative to the location of the transceiver **10**, a single image scan may present an underestimated volume of AFV due to amniotic fluid pockets that remain hidden behind the limbs of the fetus. The hidden amniotic fluid pockets present as unquantifiable shadow-regions.

[**0096**] To guard against underestimating AFV, repeated positioning the transceiver **10** and rescanning can be done to obtain more than one ultrasound view to maximize detection of amniotic fluid pockets. Repositioning and rescanning provides multiple views as a plurality of the 3D arrays **240** images cones. Acquiring multiple images cones improves the probability of obtaining initial estimates of AFV that otherwise could remain undetected and un-quantified in a single scan.

[**0097**] In an alternative scan protocol, the user determines and scans at only one location on the entire abdomen that shows the maximum amniotic fluid area while the patient is the supine position. As before, when the user presses the top button **16**, 2D scanplane images equivalent to the scanplane

**210** are continuously acquired and the amniotic fluid area on every image is automatically computed. The user selects one location that shows the maximum amniotic fluid area. At this location, as the user releases the scan button, a full 3D data cone is acquired and stored in the device's memory.

[**0098**] **FIG. 7** shows a block diagram overview the image enhancement, segmentation, and polishing algorithms of the amniotic fluid volume measuring system. The enhancement, segmentation, and polishing algorithms are applied to each scanplane **210** or to the entire scan cone **240** to automatically obtain amniotic fluid regions. For scanplanes substantially equivalent to scanplane **210**, the algorithms are expressed in two-dimensional terms and use formulas to convert scanplane pixels (picture elements) into area units. For the scan cones substantially equivalent to the 3D conic array **240**, the algorithms are expressed in three-dimensional terms and use formulas to convert voxels (volume elements) into volume units.

[**0099**] The algorithms expressed in 2D terms are used during the targeting phase where the operator trans-abdominally positions and repositions the transceiver **10** to obtain real-time feedback about the amniotic fluid area in each scanplane. The algorithms expressed in 3D terms are used to obtain the total amniotic fluid volume computed from the voxels contained within the calculated amniotic fluid regions in the 3D conic array **240**.

[**0100**] **FIG. 7** represents an overview of a preferred method of the invention and includes a sequence of algorithms, many of which have sub-algorithms described in more specific detail in FIGS. **8**A-F. **FIG. 7** begins with inputting data of an unprocessed image at step **410**. After unprocessed image data **410** is entered (e.g., read from memory, scanned, or otherwise acquired), it is automatically subjected to an image enhancement algorithm **418** that reduces the noise in the data (including speckle noise) using one or more equations while preserving the salient edges on the image using one or more additional equations. Next, the enhanced images are segmented by two different methods whose results are eventually combined. A first segmentation method applies an intensity-based segmentation algorithm **422** that determines all pixels that are potentially fluid pixels based on their intensities. A second segmentation method applies an edge-based segmentation algorithm **438** that relies on detecting the fluid and tissue interfaces. The images obtained by the first segmentation algorithm **422** and the images obtained by the second segmentation algorithm **438** are brought together via a combination algorithm **442** to provide a substantially segmented image. The segmented image obtained from the combination algorithm **442** are then subjected to a polishing algorithm **464** in which the segmented image is cleaned-up by filling gaps with pixels and removing unlikely regions. The image obtained from the polishing algorithm **464** is outputted **480** for calculation of areas and volumes of segmented regions-of-interest. Finally the area or the volume of the segmented region-of-interest is computed **484** by multiplying pixels by a first resolution factor to obtain area, or voxels by a second resolution factor to obtain volume. For example, for pixels having a size of 0.8 mm by 0.8 mm, the first resolution or conversion factor for pixel area is equivalent to 0.64 $mm^2$, and the second resolution or conversion factor for voxel volume is equivalent to 0.512 $mm^3$. Different unit lengths for pixels and voxels may be assigned, with a proportional change in pixel area and voxel volume conversion factors.

[**0101**] The enhancement, segmentation and polishing algorithms depicted in **FIG. 7** for measuring amniotic fluid areas or volumes are not limited to scanplanes assembled into rotational arrays equivalent to the 3D array **240**. As additional examples, the enhancement, segmentation and polishing algorithms depicted in **FIG. 7** apply to translation arrays and wedge arrays. Translation arrays are substantially rectilinear image plane slices from incrementally repositioned ultrasound transceivers that are configured to acquire ultrasound rectilinear scanplanes separated by regular or irregular rectilinear spaces. The translation arrays can be made from transceivers configured to advance incrementally, or may be hand-positioned incrementally by an operator. The operator obtains a wedge array from ultrasound transceivers configured to acquire wedge-shaped scanplanes separated by regular or irregular angular spaces, and either mechanistically advanced or hand-tilted incrementally. Any number of scanplanes can be either translationally assembled or wedge-assembled ranges, but preferably in ranges greater than 2 scanplanes.

[**0102**] Other preferred embodiments of the enhancement, segmentation and polishing algorithms depicted in **FIG. 7** may be applied to images formed by line arrays, either spiral distributed or reconstructed random-lines. The line arrays are defined using points identified by the coordinates expressed by the three parameters, $P(r, \phi, \theta)$, where the values or r, $\phi$, and $\theta$ can vary.

[**0103**] The enhancement, segmentation and polishing algorithms depicted in **FIG. 7** are not limited to ultrasound applications but may be employed in other imaging technologies utilizing scanplane arrays or individual scanplanes. For example, biological-based and non-biological-based images acquired using infrared, visible light, ultraviolet light, microwave, x-ray computed tomography, magnetic resonance, gamma rays, and positron emission are images suitable for the algorithms depicted in **FIG. 7**. Furthermore, the algorithms depicted in **FIG. 7** can be applied to facsimile transmitted images and documents.

[**0104**] FIGS. **8**A-E depict expanded details of the preferred embodiments of enhancement, segmentation, and polishing algorithms described in **FIG. 7**. Each of the following greater detailed algorithms are either implemented on the transceiver **10** itself or are implemented on the host computer **52** or on the server **56** computer to which the ultrasound data is transferred.

[**0105**] **FIG. 8A** depicts the sub-algorithms of Image Enhancement. The sub-algorithms include a heat filter **514** to reduce noise and a shock filter **518** to sharpen edges. A combination of the heat and shock filters works very well at reducing noise and sharpening the data while preserving the significant discontinuities. First, the noisy signal is filtered using a 1D heat filter (Equation E1 below), which results in the reduction of noise and smoothing of edges. This step is followed by a shock-filtering step **518** (Equation E2 below), which results in the sharpening of the blurred signal. Noise reduction and edge sharpening is achieved by application of the following equations E1-E2. The algorithm of the heat filter **514** uses a heat equation E1. The heat equation E1 in partial differential equation (PDE) form for image processing is expressed as:

$$\frac{\partial u}{\partial t} = \frac{\partial^2 u}{\partial x^2} + \frac{\partial^2 u}{\partial y^2},$$

[0106] where u is the image being processed. The image u is 2D, and is comprised of an array of pixels arranged in rows along the x-axis, and an array of pixels arranged in columns along the y-axis. The pixel intensity of each pixel in the image u has an initial input image pixel intensity (I) defined as $u_0$=I. The value of I depends on the application, and commonly occurs within ranges consistent with the application. For example, I can be as low as 0 to 1, or occupy middle ranges between 0 to 127 or 0 to 512. Similarly, I may have values occupying higher ranges of 0 to 1024 and 0 to 4096, or greater. The heat equation E1 results in a smoothing of the image and is equivalent to the Gaussian filtering of the image. The larger the number of iterations that it is applied for the more the input image is smoothed or blurred and the more the noise that is reduced.

[0107] The shock filter **518** is a PDE used to sharpen images as detailed below. The two dimensional shock filter E2 is expressed as:

$$\frac{\partial u}{\partial t} = -F(l(u))\|\nabla u\|, \qquad \text{E2}$$

[0108] where u is the image processed whose initial value is the input image pixel intensity (I): $u_0$=I where the l(u) term is the Laplacian of the image u, F is a function of the Laplacian, and $\|\nabla u\|$ is the 2D gradient magnitude of image intensity defined by equation E3.

$$\|\nabla u\| = \sqrt{u_x^2 + u_y^2}, \qquad \text{E3}$$

[0109] where

[0110] $u^2_x$=the square of the partial derivative of the pixel intensity (u) along the x-axis,

[0111] $u^2_y$=the square of the partial derivative of the pixel intensity (u) along the y-axis,

[0112] the Laplacian l(u) of the image, u, is expressed in equation E4 as

$$l(u) = u_{xx}u_x^2 + 2u_{xy}u_xu_y + u_{yy}u_y^2 \qquad \text{E4}$$

[0113] where equation E4 relates to equation E1 as follows:

[0114] $u_x$ is the first partial derivative

$$\frac{\partial u}{\partial x}$$

[0115] of u along the x-axis,

[0116] $u_y$ is the first partial derivative

$$\frac{\partial u}{\partial y}$$

[0117] of u along the y-axis,

[0118] $u_x^2$ is the square of the first partial derivative

$$\frac{\partial u}{\partial x}$$

[0119] of u along the x-axis,

[0120] $u_y^2$ is the square of the first partial derivative

$$\frac{\partial u}{\partial y}$$

[0121] of u along the y-axis,

[0122] $u_{xx}$ is the second partial derivative

$$\frac{\partial^2 u}{\partial x^2}$$

[0123] of u along the x-axis,

[0124] $u_{yy}$ is the second partial derivative

$$\frac{\partial^2 u}{\partial y^2}$$

[0125] of u along the y-axis,

[0126] $u_{xy}$ is cross multiple first partial derivative

$$\frac{\partial u}{\partial x dy}$$

[0127] of u along the x and y axes, and

[0128] the sign of the function F modifies the Laplacian by the image gradient values selected to avoid placing spurious edges at points with small gradient values:

$$\begin{aligned} F(l(u)) &= 1, && \text{if } l(u) > 0 \text{ and } \|\nabla u\| > t \\ &= -1, && \text{if } l(u) < 0 \text{ and } \|\nabla u\| > t \\ &= 0, && \text{otherwise} \end{aligned}$$

[0129] where t is a threshold on the pixel gradient value $\|\nabla u\|$.

[0130] The combination of heat filtering and shock filtering produces an enhanced image ready to undergo the intensity-based and edge-based segmentation algorithms as discussed below.

[0131] **FIG. 8B** depicts the sub-algorithms of Intensity-Based Segmentation (step **422** in **FIG. 7**). The intensity-based segmentation step **422** uses a "k-means" intensity clustering **522** technique where the enhanced image is subjected to a categorizing "k-means" clustering algorithm. The "k-means" algorithm categorizes pixel intensities into white, gray, and black pixel groups. Given the number of desired clusters or groups of intensities (k), the k-means algorithm is an iterative algorithm comprising four steps:

[0132] 1. Initially determine or categorize cluster boundaries by defining a minimum and a maximum pixel intensity value for every white, gray, or black pixels into groups or k-clusters that are equally spaced in the entire intensity range.

[0133] 2. Assign each pixel to one of the white, gray or black k-clusters based on the currently set cluster boundaries.

[0134] 3. Calculate a mean intensity for each pixel intensity k-cluster or group based on the current assignment of pixels into the different k-clusters. The calculated mean intensity is defined as a cluster center. Thereafter, new cluster boundaries are determined as mid points between cluster centers.

[0135] 4. Determine if the cluster boundaries significantly change locations from their previous values. Should the cluster boundaries change significantly from their previous values, iterate back to step **2**, until the cluster centers do not change significantly between iterations. Visually, the clustering process is manifest by the segmented image and repeated iterations continue until the segmented image does not change between the iterations. The pixels in the cluster having the lowest intensity value—the darkest cluster—are defined as pixels associated with amniotic fluid. For the 2D algorithm, each image is clustered independently of the neighboring images. For the 3D algorithm, the entire volume is clustered together. To make this step faster, pixels are sampled at 2 or any multiple sampling rate factors before determining the cluster boundaries. The cluster boundaries determined from the down-sampled data are then applied to the entire data.

[0136] **FIG. 8C** depicts the sub-algorithms of Edge-Based Segmentation (step **438** in **FIG. 7**) and uses a sequence of four sub-algorithms. The sequence includes a spatial gradients **526** algorithm, a hysteresis threshold **530** algorithm, a Region-of-Interest (ROI) **534** algorithm, and a matching edges filter **538** algorithm.

[0137] The spatial gradient **526** computes the x-directional and y-directional spatial gradients of the enhanced image. The Hysteresis threshold **530** algorithm detects salient edges. Once the edges are detected, the regions defined by the edges are selected by a user employing the ROI **534** algorithm to select regions-of-interest deemed relevant for analysis.

[0138] Since the enhanced image has very sharp transitions, the edge points can be easily determined by taking x- and y-derivatives using backward differences along x- and y-directions. The pixel gradient magnitude $\|\nabla I\|$ is then computed from the x- and y-derivative image in equation E5 as:

$$\|\nabla I\| = \sqrt{I^2_x + I^2_y} \quad \text{E5}$$

[0139] Where $I^2_x$=the square of x-derivative of intensity; and

[0140] $I^2_y$=the square of y-derivative of intensity along the y-axis.

[0141] Significant edge points are then determined by thresholding the gradient magnitudes using a hysteresis thresholding operation. Other thresholding methods could also be used. In hysteresis thresholding **530**, two threshold values, a lower threshold and a higher threshold, are used. First, the image is thresholded at the lower threshold value and a connected component labeling is carried out on the resulting image. Next, each connected edge component is preserved which has at least one edge pixel having a gradient magnitude greater than the upper threshold. This kind of thresholding scheme is good at retaining long connected edges that have one or more high gradient points.

[0142] In the preferred embodiment, the two thresholds are automatically estimated. The upper gradient threshold is estimated at a value such that at most 97% of the image pixels are marked as non-edges. The lower threshold is set at 50% of the value of the upper threshold. These percentages could be different in different implementations. Next, edge points that lie within a desired region-of-interest are selected **534**. This region of interest selection **534** excludes points lying at the image boundaries and points lying too close to or too far from the transceiver **10**. Finally, the matching edge filter **538** is applied to remove outlier edge points and fill in the area between the matching edge points.

[0143] The edge-matching algorithm **538** is applied to establish valid boundary edges and remove spurious edges while filling the regions between boundary edges. Edge points on an image have a directional component indicating the direction of the gradient. Pixels in scanlines crossing a boundary edge location will exhibit two gradient transitions depending on the pixel intensity directionality. Each gradient transition is given a positive or negative value depending on the pixel intensity directionality. For example, if the scanline approaches an echo reflective bright wall from a darker region, then an ascending transition is established as the pixel intensity gradient increases to a maximum value, i.e., as the transition ascends from a dark region to a bright region. The ascending transition is given a positive numerical value. Similarly, as the scanline recedes from the echo reflective wall, a descending transition is established as the pixel intensity gradient decreases to or approaches a minimum value. The descending transition is given a negative numerical value.

[0144] Valid boundary edges are those that exhibit ascending and descending pixel intensity gradients, or equivalently, exhibit paired or matched positive and negative numerical values. The valid boundary edges are retained in the image. Spurious or invalid boundary edges do not exhibit paired ascending-descending pixel intensity gradients, i.e., do not exhibit paired or matched positive and negative numerical values. The spurious boundary edges are removed from the image.

[0145] For amniotic fluid volume related applications, most edge points for amniotic fluid surround a dark, closed region, with directions pointing inwards towards the center of the region. Thus, for a convex-shaped region, the direction of a gradient for any edge point, the edge point having a gradient direction approximately opposite to the current point represents the matching edge point. Those edge points exhibiting an assigned positive and negative value are kept as valid edge points on the image because the negative value is paired with its positive value counterpart. Similarly, those edge point candidates having unmatched values, i.e., those edge point candidates not having a negative-positive value pair, are deemed not to be true or valid edge points and are discarded from the image.

[0146] The matching edge point algorithm **538** delineates edge points not lying on the boundary for removal from the desired dark regions. Thereafter, the region between any two matching edge points is filled in with non-zero pixels to establish edge-based segmentation. In a preferred embodiment of the invention, only edge points whose directions are primarily oriented co-linearly with the scanline are sought to permit the detection of matching front wall and back wall pairs.

[0147] Returning to **FIG. 7**, once Intensity-Based **422** and Edge-Based Segmentation **438** is completed, both segmentation methods use a combining step that combines the results of intensity-based segmentation **422** step and the edge-based segmentation **438** step using an AND Operator of Images **442**. The AND Operator of Images **442** is achieved by a pixel-wise Boolean AND operator **442** step to produce a segmented image by computing the pixel intersection of two images. The Boolean AND operation **442** represents the pixels as binary numbers and the corresponding assignment of an assigned intersection value as a binary number 1 or 0 by the combination of any two pixels. For example, consider any two pixels, say $pixel_A$ and $pixel_B$, which can have a 1 or 0 as assigned values. If $pixel_A$'s value is 1, and $pixel_B$'s value is 1, the assigned intersection value of $pixel_A$ and $pixel_B$ is 1. If the binary value of $pixel_A$ and $pixel_B$ are both 0, or if either $pixel_A$ or $pixel_B$ is 0, then the assigned intersection value of $pixel_A$ and $pixel_B$ is 0. The Boolean AND operation **542** takes the binary any two digital images as input, and outputs a third image with the pixel values made equivalent to the intersection of the two input images.

[0148] Upon completion of the AND Operator of Images **442** algorithm, the polish **464** algorithm of **FIG. 7** is comprised of multiple sub-algorithms. **FIG. 8D** depicts the sub-algorithms of the Polish **464** algorithm, including a Close **546** algorithm, an Open **550** algorithm, a Remove Deep Regions **554** algorithm, and a Remove Fetal Head Regions **560** algorithm.

[0149] Closing and opening algorithms are operations that process images based on the knowledge of the shape of objects contained on a black and white image, where white represents foreground regions and black represents background regions. Closing serves to remove background features on the image that are smaller than a specified size. Opening serves to remove foreground features on the image that are smaller than a specified size. The size of the features to be removed is specified as an input to these operations. The opening algorithm **550** removes unlikely amniotic fluid regions from the segmented image based on a-priori knowledge of the size and location of amniotic fluid pockets.

[0150] Referring to **FIG. 8D**, the closing **546** algorithm obtains the Apparent Amniotic Fluid Area (AAFA) or Volume (AAFV) values. The AAFA and AAFV values are "Apparent" and maximal because these values may contain region areas or region volumes of non-amniotic origin unknowingly contributing to and obscuring what otherwise would be the true amniotic fluid volume. For example, the AAFA and AAFV values contain the true amniotic volumes, and possibly as well areas or volumes due to deep tissues and undetected fetal head volumes. Thus the apparent area and volume values require correction or adjustments due to unknown contributions of deep tissue and of the fetal head in order to determine an Adjusted Amniotic Fluid Area (AdAFA) value or Volume (AdAVA) value **568**.

[0151] The AdAFA and AdAVA values obtained by the Close **546** algorithm are reduced by the morphological opening algorithm **550**. Thereafter, the AdAFA and AdAVA values are further reduced by removing areas and volumes attributable to deep regions by using the Remove Deep Regions **554** algorithm. Thereafter, the polishing algorithm **464** continues by applying a fetal head region detection algorithm **560**.

[0152] **FIG. 8E** depicts the sub-algorithms of the Remove Fetal Head Regions sub-algorithm **560**. The basic idea of the sub-algorithms of the fetal head detection algorithm **560** is that the edge points that potentially represent a fetal skull are detected. Thereafter, a circle finding algorithm to determine the best-fitting circle to these fetal skull edges is implemented. The radii of the circles that are searched are known a priori based on the fetus' gestational age. The best fitting circle whose fitting metric lies above a certain pre-specified threshold is marked as the fetal head and the region inside this circle is the fetal head region. The algorithms include a gestational Age **726** input, a determine head diameter factor **730** algorithm, a Head Edge Detection algorithm, **734**, and a Hough transform procedure **736**.

[0153] Fetal brain tissue has substantially similar ultrasound echo qualities as presented by amniotic fluid. If not detected and subtracted from amniotic fluid volumes, fetal brain tissue volumes will be measured as part of the total amniotic fluid volumes and lead to an overestimation and false diagnosis of oligo or poly-hyraminotic conditions. Thus detecting fetal head position, measuring fetal brain matter volumes, and deducting the fetal brain matter volumes from the amniotic fluid volumes to obtain a corrected amniotic fluid volume serves to establish accurately measure amniotic fluid volumes.

[0154] The gestational age input **726** begins the fetal head detection algorithm **560** and uses a head dimension table to obtain ranges of head bi-parietal diameters (BPD) to search for (e.g., 30 week gestational age corresponds to a 6 cm head diameter). The head diameter range is input to both the Head Edge Detection, **734**, and the Hough Transform, **736**., The head edge detection **734** algorithm seeks out the distinctively bright ultrasound echoes from the anterior and posterior walls of the fetal skull while the Hough Transform algorithm, **736**, finds the fetal head using circular shapes as models for the fetal head in the Cartesian image (pre-scan conversion to polar form).

[0155] Scanplanes processed by steps **522**, **538**, **530**, are input to the head edge detection step **734**. Applied as the first

step in the fetal head detection algorithm **734** is the detection of the potential head edges from among the edges found by the matching edge filter. The matching edge **538** filter outputs pairs of edge points potentially belonging to front walls or back walls. Not all of these walls correspond to fetal head locations. The edge points representing the fetal head are determined using the following heuristics:

[**0156**] (1) Looking along a one dimensional A-mode scan line, fetal head locations present a corresponding matching gradient in the opposing direction within a short distance approximately the same size as the thickness of the fetal skull. This distance is currently set to a value 1 cm.

[**0157**] (2) The front wall and the back wall locations of the fetal head are within a range of diameters corresponding to the expected diameter **730** for the gestational age **726** of the fetus. Walls that are too close or too far are not likely to be head locations.

[**0158**] (3) A majority of the pixels between the front and back wall locations of the fetal head lie within the minimum intensity cluster as defined by the output of the clustering algorithm **422**. The percentage of pixels that need to be dark is currently defined to be 80%.

[**0159**] The pixels found satisfying these features are then vertically dilated to produce a set of thick fetal head edges as the output of Head Edge Detection, **734**.

[**0160**] **FIG. 8F** depicts the sub-algorithms of the Hough transform procedure **736**. The sub-algorithms include a Polar Hough Transform **738** algorithm, a find maximum Hough value **742** algorithm **742**, and a fill circle region **746**. The Polar Hough Transform algorithm looks for fetal head structures in polar coordinate terms by converting from Cartesian coordinates using a plurality of equations. The fetal head, which appears like a circle in a 3D scan-converted Cartesian coordinate image, has a different shape in the pre-scan converted polar space. The fetal head shape is expressed in terms of polar coordinate terms explained as follows:

[**0161**] The coordinates of a circle in the Cartesian space (x,y) with center ($x_0$, $y_0$) and radius R are defined for an angle θ are derived and defined in equation E5 as:

$$x=R\cos\theta+x_0$$
$$y=R\sin\theta+y_0$$
$$\Rightarrow(x-x_0)^2+(y-y_0)^2=R^2 \quad \text{E5}$$

[**0162**] In polar space, the coordinates (r,ϕ), with respect to the center ($r_0$, $\phi_0$), are derived and defined in equation E6 as:

$$r\sin\phi=R\cos\theta+r_0\sin\phi_0$$
$$r\cos\phi=R\sin\theta+r_0\cos\phi^0$$
$$\Rightarrow(r\sin\phi-r_0\sin\phi_0)^2+(r\cos\phi-r_0\cos\phi_0)^2=R^2 \quad E6$$

[**0163**] The Hough transform **736** algorithm using equations E5 and E6 attempts to find the best-fit circle to the edges of an image. A circle in the polar space is defined by a set of three parameters, ($r_0$, $\phi_0$, R) representing the center and the radius of the circle.

[**0164**] The basic idea for the Hough transform **736** is as follows. Suppose a circle is sought having a fixed radius (say, R1) for which the best center of the circle is similarly sought. Now, every edge point on the input image lies on a potential circle whose center lays R1 pixels away from it. The set of potential centers themselves form a circle of radius R1 around each edge pixel. Now, drawing potential circles of radius R1 around each edge pixel, the point at which most circles intersect, a center of the circle that represents a best-fit circle to the given edge points is obtained. Therefore, each pixel in the Hough transform output contains a likelihood value that is simply the count of the number of circles passing through that point.

[**0165**] **FIG. 9** illustrates the Hough Transform **736** algorithm for a plurality of circles with a fixed radius in a Cartesian coordinate system. A portion of the plurality of circles is represented by a first circle **804***a*, a second circle **804***b*, and a third circle **804***c*. A plurality of edge pixels are represented as gray squares and an edge pixel **808** is shown. A circle is drawn around each edge pixel to distinguish a center location **812** of a best-fit circle **816** passing through each edge pixel point; the point of the center location through which most such circles pass (shown by a gray star **812**) is the center of the best-fit circle **816** presented as a thick dark line. The circumference of the best fit circle **816** passes substantially through is central portion of each edge pixel, represented as a series of squares substantially equivalent to the edge pixel **808**.

[**0166**] This search for best fitting circles can be easily extended to circles with varying radii by adding one more degree of freedom—however, a discrete set of radii around the mean radii for a given gestational age makes the search significantly faster, as it is not necessary to search all possible radii.

[**0167**] The next step in the head detection algorithm is selecting or rejecting best-fit circles based on its likelihood, in the find maximum Hough Value **742** algorithm. The greater the number of circles passing through a given point in the Hough-space, the more likely it is to be the center of a best-fit circle. A 2D metric as a maximum Hough value **742** of the Hough transform **736** output is defined for every image in a dataset. The 3D metric is defined as the maximum of the 2D metrics for the entire 3D dataset. A fetal head is selected on an image depending on whether its 3D metric value exceeds a preset 3D threshold and also whether the 2D metric exceeds a preset 2D threshold. The 3D threshold is currently set at 7 and the 2D threshold is currently set at 5. These thresholds have been determined by extensive training on images where the fetal head was known to be present or absent.

[**0168**] Thereafter, the fetal head detection algorithm concludes with a fill circle region **746** that incorporates pixels to the image within the detected circle. The fill circle region **746** algorithm fills the inside of the best fitting polar circle. Accordingly, the fill circle region **746** algorithm encloses and defines the area of the fetal brain tissue, permitting the area and volume to be calculated and deducted via algorithm **554** from the apparent amniotic fluid area and volume (AAFA or AAFV) to obtain a computation of the corrected amniotic fluid area or volume via algorithm **484**.

[**0169**] **FIG. 10** shows the results of sequentially applying the algorithm steps of **FIGS. 7 and 8**A-D on an unprocessed sample image **820** presented within the confines of a scan-plane substantially equivalent to the scanplane **210**. The results of applying the heat filter **514** and shock filter **518** in enhancing the unprocessed sample is shown in enhanced

image **840**. The result of intensity-based segmentation algorithms **522** is shown in image **850**. The results of edge-based segmentation **438** algorithm using sub-algorithms **526**, **530**, **534** and **538** of the enhanced image **840** is shown in segmented image **858**. The result of the combination **442** utilizing the Boolean AND images **442** algorithm is shown in image **862** where white represents the amniotic fluid area. The result of applying the polishing **464** algorithm employing algorithms **542**, **546**, **550**, **554**, **560**, and **564** is shown in image **864**, which depicts the amniotic fluid area overlaid on the unprocessed sample image **810**.

[**0170**] **FIG. 11** depicts a series of images showing the results of the above method to automatically detect, locate, and measure the area and volume of a fetal head using the algorithms outlined in **FIGS. 7 and 8**A-F. Beginning with an input image in polar coordinate form **920**, the fetal head image is marked by distinctive bright echoes from the anterior and posterior walls of the fetal skull and a circular shape of the fetal head in the Cartesian image. The fetal head detection algorithm **734** operates on the polar coordinate data (i.e., pre-scan version, not yet converted to Cartesian coordinates).

[**0171**] An example output of applying the head edge detection **734** algorithm to detect potential head edges is shown in image **930**. Occupying the space between the anterior and posterior walls are dilated black pixels **932** (stacks or short lines of black pixels representing thick edges). An example of the polar Hough transform **738** for one actual data sample for a specific radius is shown in polar coordinate image **940**.

[**0172**] An example of the best-fit circle on real data polar data is shown in polar coordinate image **950** that has undergone the find maximum Hough value step **742**. The polar coordinate image **950** is scan-converted to a Cartesian data in image **960** where the effects of finding maximum Hough value **742** algorithm are seen in Cartesian format.

[**0173**] **FIG. 12** presents a 4-panel series of sonographer amniotic fluid pocket outlines compared to the algorithm's output in a scanplane equivalent to scanplane **210**. The top two panels depict the sonographer's outlines of amniotic fluid pockets obtained by manual interactions with the display while the bottom two panels show the resulting amniotic fluid boundaries obtained from the instant invention's automatic application of 2D algorithms, 3D algorithms, combination heat and shock filter algorithms, and segmentation algorithms.

[**0174**] After the contours on all the images have been delineated, the volume of the segmented structure is computed. Two specific techniques for doing so are disclosed in detail in U.S. Pat. No. 5,235,985 to McMorrow et al, herein incorporated by reference. This patent provides detailed explanations for non-invasively transmitting, receiving and processing ultrasound for calculating volumes of anatomical structures.

## Multiple Image Cone Acquisition and Image Processing Procedures

[**0175**] In some embodiments, multiple cones of data acquired at multiple anatomical sampling sites may be advantageous. For example, in some instances, the pregnant uterus may be too large to completely fit in one cone of data sampled from a single measurement or anatomical site of the patient (patient location). That is, the transceiver **10** is moved to different anatomical locations of the patient to obtain different 3D views of the uterus from each measurement or transceiver location.

[**0176**] Obtaining multiple 3D views may be especially needed during the third trimester of pregnancy, or when twins or triplets are involved. In such cases, multiple data cones can be sampled from different anatomical sites at known intervals and then combined into a composite image mosaic to present a large uterus in one, continuous image. In order to make a composite image mosaic that is anatomically accurate without duplicating the anatomical regions mutually viewed by adjacent data cones, ordinarily it is advantageous to obtain images from adjacent data cones and then register and subsequently fuse them together. In a preferred embodiment, to acquire and process multiple 3D data sets or images cones, at least two 3D image cones are generally preferred, with one image cone defined as fixed, and the other image cone defined as moving.

[**0177**] The 3D image cones obtained from each anatomical site may be in the form of 3D arrays of 2D scanplanes, similar to the 3D array **240**. Furthermore, the 3D image cone may be in the form of a wedge or a translational array of 2D scanplanes. Alternatively, the 3D image cone obtained from each anatomical site may be a 3D scancone of 3D-distributed scanlines, similar to the scancone **300**.

[**0178**] The term "registration" with reference to digital images means the determination of a geometrical transformation or mapping that aligns viewpoint pixels or voxels from one data cone sample of the object (in this embodiment, the uterus) with viewpoint pixels or voxels from another data cone sampled at a different location from the object. That is, registration involves mathematically determining and converting the coordinates of common regions of an object from one viewpoint to the coordinates of another viewpoint. After registration of at least two data cones to a common coordinate system, the registered data cone images are then fused together by combining the two registered data images by producing a reoriented version from the view of one of the registered data cones. That is, for example, a second data cone's view is merged into a first data cone's view by translating and rotating the pixels of the second data cone's pixels that are common with the pixels of the first data cone. Knowing how much to translate and rotate the second data cone's common pixels or voxels allows the pixels or voxels in common between both data cones to be superimposed into approximately the same x, y, z, spatial coordinates so as to accurately portray the object being imaged. The more precise and accurate the pixel or voxel rotation and translation, the more precise and accurate is the common pixel or voxel superimposition or overlap between adjacent image cones. The precise and accurate overlap between the images assures the construction of an anatomically correct composite image mosaic substantially devoid of duplicated anatomical regions.

[**0179**] To obtain the precise and accurate overlap of common pixels or voxels between the adjacent data cones, it is advantageous to utilize a geometrical transformation that substantially preserves most or all distances regarding line straightness, surface planarity, and angles between the lines as defined by the image pixels or voxels. That is, the

preferred geometrical transformation that fosters obtaining an anatomically accurate mosaic image is a rigid transformation that doesn't permit the distortion or deforming of the geometrical parameters or coordinates between the pixels or voxels common to both image cones.

[0180] The preferred rigid transformation first converts the polar coordinate scanplanes from adjacent image cones into in x, y, z Cartesian axes. After converting the scanplanes into the Cartesian system, a rigid transformation, T, is determined from the scanplanes of adjacent image cones having pixels in common. The transformation T is a combination of a three-dimensional translation vector expressed in Cartesian as $t=(T_x, T_y, T_z)$, and a three-dimensional rotation R matrix expressed as a function of Euler angles $\theta_x$, $\theta_y$, $\theta_z$ around the x, y, and z axes. The transformation represents a shift and rotation conversion factor that aligns and overlaps common pixels from the scanplanes of the adjacent image cones.

[0181] In the preferred embodiment of the present invention, the common pixels used for the purposes of establishing registration of three-dimensional images are the boundaries of the amniotic fluid regions as determined by the amniotic fluid segmentation algorithm described above.

[0182] Several different protocols may be used to collect and process multiple cones of data from more than one measurement site are described in **FIGS. 13-14**.

[0183] **FIG. 13** illustrates a 4-quadrant supine procedure to acquire multiple image cones around the center point of uterine quadrants of a patient in a supine procedure. Here the patient lies supine (on her back) displacing most or all of the amniotic fluid towards the top. The uterus is divided into 4 quadrants defined by the umbilicus (the navel) and the linea-nigra (the vertical center line of the abdomen) and a single 3D scan is acquired at each quadrant. The 4-quadrant supine protocol acquires four different 3D scans in a two dimensional grid, each corner of the grid being a quadrant midpoint. Four cones of data are acquired by the transceiver **10** along the midpoints of quadrant **1**, quadrant **2**, quadrant **3**, and quadrant **4**. Thus, one 3D data cone per uterine quadrant midpoint is acquired such that each quadrant midpoint is mutually substantially equally spaced from each other in a four-corner grid array.

[0184] **FIG. 14** illustrates a multiple lateral line procedure to acquire multiple image cones in a linear array. Here the patent lies laterally (on her side), displacing most or all of the amniotic fluid towards the top. Four 3D images cones of data are acquired along a line of substantially equally space intervals. As illustrated, the transceiver **10** moves along the lateral line at position **1**, position **2**, position **3**, and position **4**. As illustrated in **FIG. 14**, the inter-position distance or interval is approximately 6 cm.

[0185] The preferred embodiment for making a composite image mosaic involves obtaining four multiple image cones where the transceiver **10** is placed at four measurement sites over the patient in a supine or lateral position such that at least a portion of the uterus is ultrasonically viewable at each measurement site. The first measurement site is originally defined as fixed, and the second site is defined as moving and placed at a first known inter-site distance relative to the first site. The second site images are registered and fused to the first site images After fusing the second site images to the first site images, the third measurement site is defined as moving and placed at a second known inter-site distance relative to the fused second site now defined as fixed. The third site images are registered and fused to the second site images Similarly, after fusing the third site images to the second site images, the fourth measurement site is defined as moving and placed at a third known inter-site distance relative to the fused third site now defined as fixed. The fourth site images are registered and fused to the third site images

[0186] The four measurement sites may be along a line or in an array. The array may include rectangles, squares, diamond patterns, or other shapes. Preferably, the patient is positioned such that the baby moves downward with gravity in the uterus and displaces the amniotic fluid upwards toward the measuring positions of the transceiver **10**.

[0187] The interval or distance between each measurement site is approximately equal, or may be unequal. For example in the lateral protocol, the second site is spaced approximately 6 cm from the first site, the third site is spaced approximately 6 cm from the second site, and the fourth site is spaced approximately 6 cm from the third site. The spacing for unequal intervals could be, for example, the second site is spaced approximately 4 cm from the first site, the third site is spaced approximately 8 cm from the second site, and the third is spaced approximately 6 cm from the third site. The interval distance between measurement sites may be varied as long as there are mutually viewable regions of portions of the uterus between adjacent measurement sites.

[0188] For uteruses not as large as requiring four measurement sites, two and three measurement sites may be sufficient for making a composite 3D image mosaic. For three measurement sites, a triangular array is possible, with equal or unequal intervals. Furthermore, is the case when the second and third measurement sites have mutually viewable regions from the first measurement site, the second interval may be measured from the first measurement site instead of measuring from the second measurement site.

[0189] For very large uteruses not fully captured by four measurement or anatomical sites, greater than four measurement sites may be used to make a composite 3D image mosaic provided that each measurement site is ultrasonically viewable for at least a portion of the uterus. For five measurement sites, a pentagon array is possible, with equal or unequal intervals. Similarly, for six measurement sites, a hexagon array is possible, with equal or unequal intervals between each measurement site. Other polygonal arrays are possible with increasing numbers of measurement sites.

[0190] The geometrical relationship between each image cone must be ascertained so that overlapping regions can be identified between any two image cones to permit the combining of adjacent neighboring cones so that a single 3D mosaic composite image is produced from the 4-quadrant or in-line laterally acquired images.

[0191] The translational and rotational adjustments of each moving cone to conform with the voxels common to the stationary image cone is guided by an inputted initial transform that has the expected translational and rotational values. The distance separating the transceiver **10** between image cone acquisitions predicts the expected translational

and rotational values. For example, as shown in **FIG. 14**, if 6 cm separates the image cones, then the expected translational and rotational values are proportionally estimated. For example, the ($T_x$, $T_y$, $T_z$) and ($\theta_x$, $\theta_y$, $\theta_z$) Cartesian and Euler angle terms fixed images p voxel values are defined respectively as (6 cm, 0 cm, 0 cm) and (0 deg, 0 deg, 0 deg).

[**0192**] **FIG. 15** is a block diagram algorithm overview of the registration and correcting algorithms used in processing multiple image cone data sets. The algorithm overview **1000** shows how the entire amniotic fluid volume measurement process occurs from the multiply acquired image cones. First, each of the input cones **1004** is segmented **1008** to detect all amniotic fluid regions. The segmentation **1008** step is substantially similar to steps **418-480** of **FIG. 7**. Next, these segmented regions are used to align (register) the different cones into one common coordinate system using a Rigid Registration **1012** algorithm. Next, the registered datasets from each image cone are fused with each other using a Fuse Data **1016** algorithm to produce a composite 3D mosaic image. Thereafter, the total amniotic fluid volume is computed **1020** from the fused or composite 3D mosaic image.

[**0193**] **FIG. 16** is a block diagram of the steps of the rigid registration algorithm **1012**. The rigid algorithm **1012** is a 3D image registration algorithm and is a modification of the Iterated Closest Point (ICP) algorithm published by P J Besl and N D McKay, in "A Method for Registration of 3-D Shapes,"*IEEE Trans. Pattern Analysis & Machine Intelligence, vol.* 14, no. **2**, February 1992, pp. 239-256. The steps of the rigid registration algorithm **1012** serves to correct for overlap between adjacent 3D scan cones acquired in either the 4-quadrant supine grid procedure or lateral line multi data cone acquisition procedures. The rigid algorithm **1012** first processes the fixed image **1104** in polar coordinate terms to Cartesian coordinate terms using the 3D Scan Convert **1108** algorithm. Separately, the moving image **1124** is also converted to Cartesian coordinates using the 3D Scan Convert **1128** algorithm. Next, the edges of the amniotic fluid regions on the fixed and moving images are determined and converted into point sets p and q respectively by a 3D edge detection process **1112** and **1132**. Also, the fixed image point set, p, undergoes a 3D distance transform process **1116** which maps every voxel in a 3D image to a number representing the distance to the closest edge point in p. Pre-computing this distance transform makes subsequent distance calculations and closest point determinations very efficient.

[**0194**] Next, the known initial transform **1136**, for example, (6, 0, 0) for the Cartesian $T_x$, $T_y$, $T_z$ terms and (0, 0, 0) for the $\theta_x$, $\theta_y$, $\theta_z$ Euler angle terms for an inter-transceiver interval of 6 cm, is subsequently applied to the moving image by the Apply Transform **1140** step. This transformed image is then compared to the fixed image to examine for the quantitative occurrence of overlapping voxels. If the overlap is less than 20%, there are not enough common voxels available for registration and the initial transform is considered sufficient for fusing at step **1016**.

[**0195**] If the overlapping voxel sets by the initial transform exceed 20% of the fixed image p voxel sets, the q-voxels of the initial transform are subjected to an iterative sequence of rigid registration.

[**0196**] A transformation T serves to register a first voxel point set p from the first image cone by merging or overlapping a second voxel point set q from a second image cone that is common to p of the first image cone. A point in the first voxel point set p may be defined as $p_i=(x_i, y_i, z_i)$ and a point in the second voxel point set q may similarly be defined as $q_j=(x_j,y_j, z_j)$, If the first image cone is considered to be a fixed landmark, then the T factor is applied to align (translate and rotate) the moving voxel point set q onto the fixed voxel point set p.

[**0197**] The precision of T is often affected by noise in the images that accordingly affects the precision of t and R, and so the variability of each voxel point set will in turn affect the overall variability of each matrix equation set for each point. The composite variability between the fixed voxel point set p and a corresponding moving voxel point set q is defined to have a cross-covariance matrix Cpq, more fully described in equation E8 as:

$$C_{pq} = \frac{1}{n} \sum_{i=1 \ldots n} (p_i - \bar{p})(q_i - \bar{q})^T \qquad E8$$

[**0198**] where, n is the number of points in each point set and $\bar{p}$ and $\bar{q}$ are the central points in the two voxel point sets. How strong the correlation is between two sets data is determined by statistically analyzing the cross-covariance $C_{pq}$. The preferred embodiment uses a statistical process known as the Single Value Decomposition (SVD) originally developed by Eckart and Young (G. Eckart and G. Young, 1936, *The Approximation of One Matrix by Another of Lower Rank*, Pychometrika 1, 211-218). When numerical data is organized into matrix form, the SVD is applied to the matrix, and the resulting SVD values are determined to solve for the best fitting rotation transform R to be applied to the moving voxel point set q to align with the fixed voxel point set p to acquire optimum overlapping accuracy of the pixel or voxels common to the fixed and moving images.

[**0199**] Equation E9 gives the SVD value of the cross-covariance $C_{pq}$:

$$C_{pq}=UDV^t \qquad E9$$

[**0200**] where D is a 3×3 diagonal matrix and U and V are orthogonal 3×3 matrices

[**0201**] Equation E10 further defines the rotational R description of the transformation T in terms of U and V orthogonal 3×3 matrices as:

$$R=UV^T \qquad E10$$

[**0202**] Equation E11 further defines the translation transform t description of the transformation T in terms of $\bar{p}$, $\bar{q}$ and R as:

$$t=\bar{p}-R\bar{q} \qquad E11$$

[**0203**] Equations E8 through E11 present a method to determine the rigid transformation between two point sets p and q—this process corresponds to step **1152** in **FIG. 17**.

[**0204**] The steps of the registration algorithm are applied iteratively until convergence. The iterative sequence includes a Find Closest Points on Fixed Image **1148** step, a Determine New Transform **1152** step, a Calculate Distances **1156** step, and Converged decision **1160** step.

[0205] In the Find Closest Points on Fixed Image **1148** step, corresponding q points are found for each point in the fixed set p. Correspondence is defined by determining the closest edge point on q to the edge point of p. The distance transform image helps locate these closest points. Once p and closest −q pixels are identified, the Determine New Transform **1152** step calculates the rotation R via SVD analysis using equations E8-E10 and translation transform t via equation E11. If, at decision step **1160**, the change in the average closest point distance between two iterations is less than 5%, then the predicted-q pixel candidates are considered converged and suitable for receiving the transforms R and t to rigidly register the moving image Transform **1136** onto the common voxels p of the 3D Scan Converted **1108** image. At this point, the rigid registration process is complete as closest proximity between voxel or pixel sets has occurred between the fixed and moving images, and the process continues with fusion at step **1016**.

[0206] If, however, there is >5% change between the predicted-q pixels and p pixels, another iteration cycle is applied via the Apply Transform **1140** to the Find Closest Points on Fixed Image **1148** step, and is cycled through the converged **1160** decision block. Usually in 3 cycles, though as many as 20 iterative cycles, are engaged until is the transformation T is considered converged.

[0207] A representative example for the application of the preferred embodiment for the registration and fusion of a moving image onto a fixed image is shown in **FIGS. 17A-17C**.

[0208] **FIG. 17A** is a first measurement view of a fixed scanplane **1200**A from a **3**D data set measurement taken at a first site. A first pixel set p consistent for the dark pixels of AFV is shown in a region **1204**A. The region **1204**A has approximate x-y coordinates of **(150, 120)** that is closest to dark edge.

[0209] **FIG. 17B** is a second measurement view of a moving scanplane **1200**B from a 3D data set measurement taken at a second site. A second pixel set q consistent for the dark pixels of AFV is shown in a region **1204**B. The region **1204**B has approximate x-y coordinates of **(50, 125)** that is closest to dark edge.

[0210] **FIG. 17C** is a composite image **1200**C of the first (fixed) **1200**A and second (moving) **1200**B images in which common pixels **1204**B at approximate coordinates (50,125) is aligned or overlapped with the voxels **1204**A at approximate coordinates (150, 120). That is, the region **1204**B pixel set q is linearly and rotational transformed consistent with the closest edge selection methodology as shown in **FIGS. 13A and 13B** from employing the 3D Edge Detection **1112** step. The composite image **1200**C is a mosaic image from scanplanes having approximately the same ϕ and rotation θ angles.

[0211] The registration and fusing of common pixel sets p and q from scanplanes having approximately the same ϕ and rotation θ angles can be repeated for other scanplanes in each 3D data set taken at the first (fixed) and second(moving) anatomical sites. For example, if the composite image **1200**C above was for scanplane **#1**, then the process may be repeated for the remaining scanplanes #2-24 or #2-48 or greater as needed to capture a completed uterine mosaic image. Thus an array similar to the 3D array **240** from **FIG. 5B** is assembled, except this time the scanplane array is made of composite images, each composited image belonging to a scanplane having approximately the same ϕ and rotation θ angles.

[0212] If a third and a fourth 3D data sets are taken, the respective registration, fusing, and assembling into scanplane arrays of composited images is undertaken with the same procedures. In this case, the scanplane composite array similar to the 3D array **240** is composed of a greater mosaic number of registered and fused scanplane images.

[0213] A representative example the fusing of two moving images onto a fixed image is shown in **FIGS. 18A-18D**.

[0214] **FIG. 18A** is a first view of a fixed scanplane **1220**A. Region **1224**A is identified asp voxels approximately at the coordinates (150, 70).

[0215] **FIG. 18B** is a second view of a first moving scanplane **1220**B having some q voxels **1224**B at x-y coordinates (300, 100) common with the first measurements p voxels at x-y coordinates (150, 70). Another set of voxels **1234**A is shown roughly near the intersection of x-y coordinates (200, 125). As the transceiver **10** was moved only translationally, The scanplane **1220**B from the second site has approximately the same tilt ϕ and rotation θ angles of the fixed scanplane **1220**A taken from the first lateral in-line site.

[0216] **FIG. 18C** is a third view of a moving scanplane **1220**C. A region **1234**B is identified as q voxels approximately at the x-y coordinates (250, 100) that are common with the second views q voxels **1234**A. The scanplane **1220***c* from the third lateral in-line site has approximately the same tilt **0** and rotation **0** angles of the fixed scanplane **1220**A taken from the first lateral in-line site and the first moving scanplane **1220**B taken from the second lateral in-line site.

[0217] **FIG. 18D** is a composite mosaic image **1220**D of the first (fixed) **1220**A image, the second (moving) **1220**B image, and the third (moving) **1220**C image representing the sequential alignment and fusing of q voxel sets **1224**B to **1224**A, and **1234**B with **1234**A.

[0218] A fourth image similarly could be made to bring about a 4-image mosaic from scanplanes from a fourth 3D data set acquired from the transceiver **10** taking measurements at a fourth anatomical site where the fourth 3D data set is acquired with approximately the same tilt ϕ and rotation θ angles.

[0219] The transceiver **10** is moved to different anatomical sites to collect 3D data sets by hand placement by an operator. Such hand placement could create the acquiring of 3D data sets under conditions in which the tilt ϕ and rotation θ angles are not approximately equal, but differ enough to cause some measurement error requiring correction to use the rigid registration **1012** algorithm. In the event where the 3D data sets between anatomical sites, either between a moving supine site in relation to its beginning fixed site, or between a moving lateral site with its beginning fixed site, cannot be acquired with the tilt ϕ and rotation θ angles being approximately the same, then the built-in accelerometer measures the changes in tilt ϕ and rotation θ angles and compensates accordingly so that acquired moving images are presented if though they were acquired under approximately equal tilt ϕ and rotation θ angle conditions.

[0220] **FIG. 19** illustrates a 6-section supine procedure to acquire multiple image cones around the center point of a uterus of a patient in a supine position. Each of the 6 segments are scanned in the order indicated, starting with segment **1** on the lower right side of the patient. The display on the scanner **10** is configured to indicate how many segments have been scanned, so that the display shows "0 of 6,""1 of 6," . . . "6 of 6." The scans are positioned such that the lateral distances between each scanning position (except between positions **3** and **4**) are approximately about 8 cm. Alternate intervals are used in alternate embodiments.

[0221] To repeat the scan, the top button of the scanner **10** is repetitively depressed, so that it returns the scan to "0 of 6," to permit a user to repeat all six scans again. Finally, the scanner **10** is returned to the cradle to upload the raw ultrasound data to computer, intranet, or Internet as depicted in **FIGS. 2C, 3**, and **4** for algorithmic processing, as will be described in detail below. Within a time period, preferably predetermined, a result is generated that includes an estimate of the amniotic fluid volume.

[0222] As with the quadrant and the four in-line scancone measuring methods described earlier, the six-segment procedure ensures that the measurement process detects all amniotic fluid regions. The transceiver **10** projects outgoing ultrasound signals, in this case into the uterine region of a patient, at six anatomical locations, and receives incoming echoes reflected back from the regions of interest to the transceiver **10** positioned at a given anatomical location. An array of scanplane images is obtained for each anatomical location based upon the incoming echo signals. Image enhanced and segmented regions for the scanplane images are determined, preferably for each scanplane array, which may be a rotational, wedge, or translationally configured scanplane array. The segmented regions are used to align or register the different scancones into one common coordinate system. Thereafter, the registered datasets are merged with each other so that the total amniotic fluid volume is computed from the resulting fused image.

[0223] **FIG. 20** is a block diagrammatic overview of an algorithm for the registration and correction processing of the 6-section multiple image cone data sets depicted in **FIG. 19**. A six-section algorithm overview **1000**A includes many of the same blocks of algorithm overview **1000** depicted in **FIG. 15**. However, the segmentation registration procedures are modified for the 6-section multiple image cones. In the algorithm overview **1000**A, the sub-processes include the InputCones block **1004**, an Image Enhancement and Segmentation block **1010**, a RigidRegistration block **1014**, the FuseData block **1016**, and the CalculateVolume block **1020**. Generally, the Image Enhanced and Segmentation block **1010** reduces the effects of "noise", which may include speckle noise, in the data while preserving the salient edges on the image. The enhanced images are then segmented by an edge-based and intensity-based method, and the results of each segmentation method are then subsequently combined. The results of the combined segmentation method are then cleaned up to fill gaps and to remove outliers. The area and/or the volume of the segmented regions are then computed.

[0224] **FIG. 21** is a more detailed view of the Image Enhancement and Segmentation block **1010** of **FIG. 20**. Very similar to the algorithm processes of Image Enhancement **418**, Intensity-based segmentation **422**, and Edge-based segmentation **438** explained for **FIG. 7**, the enhancement-segmentation block **1010** begins with an input data block **1010A2**, wherein the signals of pixel image data are subjected to a blurring and speckle removal process followed by a sharpening or de-blurring process. The combination of blurring and speckle removal followed by sharpening or de-blurring enhances the appearance of the pixel-based input image.

[0225] The blurring and de-blurring is achieved by a combination of heat and shock filters. The inputed pixel related data from process **1010A2** is first subjected to a heat filter process block **1010A4**. The heat filter block **1010A4** is a Laplacian-based filtering process and results in reduction of the speckle noise and smooths or otherwise blurs the edges in the image. The heat filter block **1010A4** is modified via a user-determined stored data block **1010A6** wherein the number of heat filter iterations and step sizes are defined by the user and are applied to the inputed data **1010A2** in the heat filter process block **1010A4**. The effect of heat iteration number in progressively blurring and removing speckle from an original image as the number of iteration cycles is increased is shown in **FIG. 23**. Once the pixel image data has been heat filter processed, the pixel image data is further processed by a shock filter block **1010A8**. The shock filter block **1010A8** is subjected to a user-determined stored data block **1010A10** wherein the number shock filter iterations, step sizes, and gradient threshold are specified by the user. The foregoing values are then applied to heat filtered pixel data in the shock filter block **1010A8**. The effect of shock iteration number, step sizes, and gradient thresholds in reducing the blurring is seen in signal plots (a) and (b) of **FIG. 24**. Thereafter, a heat and shock-filtered pixel data is parallel processed in two algorithm pathways, as defined by blocks **1010B2-6** (Intensity-Based Segmentation Group) and blocks **1010C2-4** (Edge-Based Segmentation Group).

[0226] The Intensity-based Segmentation utilizes the observation that amniotic fluid is usually darker than the rest of the image. Pixels associated with fluids are classified based upon a threshold intensity level. Thus pixels below this intensity threshold level are interpreted as fluid, and pixels above this intensity threshold are interpreted as solid or non-fluid tissues. However, pixel values within a dataset can vary widely, so a means to automatically determine a threshold level within a given dataset is required in order to distinguish between fluid and non-fluid pixels. The intensity-based segmentation is divided into three steps. A first step includes estimating the fetal body and shadow regions, a second step includes determining an automatic thresholding for the fluid region after removing the body region, and a third step includes removing the shadow and fetal body regions from the potential fluid regions. In alternate embodiments, different sequences of these steps, and more or fewer steps are utilized.

[0227] The Intensity-Based Segmentation Group includes a fetal body region block **1010B2**, wherein an estimate of the fetal shadow and body regions is obtained. Generally, the fetal body regions in ultrasound images appear bright and are relatively easily detected. Commonly, anterior bright regions typically correspond with the dome reverberation of the transceiver **10**, and the darker appearing uterus is discernable against the bright pixel regions formed by the more echogenic fetal body that commonly appears posterior to the

amniotic fluid region. In fetal body region block **1010**B2, the fetal body and shadow is found in scanlines that extend between the bright dome reverberation region and the posterior bright-appearing fetal body. A magnitude of the estimate of fetal and body region is then modified by a user-determined input parameter stored in a body threshold data block **1010**B4, and a pixel value is chosen by the user. For example, a pixel value of 40 may be selected by the user. An example of the image obtained from blocks **1010**B2-4 is panel (c) of **FIG. 25**. Once the fetal body regions and the shadow has been estimated, an automatic region threshold block **1010**B6 is applied to this estimate to determine which pixels are fluid related and which pixels are non-fluid related. The automatic region threshold block **1010**B6 uses a version of the Otsu algorithm (R M Haralick and L G Shaprio, Computer and Robot Vision, vol. 1, Addison Wesley 1992, page 11, incorporated by reference). Briefly, and in general terms, the Otsu algorithm determines a threshold value from an assumed bimodal pixel value histogram that generally corresponds to fluid and some soft tissue (non-fluid) such as placental or other fetal or maternal soft tissue. All pixel values less than the threshold value as determined by the Otsu algorithm are designated as potential fluid pixels. Using the Otsu algorithm determined threshold value, the first pathway is completed by a removing body regions above this threshold value in block **1010**B8 so that the amniotic fluid regions are isolated. An example of the effect of the Intensity-based segmentation group is shown in panel (d) of **FIG. 25**. The isolated amniotic fluid region image thus obtained from the intensity-based segmentation process is then processed for subsequent combination with the end result of the second edge-based segmentation method.

[**0228**] Referring now to the second pathway or the Edge-Based Segmentation Group, the procedural blocks find pixel points on an image having high spatial gradient magnitudes. The edge-based segmentation process begins processing the shock filtered **1010**A8 pixel data via a spatial gradients block **1010**C2 in which the gradient magnitude of a given pixel neighborhood within the image is determined. The gradient magnitude is determined by the taking the X and Y derivatives using the difference kernels shown in **FIG. 26**.

[**0229**] The gradient magnitude of the image is given by Equation E7:

$$\|\nabla I\| = \sqrt{I_x^2 + I_y^2}$$
$$I_x = I * K_x$$
$$I_y = I * K_y \qquad E7$$

[**0230**] where * is the convolution operator.

[**0231**] Once the gradient magnitude is determined, pixel edge points are determined by a hysteresis threshold of gradients process block **1010**C4. In block **1010**C4, a lower and upper threshold value is selected. The image is then thresholded using the lower value and a connected component labeling is performed on the resulting image. The pixel value of each connected component is measured to determine which pixel edge points have gradient magnitude pixel values equal to or greater than the upper threshold value. Those pixel edge points having gradient magnitude pixel values equal to or exceeding the upper threshold are retained. This retention of pixels having strong gradient values serves to retain selected long connected edges which have one or more high gradient points.

[**0232**] Thereafter, the image is thresholded using the upper value, and a connected component labeling is carried out on the resulting image. The hysteresis threshold **1010**C4 is modified by a user-determined edge threshold block **1010**C6. An example of an application of the second pathway will be shown in panels (b) for the spatial gradients block **1010**C2 and (c) for the threshold of gradients process block **1010**C4 of **FIG. 27**. Another example of application of the edge detection block group for blocks **1010**C2 and **1010**C4 can also be seen in panel (e) of **FIG. 25**.

[**0233**] Referring again to **FIG. 21**, the first and second pathways are merged at a combined region and edges process block **1010**D2. The combining process avoids erroneous segmentation arising from either the intensity-based or edge-based segmentation processes. The goal of the combining process is to ensure that good edges are reliably identified so that fluid regions are bounded by strong edges. Intensity-based segmentation may underestimate fluid volume, so that the boundaries need to be corrected using the edge-based segmentation information. In block **1010**D2, the beginning and end of each scanline within the segmented region is determined by searching for edge pixels on each scanline. If no edge pixels are found in the search region, the segmentation on that scanline is removed. If edge pixels are found, then the region boundary locations are moved to the location of these edge pixels. Panel (f) of **FIG. 25** illustrates the effects of the combining block **1010**D2.

[**0234**] The segmentation resulting from the combination of region and edge information occasionally includes extraneous regions or even holes. A cleanup stage helps ensure consistency of segmented regions in a single scanplane and between scanplanes. The cleanup stage uses morphological operators (such as erosion, dilation, opening, closing) using the Markov Random Fields (MRFs) as disclosed in Forbes et al. (Florence Forbes and Adrian E. Raftery, "Bayesian morphology: Fast Unsupervised Bayesian Image Analysis," Journal of the American Statistical Association, June 1999, herein incorporated by reference). The combined segmentation images receive the MRFs by being subjected to an In-plane Closing and Opening process block **1010**D4. The In-plane opening-closing block **1010**D4 block is a morphological operator wherein pixel regions are opened to remove pixel outliers from the segmented region, or that fills in or "closes" gaps and holes in the segmented region within a given scanplane. Block **1010**D4 uses a one-dimensional structuring element extending through five scanlines. The closing-opening block is affected by a user-determined width, height, and depth parameter block **1010**D6. Thereafter, an Out-of-plane Closing and Opening processing block **1010**D8 is applied. The block **1010**D8 applies a set of out-of-plane morphological closings and openings using a one-dimensional structuring element extending through three scanlines. Pixel inconsistencies are accordingly removed between the scanplanes. Panel (g) of **FIG. 25** illustrates the effects of the blocks **1010**D4-8.

[**0235**] **FIG. 22** is an expansion of the RigidRegistration block **1014** of **FIG. 20**. Similar in purpose and general operation using the previously described ICP algorithm as used in the RigidRegistration block **1012** of **FIG. 16**, the block **1014** begins with parallel inputs of a fixed Image **1014**A, a Moving Image **1014**B, and an Initial Transform input **1014**B10.

[0236] The steps of the rigid registration algorithm **1014** correct any overlaps between adjacent 3D scan cones acquired in the 6-section supine grid procedure. The rigid algorithm **1014** first converts the fixed image **1104**A2 from polar coordinate terms to Cartesian coordinate terms using the 3D Scan Convert **1014**A4 algorithm. Separately, the moving image **1014**B2 is also converted to Cartesian coordinates using the 3D Scan Convert **1014**B4 algorithm. Next, the edges of the amniotic fluid regions on the fixed and moving images are determined and converted into point sets p and q, respectively by a 3D edge detection process **1014**A6 and **1014**B6. Also, the fixed image point set, p, undergoes a 3D distance transform process **1014**B8 which maps every voxel in a 3D image to a number representing the distance to the closest edge point in p. Pre-computing this distance transform makes subsequent distance calculations and closest point determinations very efficient.

[0237] Next, the known initial transform **1014**B10, for example, (6, 0, 0) for the Cartesian $T_x$, $T_y$, $T_z$ terms and (0, 0, 0) for the $\theta_x$, $\theta_y$, $\theta_z$ Euler angle terms, for an inter-transceiver interval of 6 cm, is subsequently applied to the moving image by the transform edges **1014**B8 block. This transformed image is then subjected to the Find Closest Points on Fixed Image block **1014**C2, similar in operation to the block **1148** of **FIG. 16**. Thereafter, a new transform is determined in block **1014**C4, and the new transform is queried for convergence at decision diamond **1014**C8. If conversion is attained, the RigidRegistration **1014** is complete at terminus **1014**C10. Alternatively, if conversion is not attained, then a return to the transform edges block **1014**B8 occurs to start another iterative cycle.

[0238] The RigidRegistration block **1014** typically converges in less than 20 iterations. After applying the initial transformation, the entire registration process is performed in case there are any overlapping segmented regions between any two images. Similar to the process described in connection with **FIG. 16**, an overlap threshold of approximately 20% is currently set as an input parameter.

[0239] **FIG. 23** is a 4-panel image set that shows the effect of multiple iterations of the heat filter applied to an original image. The effect of shock iteration number in progressively blurring and removing speckle from an original image as the number of iterations increases is shown in **FIG. 23**. In this case the heat filter is described by process blocks **1010**A4 and A6 of **FIG. 21**. In this example, an original image of a bladder is shown in panel (a) having visible speckle spread throughout the image. Some blurring is seen with the 10 iteration image in panel (b), followed by more progressive blurring at **50** iterations in panel (c) and **100** iterations in panel (d). As the blurring increases with iteration number, the speckle progressively decreases.

[0240] **FIG. 24** shows the effect of shock filtering and a combination heat-and-shock filtering to the pixel values of the image. The effect of shock iteration number, step sizes, and gradient thresholds on the blurring of a heat filter is seen in ultrasound signal plots (a) and (b) of **FIG. 24**. Signal plot (a) depicts a smoothed or blurred signal gradient as a sigmoidal long dashed line that is subsequently shock filtered. As can be seen by the more abrupt or steep stepped signal plots after shock filtering, the magnitude of the shock filtered signal (short dashed line) approaches that of the original signal (solid line) without the choppy or noisy pattern associated with speckle. For the most part there is virtually a complete overlap of the shock filtered signal with the original signal through the pixel plot range.

[0241] Similarly, ultrasound signal plot (b) depicts the effects of applying a shock filter to a noisy (speckle rich) signal line (sinuous long dash line) that has been smooth or blurred by the heat filter (short dashed line with sigmoidal appearance). In operation the shock filter results in a generally de-blurring or sharpening of the edges of the image that were previously blurred. Adjacent with, but not entirely overlapping with the original signal (solid line) throughout the pixel plot range, the shock filtered plot substantially overlaps the vertical portion of the original signal, but is elevated in the low and high pixel ranges. Like in (a), a more abrupt or steep stepped signal plot after shock filtering is obtained without significant removal of speckle. Generally dependent on the gradient threshold, step size, and iteration number imposed by block **1010**A10 upon shock block **1010**A8, different overlapping levels of the shock filtered line to that of the original are obtained.

[0242] **FIG. 25** is a 7-panel image set generated by the image enhancement and segmentation algorithms of **FIG. 21**. Panel (a) is an image of the original uterine image. Panel (b) is the image that is produced from the image enhancement processes primarily described in blocks **1010**A4-6 (heat filters) and blocks **1010**A8-10 (shock filters) of **FIG. 21**. Panel (c) shows the effects of the processing obtained from blocks **1010**B2-4 (Estimate Shadow and Fetal Body Regions/Body Threshold). Panel (d) is the image when processed by the Intensity-Based Segmentation Block Group **1010**B2-8. Panel (e) results from application of the Edge-Based Segmentation Block Group **1010**C2-6. Thereafter, the two Intensity-based and Edge-based block groups are combined (combining block **1010**D2) to result in the image shown in panel (f). Panel (g) illustrates the effects of the blocks In-plane and Out-of-plane opening and closing processing blocks **1010**D4-8.

[0243] **FIG. 26** is a pixel difference kernel for obtaining X and Y derivatives to determine pixel gradient magnitudes for edge-based segmentation. As illustrated, a simplest case convolution is obtained for a first derivative computation where $K_x$ and $K_y$ are convolution constants.

[0244] **FIG. 27** is a 3-panel image set showing the progressive demarcation or edge detection of organ wall interfaces arising from edge-based segmentation algorithms. Panel (a) is the enhanced input image. Panel (b) is the image result when the enhanced input image is subjected to the spatial gradients block **1010**C2. Panel (c) is the image result when the enhanced and spatial gradients **1010**C2 processed image is further processed by the threshold of gradients process block **1010**C4.

[0245] Demonstrations of the algorithmic manipulation of pixels of the present invention are provided in Appendix 1: Examples of Algorithmic Steps. Source code of the algorithms of the present invention is provided in Appendix 2: Matlab Source Code.

[0246] While the preferred embodiment of the invention has been illustrated and described, as noted above, many changes can be made without departing from the spirit and scope of the invention. For example, other uses of the invention include determining the areas and volumes of the

prostate, heart, bladder, and other organs and body regions of clinical interest. Similarly, while the preferred sequence of steps and sub-steps (e.g., algorithms) have been described, alternate sequences and additional or fewer steps can be utilized in alternate embodiments. Accordingly, the scope of the invention is not limited by the disclosure of the preferred embodiment.

Appendix 1: Examples of Algorithmic Steps

EXAMPLE IMAGE

[**0247**] The FIG. A below shows an example image on which some of the algorithmic steps are demonstrated. The size of this image is 20 rows by 20 columns.

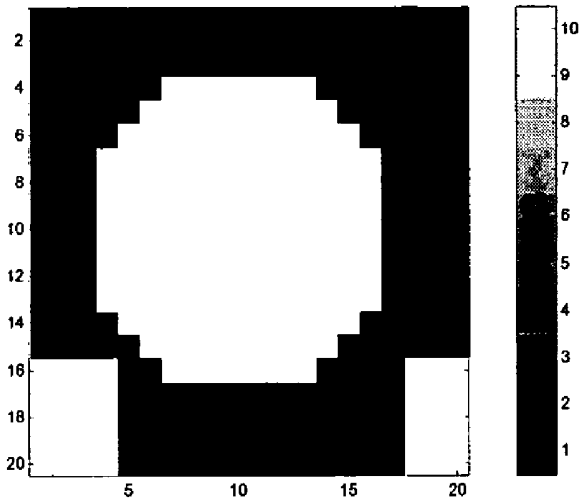


Figure A: Example input image with 20 rows and 20 columns.

[0248] The image shown above is represented as a matrix of numbers and can also be displayed in 20×20 matrix form where the black pixels on the image have a number zero and white pixels have a number 10 in this case:

| | | | | | | | | | | | | | | | | | | | |
|---|---|---|---|---|---|---|---|---|---|---|---|---|---|---|---|---|---|---|---|
| 0 | 0 | 0 | 0 | 0 | 0 | 0 | 0 | 0 | 0 | 0 | 0 | 0 | 0 | 0 | 0 | 0 | 0 | 0 | 0 |
| 0 | 0 | 0 | 0 | 0 | 0 | 0 | 0 | 0 | 0 | 0 | 0 | 0 | 0 | 0 | 0 | 0 | 0 | 0 | 0 |
| 0 | 0 | 0 | 0 | 0 | 0 | 0 | 0 | 0 | 0 | 0 | 0 | 0 | 0 | 0 | 0 | 0 | 0 | 0 | 0 |
| 0 | 0 | 0 | 0 | 0 | 0 | 10 | 10 | 10 | 10 | 10 | 10 | 10 | 0 | 0 | 0 | 0 | 0 | 0 | 0 |
| 0 | 0 | 0 | 0 | 0 | 10 | 10 | 10 | 10 | 10 | 10 | 10 | 10 | 10 | 0 | 0 | 0 | 0 | 0 | 0 |
| 0 | 0 | 0 | 0 | 10 | 10 | 10 | 10 | 10 | 10 | 10 | 10 | 10 | 10 | 10 | 0 | 0 | 0 | 0 | 0 |
| 0 | 0 | 0 | 10 | 10 | 10 | 10 | 10 | 10 | 10 | 10 | 10 | 10 | 10 | 10 | 10 | 0 | 0 | 0 | 0 |
| 0 | 0 | 0 | 10 | 10 | 10 | 10 | 10 | 10 | 10 | 10 | 10 | 10 | 10 | 10 | 10 | 0 | 0 | 0 | 0 |
| 0 | 0 | 0 | 10 | 10 | 10 | 10 | 10 | 10 | 10 | 10 | 10 | 10 | 10 | 10 | 10 | 0 | 0 | 0 | 0 |
| 0 | 0 | 0 | 10 | 10 | 10 | 10 | 10 | 10 | 10 | 10 | 10 | 10 | 10 | 10 | 10 | 0 | 0 | 0 | 0 |
| 0 | 0 | 0 | 10 | 10 | 10 | 10 | 10 | 10 | 10 | 10 | 10 | 10 | 10 | 10 | 10 | 0 | 0 | 0 | 0 |
| 0 | 0 | 0 | 10 | 10 | 10 | 10 | 10 | 10 | 10 | 10 | 10 | 10 | 10 | 10 | 10 | 0 | 0 | 0 | 0 |
| 0 | 0 | 0 | 10 | 10 | 10 | 10 | 10 | 10 | 10 | 10 | 10 | 10 | 10 | 10 | 10 | 0 | 0 | 0 | 0 |
| 0 | 0 | 0 | 10 | 10 | 10 | 10 | 10 | 10 | 10 | 10 | 10 | 10 | 10 | 10 | 10 | 0 | 0 | 0 | 0 |
| 0 | 0 | 0 | 0 | 10 | 10 | 10 | 10 | 10 | 10 | 10 | 10 | 10 | 10 | 10 | 0 | 0 | 0 | 0 | 0 |
| 0 | 0 | 0 | 0 | 0 | 10 | 10 | 10 | 10 | 10 | 10 | 10 | 10 | 10 | 0 | 0 | 0 | 0 | 0 | 0 |
| 10 | 10 | 10 | 10 | 0 | 0 | 10 | 10 | 10 | 10 | 10 | 10 | 10 | 0 | 0 | 0 | 0 | 10 | 10 | 10 |
| 10 | 10 | 10 | 10 | 0 | 0 | 0 | 0 | 0 | 0 | 0 | 0 | 0 | 0 | 0 | 0 | 0 | 10 | 10 | 10 |
| 10 | 10 | 10 | 10 | 0 | 0 | 0 | 0 | 0 | 0 | 0 | 0 | 0 | 0 | 0 | 0 | 0 | 10 | 10 | 10 |
| 10 | 10 | 10 | 10 | 0 | 0 | 0 | 0 | 0 | 0 | 0 | 0 | 0 | 0 | 0 | 0 | 0 | 10 | 10 | 10 |
| 10 | 10 | 10 | 10 | 0 | 0 | 0 | 0 | 0 | 0 | 0 | 0 | 0 | 0 | 0 | 0 | 0 | 10 | 10 | 10 |

[0249] To illustrate some of our algorithms, we also use a noisy version of this example image. To create this image, we added random values to every pixel of the example image and this noisy image is shown in FIG. B.

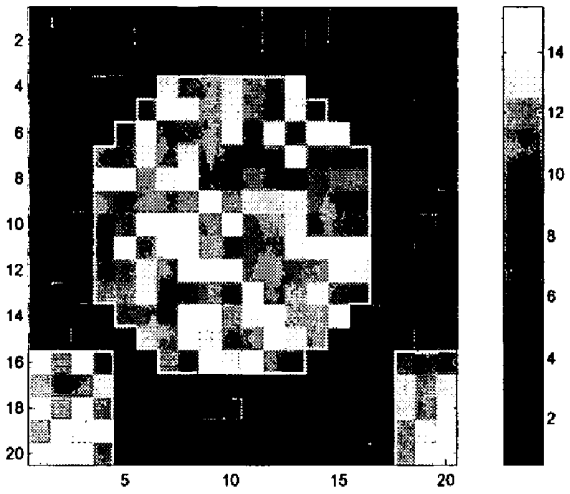


Figure B: Noisy image generated by adding random values to every pixel of the example image shown in Figure A.

[0250] As before, the noisy image is shown as a 20×20 matrix below:

| | | | | | | | | | | | | | | | | | | | |
|---|---|---|---|---|---|---|---|---|---|---|---|---|---|---|---|---|---|---|---|
| 1.4 | 4.1 | 1.1 | 1 | 3 | 0.074 | 2.7 | 0.37 | 3.8 | 0.91 | 4.5 | 0.67 | 3.3 | 0.52 | 4.2 | 2.6 | 4.6 | 2.8 | 0.86 | 1.7 |
| 2 | 0.83 | 3.5 | 2.3 | 4.7 | 1.4 | 3.1 | 0.97 | 3.3 | 2.5 | 4.7 | 0.11 | 4.3 | 0.79 | 4 | 3.6 | 2.8 | 3.8 | 0.65 | 2.8 |
| 2.5 | 2 | 2.6 | 0.41 | 1.4 | 4.1 | 3.4 | 1.9 | 4.4 | 2.1 | 1.7 | 1.3 | 2.8 | 2 | 3.5 | 2.6 | 3.3 | 3.9 | 1.1 | 0.59 |
| 3.6 | 2.6 | 4.7 | 4.3 | 4.4 | 4.9 | 13 | 11 | 11 | 13 | 12 | 11 | 15 | 2 | 2.3 | 3 | 3.9 | 2.4 | 0.53 | 0.85 |
| 1.5 | 3.6 | 3.6 | 2.8 | 0.51 | 10 | 14 | 14 | 12 | 13 | 12 | 10 | 14 | 10 | 0.41 | 4.8 | 0.53 | 4 | 0.71 | 1.4 |
| 0.56 | 2.8 | 1.1 | 1.6 | 10 | 14 | 10 | 12 | 11 | 15 | 11 | 14 | 11 | 15 | 14 | 4.1 | 0.0054 | 2.4 | 2.3 | 2.8 |
| 2.2 | 2.3 | 2.2 | 12 | 11 | 13 | 12 | 13 | 10 | 11 | 11 | 11 | 14 | 11 | 11 | 12 | 2.7 | 1 | 3.9 | 2.4 |
| 2.3 | 2.2 | 0.86 | 14 | 15 | 13 | 14 | 15 | 10 | 11 | 13 | 10 | 11 | 12 | 12 | 13 | 0.034 | 2.9 | 1.4 | 4.8 |
| 0.073 | 0.44 | 4.8 | 12 | 10 | 11 | 12 | 13 | 14 | 13 | 14 | 14 | 13 | 12 | 10 | 11 | 2.3 | 3.3 | 1.1 | 1.2 |
| 3.3 | 2.2 | 1.8 | 10 | 11 | 14 | 15 | 15 | 12 | 15 | 12 | 13 | 13 | 11 | 12 | 11 | 0.98 | 3.4 | 4.5 | 2.4 |
| 3.6 | 1.8 | 0.25 | 11 | 15 | 11 | 13 | 14 | 12 | 10 | 12 | 11 | 14 | 14 | 14 | 14 | 3.9 | 4.7 | 0.037 | 2.6 |
| 1.4 | 1.5 | 3.8 | 10 | 11 | 14 | 10 | 15 | 15 | 14 | 11 | 12 | 12 | 12 | 14 | 13 | 3.1 | 3.9 | 2.9 | 4 |
| 1.3 | 4.3 | 4.5 | 13 | 12 | 13 | 10 | 11 | 11 | 10 | 14 | 10 | 12 | 14 | 12 | 10 | 0.078 | 3.7 | 2.7 | 0.97 |
| 3.5 | 3.8 | 1.4 | 0.61 | 11 | 11 | 10 | 14 | 14 | 13 | 13 | 14 | 12 | 12 | 14 | 2.8 | 4.5 | 4.3 | 3.3 | 4.5 |
| 3.9 | 4.7 | 1.3 | 2.6 | 3.4 | 13 | 11 | 15 | 13 | 11 | 11 | 14 | 13 | 12 | 2.4 | 2.3 | 3.8 | 5 | 1.6 | 4.6 |
| 15 | 13 | 15 | 11 | 4.8 | 3 | 13 | 11 | 14 | 14 | 15 | 11 | 11 | 2.5 | 2.8 | 4.5 | 4.5 | 13 | 11 | 10 |
| 12 | 10 | 11 | 14 | 3.8 | 3.3 | 2.3 | 0.61 | 2.4 | 1.3 | 3.2 | 2.8 | 0.01 | 0.85 | 3.1 | 1.4 | 3.8 | 13 | 12 | 14 |
| 15 | 13 | 15 | 12 | 3.3 | 0.92 | 3.5 | 3.8 | 5 | 4.7 | 1.1 | 0.8 | 4 | 2.6 | 3.3 | 0.33 | 1.9 | 14 | 11 | 15 |
| 12 | 14 | 14 | 14 | 0.65 | 3.2 | 2.9 | 3.6 | 1.9 | 0.69 | 3.4 | 3 | 2.6 | 3.2 | 3.1 | 2.4 | 1.7 | 12 | 13 | 14 |
| 14 | 15 | 14 | 10 | 0.48 | 0.85 | 2.5 | 3.3 | 2.7 | 2.6 | 3.3 | 1.7 | 1.1 | 0.081 | 3.4 | 4.9 | 2.5 | 13 | 15 | 15 |

Heat Filter—**514**

[0251] The Laplacian (second derivative) of the example image is computed as the sum of the second partial x-derivative and second partial y-derivative of the image:

$$\frac{\partial^2 u}{\partial x^2} + \frac{\partial^2 u}{\partial y^2}.$$

[0252] This Laplacian is the right-hand side of the heat equation E1.

[0253] The Laplacian of the example image is computed and this is shown in FIG. C(**1**). Notice the negative values on the inside of the bright areas and positive values on the outside of the bright areas at the edges of the regions. The Laplacian is zero an pixels far from edges.

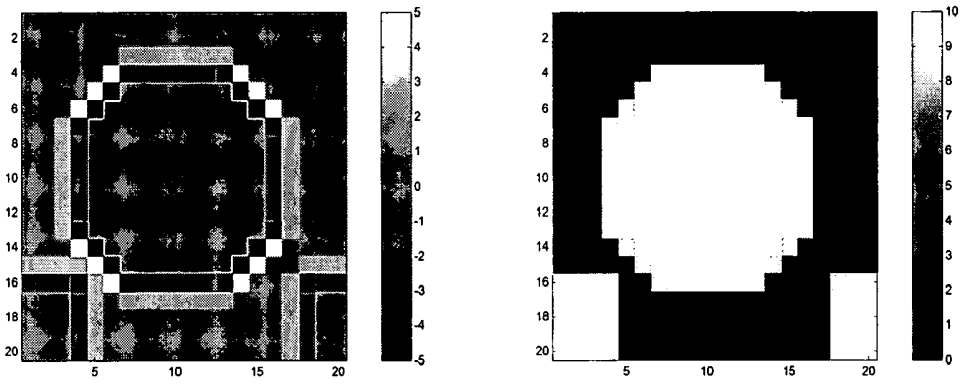


(1) (2)

Figure C (1): The Laplacian of the example image shown in Figure A. (2) The Laplacian added back to the input image.

[0254] When this Laplacian is added back to the input image, after multiplying with a step size parameter, it results in blurring of the edges since the bright areas are reduced in brightness and the dark areas are increased in brightness—this output is shown in FIG. C(2). This is the output of a single iteration of the heat filter. The heat filter outputs after 4 iterations and after 20 iterations are shown in (1) (2)

[0255] FIG. D. Notice the progressive blurring of the image as you apply more iterations.

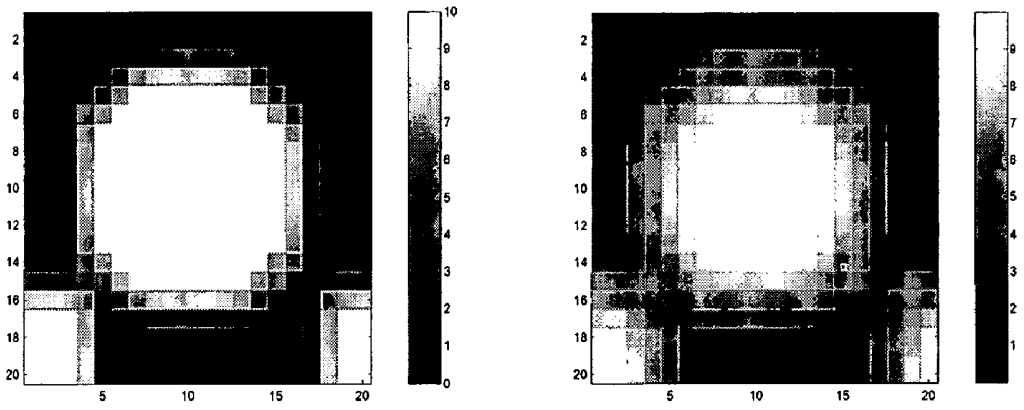


(1) (2)

Figure D: Heat filter outputs after 4 iterations (1) and after 20 iterations (2) on the image shown in Figure A.

[**0256**] Applying 20 iterations of the heat filter to the noisy image from FIG. B results in a reduction of noise and a blurring of the image. This output is shown in FIG. E.

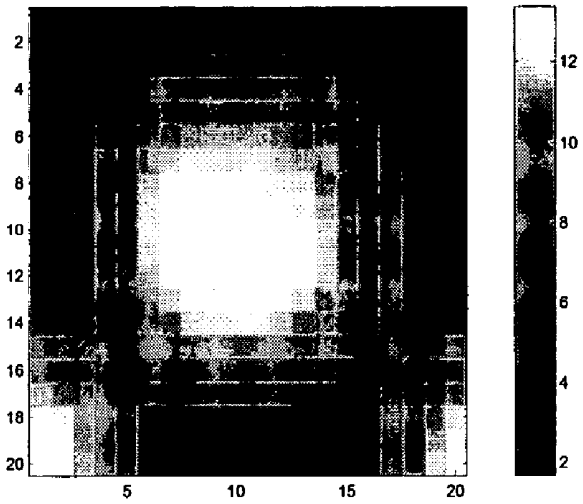


Figure E: The result of applying heat filter to a noisy image.

[0257] Note that in this image, the noise has been significantly removed, although the image is very blurred. This image looks very similar to the heat filtered version of the noiseless image shown in FIG. D(2).

Shock Filter—518

[0258] The application of the shock filtered to the blurred image is shown in FIG. E to sharpen this image. For purposes of the shock filter, the Laplacian of an image (Equation E4) is computed as:

$$l(u)=u_{xx}u_x^2+2u_{xy}u_xu_y+u_{yy}u_y^2.$$

[0259] This is computed for the blurred image and is shown below in shown in FIG. F(1). Again, notice the negative values on the inside of the bright areas and positive values on the outside of the bright areas at the edges of the regions.

[0260] The gradient magnitude of the blurred image (Equation E3) is:

$$\|\nabla u\|=\sqrt{u_x^2+u_y^2}$$

[0261] This is computed for the blurred image and is shown in FIG. F(2) below. Note that the gradient magnitude is highest at the edges and zero in smooth regions.

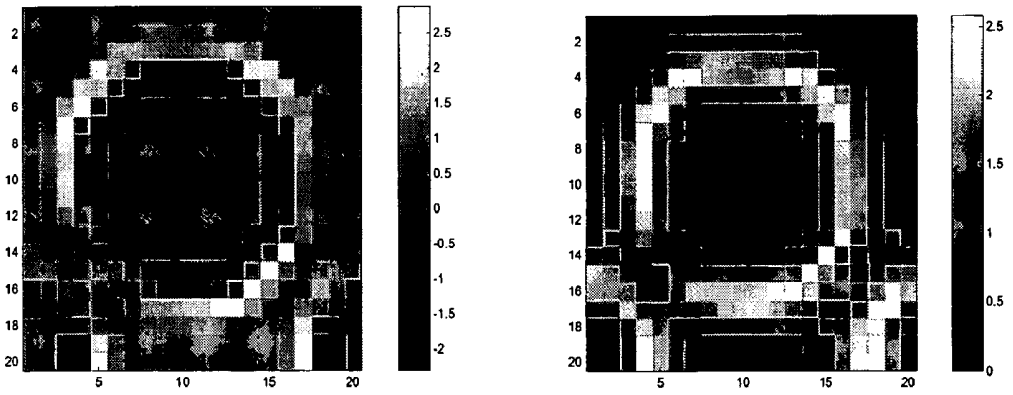


(1) (2)

Figure F (1) The Laplacian of the blurred image. (2) The gradient magnitude of the blurred image.

[0262] Using a threshold value, t, on pixel gradient to be 0.7 we can compute the F function, which is positive where the Laplacian is greater than zero and the gradient magnitude is greater than a threshold, negative where the Laplacian is less than zero and the gradient magnitude is greater than the threshold and zero elsewhere:

$$F(I(u)) = 1, \text{ if } I(u) > 0 \text{ and } \|\nabla u\| > t$$
$$= -1, \text{ if } I(u) < 0 \text{ and } \|\nabla u\| > t$$
$$= 0, \text{ otherwise}$$

[0263] This F image is shown in FIG. G(1) below. Note that as with the Laplacian image, everything outside the original white regions at the edge is 1, everything inside the original white regions at the edge is −1. The boundaries of the original region can be seen as the transition between the negative and the positive F values (the zero crossings).

[0264] Now, the right hand side of the shock filter equation E2, is the negative of the product of the F function image FIG. G(1) and the gradient magnitude image shown in FIG. F(2):

$$-F(I(u))\|\nabla u\|$$

[0265] This right hand side of the shock filter equation is shown in FIG. G(2). If we add this image to the original blurred image we can see that it has the opposite effect of the heat filter. The dark pixels in FIG. G(2) are subtracted from the blurred image and the bright pixels are added to the blurred image basically, thereby making the blurred image more crisp. The addition of this image to the input blurred image is basically what constitutes a single iteration of the shock filter—this addition is shown in FIG. H(1). After 20 iterations, a crisper output as shown in FIG. H(2) is obtained. While this image is not identical to the input noiseless image of FIG. A, it is quite similar to it and much more noise free as compared to the noisy version shown in FIG. B.

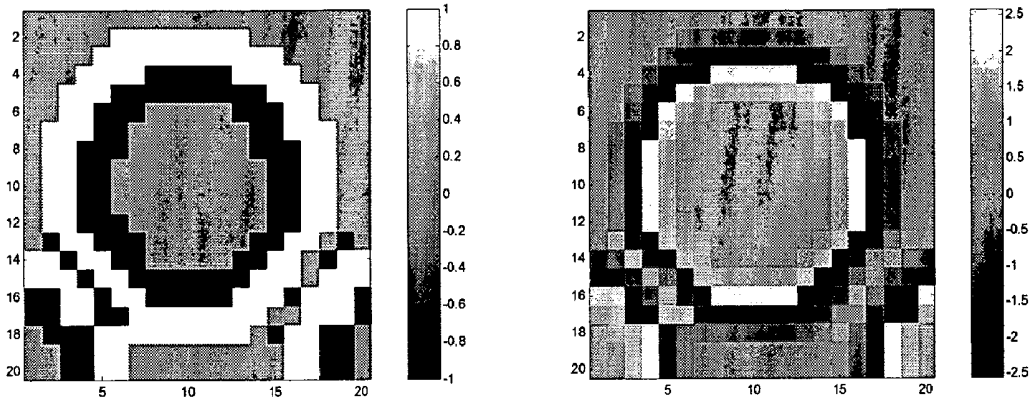

(1) (2)

Figure G: (1) The F function computed from the Laplacian and the gradient. (2) The negative of the product of the F function and the gradient.

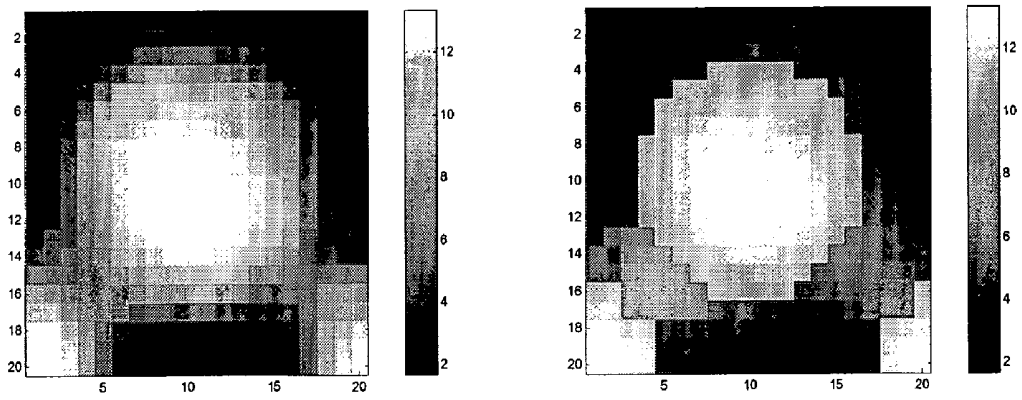

Figure H(1) The output of 1 iteration of the shock filter on the blurred image from Figure E. (2) The output of 20 iterations of the shock filter on the same blurred image.

Intensity Clustering—**422**

[**0266**] In intensity clustering, the enhanced image is subject to the k-means clustering algorithm. In this example, the enhanced image, shown in FIG. H(**2**), is clustered into 4 clusters.

[**0267**] The minimum and maximum intensity values are 1.69 and 13.40. We divide that range into 4 partitions and get the following initial cluster boundaries.

[**0268**] 1.19 4.12 7.04 9.98 13.90

[**0269**] With this partition, all pixels with values between 1.19 and 4.12 are assigned into cluster **1**, all between 4.12 and 7.04 are assigned into cluster **2**, etc. This initial assignment of every pixel to the 4 clusters is shown in FIG. I(**1**). Based on this assignment new cluster centers are found and new partition boundaries found accordingly—after this first iteration, the cluster boundaries move slightly and they are now at:

[**0270**] 1.19 4.08 6.30 9.57 13.90.

[**0271**] In the next iteration, the pixel assignment based on these partition boundaries is shown in **FIG. 1(2)**. Finally, after 6 iterations, the partition boundaries change very little between iterations and are set to:

[**0272**] 1.19 3.65 5.646 9.25 13.90

[**0273**] The final assignment of pixels to the 4 clusters is shown in **FIG. 1(3)**. For this example, the output of the clustering step is the set of pixels assigned to the brightest cluster. This output is shown in **FIG. 1(4)**.

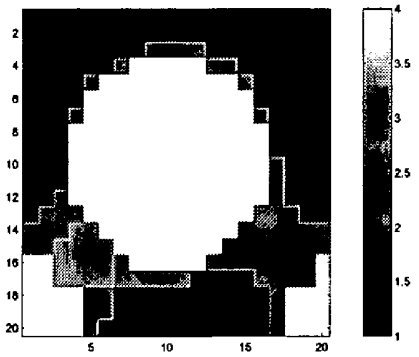
2
4
6
8
10
12
14
16
18
20
5
10
15
20
4
3.5
3
2.5
2
1.5
1

(1)

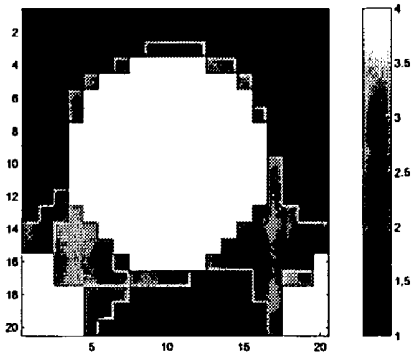
2
4
6
8
10
12
14
16
18
20
5
10
15
20
4
3.5
3
2.5
2
1.5
1

(2)

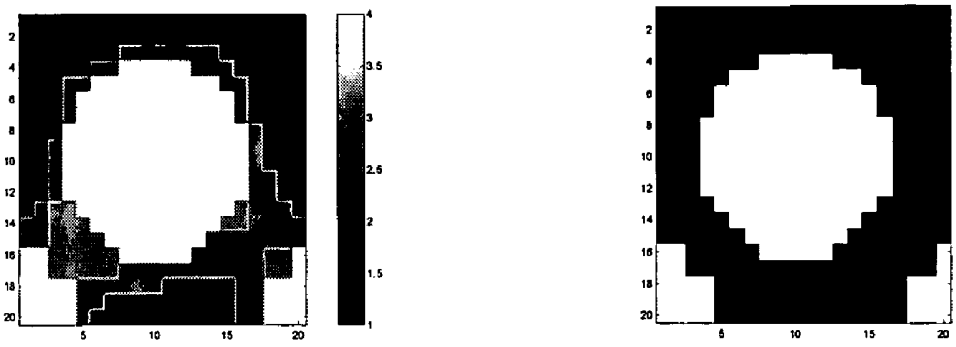

(3) (4)

Figure I: The output of clustering at different iterations of the k-means clustering process. (1) Initial assignment (2) After the first iteration (3) Final assignment after 6 iterations. (4) The one brightest cluster representing the region of interest.

Spatial Gradient—**526**

[**0274**] To compute the gradient magnitude of the enhanced image shown in FIG. H(**2**), the x-derivative $u_x$ and the y-derivative $u_y$ of the image is calculated and then the sum of squares of the two images is calculated to get the gradient magnitude—$\|\nabla u\|=\sqrt{u_x^2+u_y^2}$. The x- and y-derivatives and the gradient magnitudes of the enhanced image are shown in FIG. J.

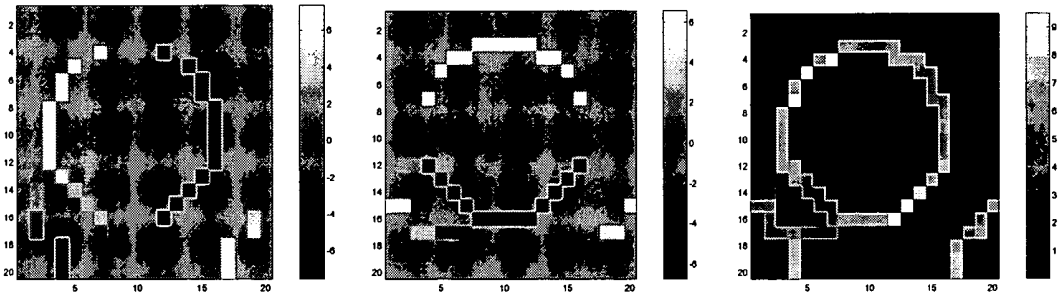

(1) (2) (3)

Figure J: Spatial gradients of the image shown in Figure H(2): (1) x-derivative of image (2) y-derivative of image (3) gradient magnitude of image.

Hysteresis Threshold—**530**

[**0275**] In the hysteresis threshold, two threshold values based on the percentage of non-edge pixels desired and the ratio of the two thresholds is determined. In this example, the percentage non-edge pixels desired is set to 90% and the lower to upper threshold ratio is set to 0.5.

[**0276**] The upper threshold is first computed by looking at the histogram and the cumulative histogram of the gradient magnitude image shown in FIG. J(**3**). The histogram of the gradient magnitude image is shown in FIG. K(**1**). The histogram shows the count of pixels of different gradient values on the image. The cumulative histogram calculated by cumulatively adding up the bins of the histogram is shown in FIG. K(**2**). The cumulative histogram shows the count of all pixels less than a given value in the gradient magnitude image. The horizontal line shown in FIG. K(**2**) corresponds to a y-value of 90% of the image pixels (0.90*20*20=360). The intersection of this line with the cumulative histogram gives the threshold at which 90% of the image pixels will be marked as non-edge and 10% will be marked as edge. From the graph, we can see that a threshold of **7** satisfies that condition. The lower threshold is set to 0.5 times the upper threshold of **7**, which gives 3.5.

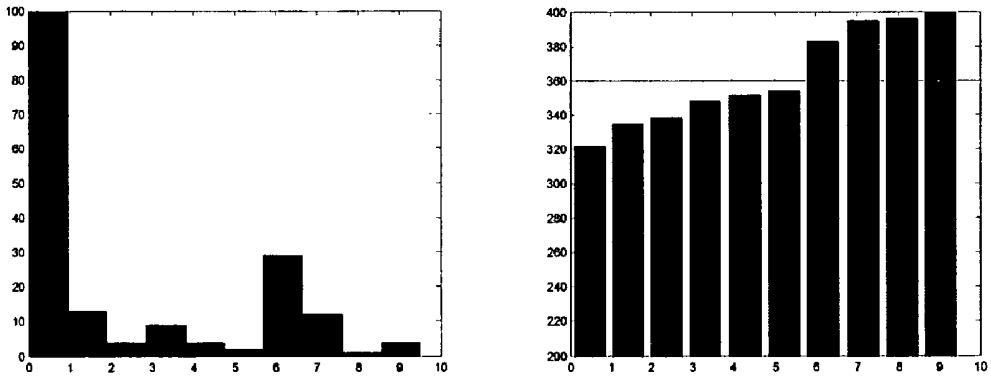


Figure K: Histogram and cumulative histogram of the gradient magnitude image.

[**0277**] For the hysteresis threshold, the threshold of the image at the two threshold values of 3.5 and at 7 is set and then all edge segments from the lower threshold image is selected that have at least one higher threshold pixel. The two thresholded images and the output of the Hysteresis threshold step are shown in FIG. L. In this example, note that one edge segment—(row **15**, column **2**) has no pixel greater than the higher threshold and is therefore removed from the output. All other edge segments from FIG. L(**1**) are retained in the output.

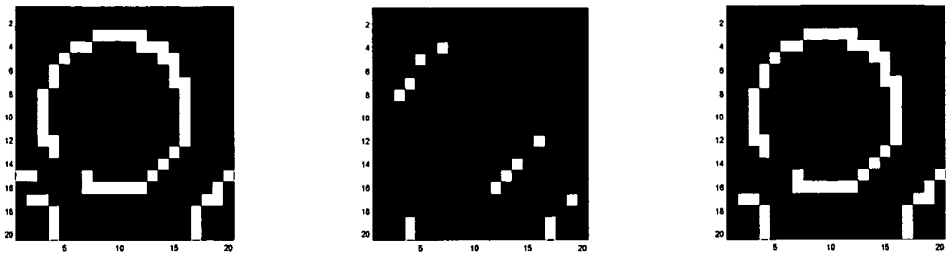

(1) (2) (3)

Figure L: (1) Gradient image thresholded at 3.5 – all pixels greater than 3.5 are shown as white (2) gradient image thresholded at 7, (3) Output of hysteresis threshold.

Matching Edges Filter—**538**

[**0278**] The matching edges filter selects pairs of matching edges from among all the edges found by the hysteresis threshold step (FIG. L(**3**)). The y-derivative image, shown in FIG. J(**2**) is used in this step to help find the vertical matching edges. The matching edges found by this step of the algorithm are shown in FIG. M(**1**) and the filled region between the leading the trailing edges are shown in FIG. M(**2**). Note that this step gets rid of edges of regions on the periphery of the image since it cannot find matching trailing edges for those regions. Also, note that in the output filled image we have some unfilled lines where the gradient was primarily horizontal or where the matching edges did not exist.

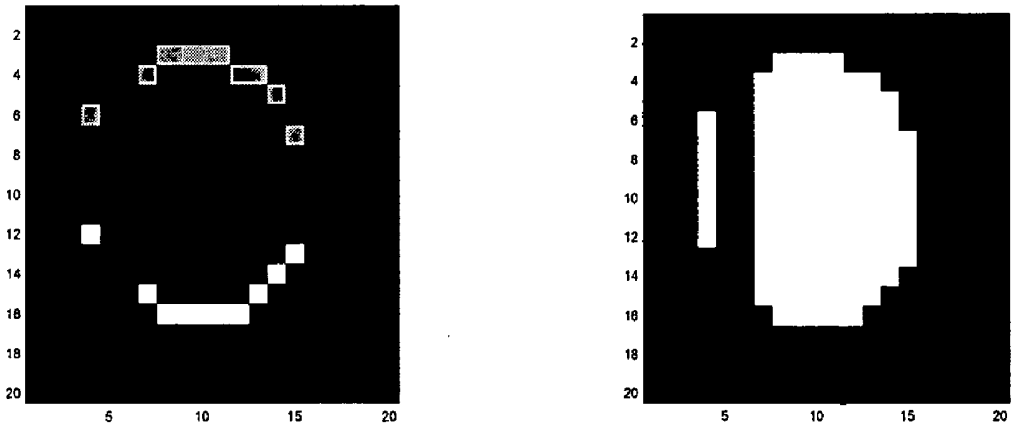


(1) (2)

Figure M: (1) Matching edges found by the algorithm – leading edges shown in gray and lagging edges shown in white. (2) The region between the leading the lagging edges filled by white pixels.

And Images—**442**

[**0279**] The two images shown in **FIG. 1(4)** and FIG. M(**2**) represent the segmentation of the input noisy image shown in FIG. B. Neither of them represents a perfect output. The region-based algorithm finds extraneous regions while the edge-based algorithm misses part of the desired region. The two images are combined using a Boolean AND operator and the output is shown in FIG. N.

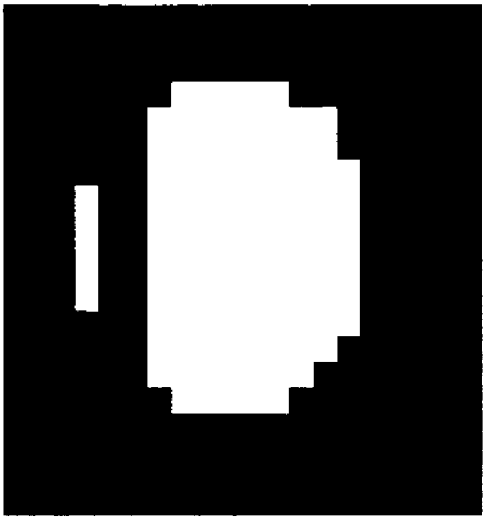

Figure N: Combining the region-based and edge-based segmentation.

Close And Open—**546** & **550**

[**0280**] Using a structuring element shaped like a line of width 5 pixels, we close the output of AND images and this gives us a single region representing the structure of interest as shown in FIG. O.

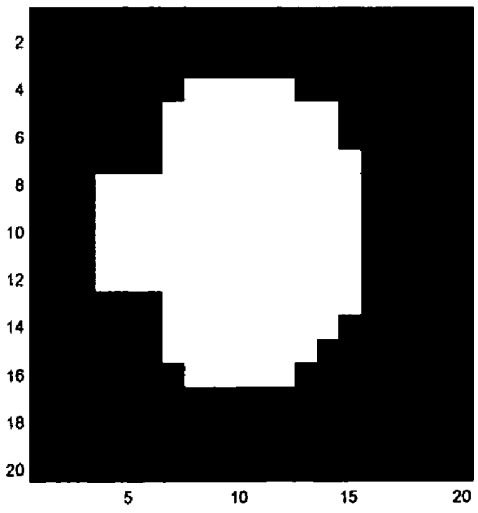


Figure O: Result of closing the image from Figure N.

[**0281**] Opening this image does not change the result—however, FIG. P shows an example of opening on another image. The input image, FIG. P(**1**), contains two regions, one large region and one small region. The large region is 10 pixels in width and height while the small region is 4 pixels in width and height. Using a structuring element shaped like a line of length 5 pixels and applying morphological opening to the input image results in an image shown in FIG. P(**2**) where the smaller region whose width was smaller than the structuring element was removed from the image.

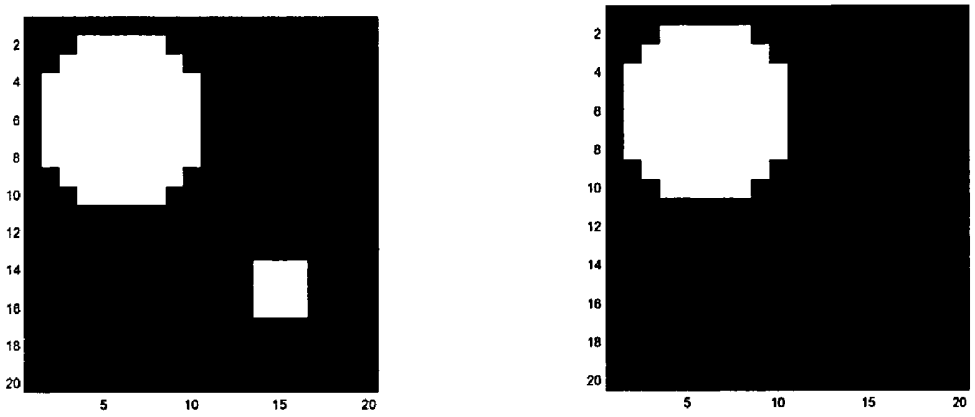


(1) (2)

Figure P: (1) Input image containing two foreground regions. (2) Output image after opening where the smaller region was removed because it was smaller than the structuring element.

Filter Deep Regions—**554**

[**0282**] This filtering step is used to remove regions from a segmented image that start at a location deeper than a user specified depth threshold. This filtering is illustrated in FIG. Q, where the input image contains two regions—one region starts at row **2** and the other region starts at row **14**. For each region on the input image, the starting row is determined after doing a connected component labeling—then using a depth threshold of 12, the regions where the starting row depth is greater than the depth threshold are removed from the input

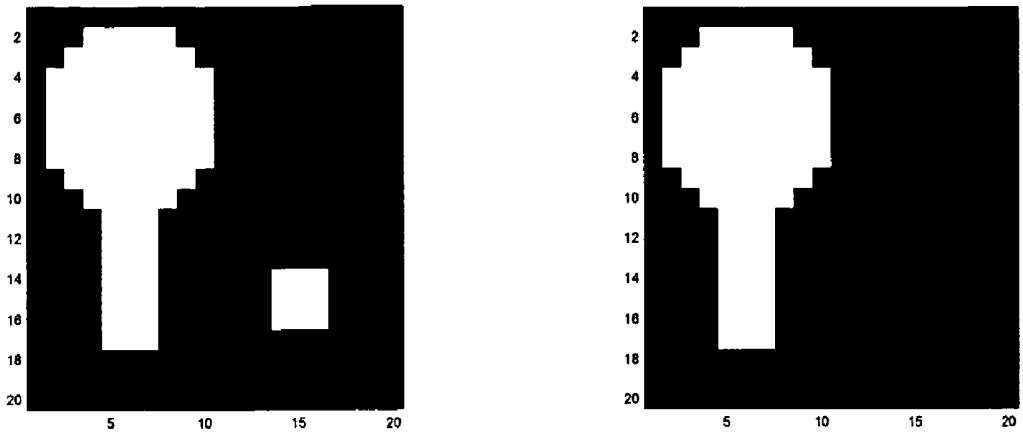


Figure Q: (1) Input image containing two foreground regions. (2) Output image after removing the region whose starting row is greater than the depth threshold of 12.

[0283] Head Diameter Range—**730**

[0284] For a gestational age of 20 weeks, the bi-parietal diameter (BPD) is typically 46 mm. The calculated Head Diameter search range, which ranges from −30% to +30% of the typical BPD value, is found to be:

| | | | | | | |
|---|---|---|---|---|---|---|
| 32.2 | 36.8 | 41.4 | 46.0 | 50.6 | 55.2 | 59.8 |

[0285] For a gestational age of 36 weeks, the bi-parietal diameter (BPD) is typically 88 mm. The calculated Head Diameter search range, which ranges from −30% to +30% of the typical BPD value, is found to be:

| | | | | | | |
|---|---|---|---|---|---|---|
| 61.6 | 70.4 | 79.2 | 88.0 | 96.8 | 105.6 | 114.4 |

Polar Hough Transform—**738**

[0286] To illustrate the polar Hough transform, an exemplary image is generated of a circle in the Cartesian coordinates using the circle equations, E5. This circle image was then dilated to result in a disk like shape and then a few rows of data were set to zero. This input image is shown in FIG. R(**1**). The goal of the circular Hough transform is to find the circle that best fits the white pixels in this input image.

[0287] Next, this Cartesian input image was converted to polar domain by inverse scan conversion and the resulting image is shown in FIG. R(**2**). To this polar coordinate image, the polar Hough transform for a circle was applied, where for each white pixel on the image a polar circle of a known radius was drawn. The output of the Hough transform is the sum of all such circles and this is shown in FIG. R(**3**). The center of the best-fit circle has the most points passing through it. So, to determine the best-fit circle, we simply found the pixel on the Hough output with the maximum value. The point with the maximum value represents the center of the best-fit circle.

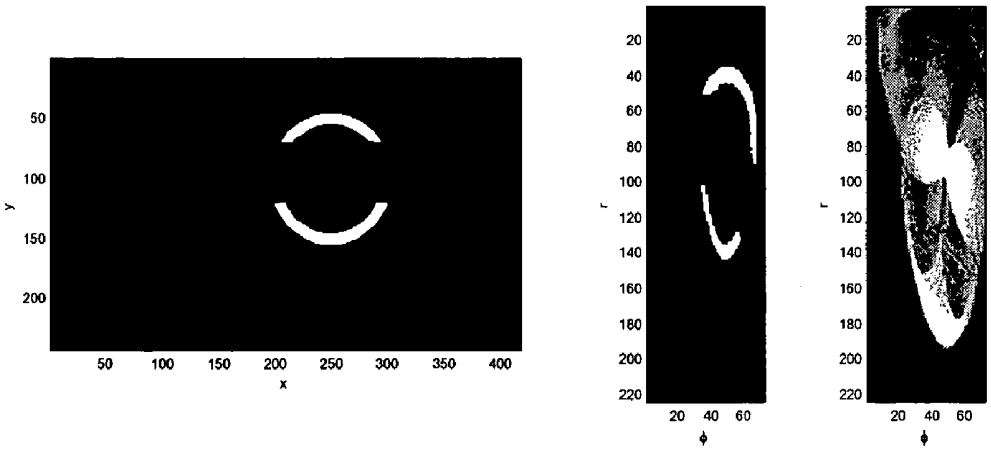


(1) (2) (3)

Figure R: (1) The input Cartesian coordinate partial circle (2) The partial circle converted to polar coordinates, (3) The Hough transform output showing the sum of polar circles drawn around each white pixel of the input image.

[0288] The best-fit circle determined by this Hough transform procedure is overlaid on the polar coordinate image and the Cartesian coordinate image and the two drawings are shown in FIG. S.

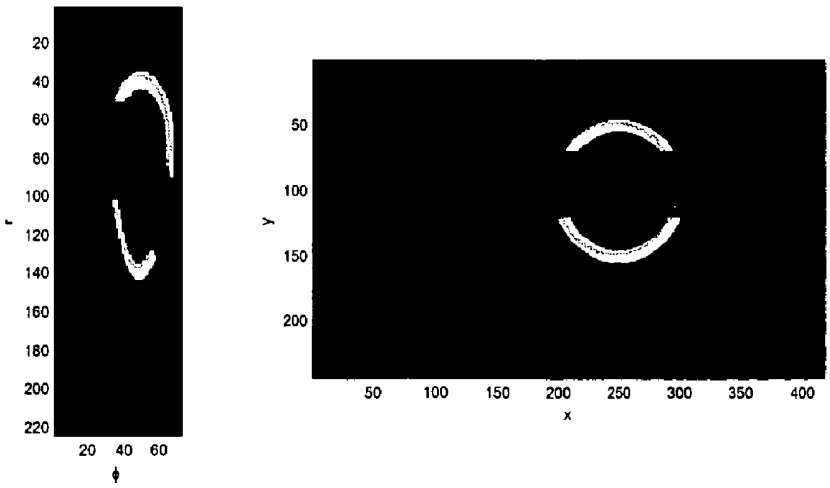


Figure S: The best fit circle found using a Polar coordinate Hough transform (1) overlaid on the polar

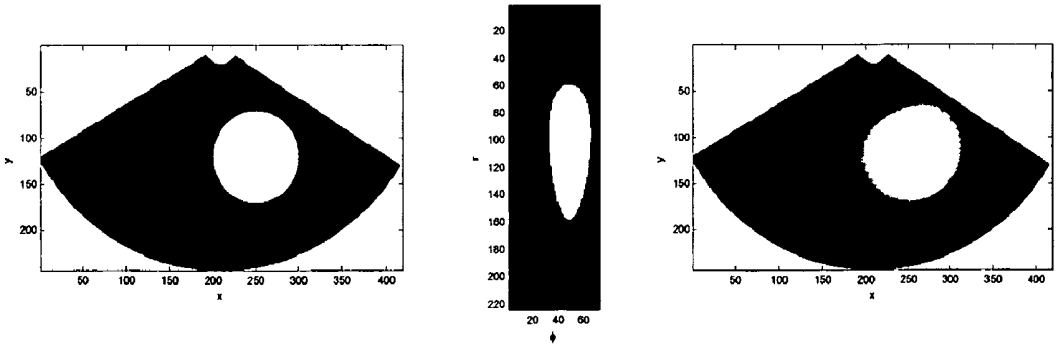


(1) (2) (3)

Fill Circle Region—**746**

[**0289**] A circle region in Cartesian space has a somewhat different shape in the Polar coordinate space. To illustrate this polar coordinate circle, we use both Cartesian coordinate and polar coordinate circles. First, a Cartesian coordinate circle of radius 50 pixels and a center (**120,250**) is drawn using the circle equation, E5, $(x-x_0)^2+(y-y_0)^2=R^2$—this circle is shown in FIG. T(**1**).

[**0290**] Now, the Cartesian center coordinates $(x_0,y_0)$ are converted from Cartesian to polar center $(r_0, \phi_0)$ using the scan conversion equations:

$r_0^2=(x_0^2+y_0^2)$,

$\phi_0=\tan^{-1}(y_0/x_0)$

[**0291**] Next, the polar coordinate circle drawing and filling equation, E6, $(r \sin\phi-r_0\sin\phi_0)2+(r \cos\phi-r_0\cos\phi_0)^2=R^2$,

[**0292**] is applied to draw and fill the same circle of radius R=50, in polar coordinates. This circle in the polar coordinates is shown in FIG. T(**2**).

[**0293**] Finally, to verify that this polar coordinate circle in indeed a representation of the Cartesian coordinate circle, the polar circle image is scan-converted to generate the representative Cartesian coordinate circle image. This scan-converted circle is shown in FIG. T(**3**). Comparing FIG. T(**1**) and FIG. T(**3**), it can be seen that while the two circles are not identical, they are fairly similar. The differences are due to the fact that the polar coordinate data cannot represent Cartesian data completely.

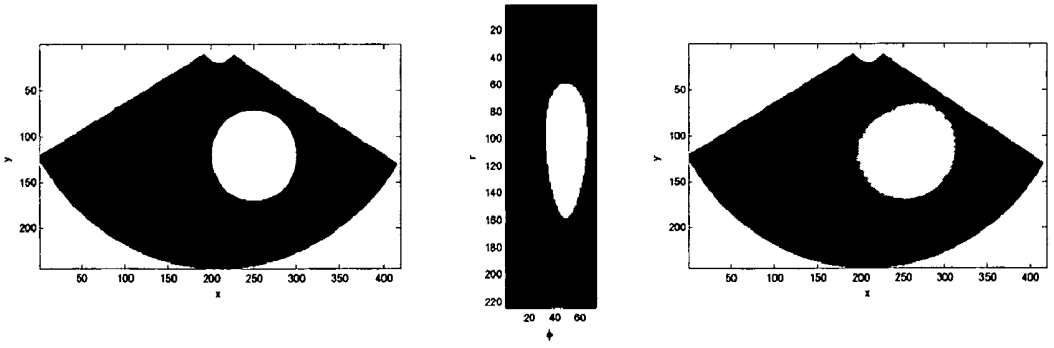


(1) (2) (3)

Figure T Polar coordinate circle filling. (1) A filled circle in a Cartesian coordinate image (2) The equivalent filled circle in polar coordinate image, (3) The scan converted polar coordinate filled circle image.

We claim:

1. A method to determine amniotic fluid volume in digital images, the method comprising:

positioning an ultrasound transceiver to probe a first portion of a uterus of a patient, the transceiver adapted to obtain a first plurality of scanplanes;

re-positioning the ultrasound transceiver to probe a second portion of the uterus to obtain a second plurality of scanplanes;

enhancing the images of the amniotic fluid regions in the scanplanes with a plurality of algorithms;

registering the scanplanes of the first plurality with the second plurality;

associating the registered scanplanes into a composite array, and

determining the amniotic fluid volume of the amniotic fluid regions within the composite array.

2. The method of claim 1, wherein plurality of scanplanes are acquired from a rotational array, a translational array, or a wedge array.

3. The method of claim 1, wherein the plurality of algorithms includes algorithms for image enhancement, segmentation, and polishing.

4. The method of claim 3, wherein segmentation further includes an intensity clustering step, a spatial gradients step, a hysteresis threshold step, a Region-of-Interest selection step, and a matching edges filter step.

5. The method of claim 4, wherein the intensity clustering step is performed in a first parallel operation, and the spatial gradients, hysteresis threshold, Region-of-Interest selection, and matching edges filter steps are performed in a second parallel operation, and further wherein the results from the first parallel operation are combined with the results from the second parallel operation.

6. The method of claim 3, wherein image enhancement further includes applying a heat filter and a shock filter to the digital images.

7. The method of claim 6 wherein the heat filter is applied to the digital images followed by application of the shock filter to the digital images.

8. The method of claim 1, wherein the amniotic fluid volume is adjusted for underestimation or overestimation.

9. The method of claim 8, wherein the amniotic fluid volume is adjusted for underestimation by probing with adjustable ultrasound frequencies to penetrate deep tissues and to repositioning the transceiver to establish that deep tissues are exposed with probing ultrasound of sufficient strength to provide a reflecting ultrasound echo receivable by the transceiver, such that more than one rotational array to detect deep tissue and regions of the fetal head are obtained.

10. The method of claim 8, wherein amniotic fluid volume is adjusted for overestimation by automatically determining fetal head volume contribution to amniotic fluid volume and deducting it from the amniotic fluid volume.

11. The method of claim 10, wherein the steps to adjust for overestimated amniotic fluid volumes include a 2D clustering step, a matching edges step, an all edges step, a gestational age factor step, a head diameter step, an head edge detection step, and a Hough transform step.

12. The method of claim 12, wherein the Hough transform step includes a polar Hough Transform step, a Find Maximum Hough value step, and a fill circle region step.

13. The method of claim 12, wherein the polar Hough Transform step includes a first Hough transform to look for lines of a specified shape, and a second Hough transform to look for fetal head structures.

14. The method of claim 1, wherein the positions include lateral and transverse.

15. A method to determine amniotic fluid volume in digital images, the method comprising:

positioning an ultrasound transceiver to probe a first portion of a uterus of a patient, the transceiver adapted to obtain a first plurality of scanplanes;

re-positioning the ultrasound transceiver to probe a second and a third portion of the uterus to obtain a second and third plurality of scanplanes;

enhancing the images of the amniotic fluid regions in the scanplanes with a plurality of algorithms;

registering the scanplanes of the first plurality through the third plurality;

associating the registered scanplanes into a composite array, and

determining the amniotic fluid volume of the amniotic fluid regions within the composite array.

16. A method to determine amniotic fluid volume in digital images, the method comprising:

positioning an ultrasound transceiver to probe a first portion of a uterus of a patient, the transceiver adapted to obtain a first plurality of scanplanes;

re-positioning the ultrasound transceiver to probe a second through fourth portion of the uterus to obtain a second through fourth plurality of scanplanes;

enhancing the images of the amniotic fluid regions in the scanplanes with a plurality of algorithms;

registering the scanplanes of the first through fourth plurality;

associating the registered scanplanes into a composite array, and

determining the amniotic fluid volume of the amniotic fluid regions within the composite array.

17. A method to determine amniotic fluid volume in digital images, the method comprising:

positioning an ultrasound transceiver to probe a first portion of a uterus of a patient, the transceiver adapted to obtain a first plurality of scanplanes;

re-positioning the ultrasound transceiver to probe a second through fifth portion of the uterus to obtain a second through fifth plurality of scanplanes;

enhancing the images of the amniotic fluid regions in the scanplanes with a plurality of algorithms;

registering the scanplanes of the first through the fifth plurality;

associating the registered scanplanes into a composite array, and determining the amniotic fluid volume of the amniotic fluid regions within the composite array.

**18**. A system for determining amniotic fluid volume, the system comprising:

a transceiver positioned from two to six locations of a patient, the transceiver configured to deliver radio frequency ultrasound pulses to amniotic fluid regions of a patient, to receive echoes of the pulses reflected from the amniotic fluid regions, to convert the echoes to digital form, and to obtain a plurality of scanplanes in the form of an array for each location;

a computer system in communication with the transceiver, the computer system having a microprocessor and a memory, the memory further containing stored programming instructions operable by the microprocessor to associate the plurality of scanplanes of each array, and

the memory further containing instructions operable by the microprocessor to determine the presence of an amniotic fluid region in each array and determine the amniotic fluid volume in each array.

**19**. The system of claim 18, wherein the array includes rotational, wedge, and translation.

**20**. The system of claim 18, wherein stored programming instructions further include aligning scanplanes having overlapping regions from each location into a plurality of registered composite scanplanes.

**21**. The system of claim 20, wherein the stored programming instructions further include fusing the registered composite scanplanes amniotic fluid regions of the scanplanes of each array.

**22**. The system of claim 21 wherein the stored programming instructions further include arranging the fused composite scanplanes into a composite array.

**23**. The system of claim 18, wherein the computer system is configured for remote operation via a local area network or an Internet web-based system, the internet web-based system having a plurality of programs that collect, analyze, and store amniotic fluid volume.

* * * * *

| | | | |
|---|---|---|---|
| 专利名称(译) | 基于3D超声的仪器，用于非侵入性测量羊水量 | | |
| 公开(公告)号 | US20050251039A1 | 公开(公告)日 | 2005-11-10 |
| 申请号 | US11/119355 | 申请日 | 2005-04-29 |
| [标]申请(专利权)人(译) | CHALANA VIKRAM<br>DUDYCHA STEPHEN<br>MCMORROW GERALD | | |
| 申请(专利权)人(译) | CHALANA VIKRAM<br>DUDYCHA STEPHEN<br>MCMORROW GERALD | | |
| 当前申请(专利权)人(译) | VERATHON INC. | | |
| [标]发明人 | CHALANA VIKRAM<br>DUDYCHA STEPHEN<br>MCMORROW GERALD | | |
| 发明人 | CHALANA, VIKRAM<br>DUDYCHA, STEPHEN<br>MCMORROW, GERALD | | |
| IPC分类号 | A61B5/00 A61B8/00 A61B8/08 A61B8/12 A61B8/14 G06T5/00 G06T7/60 | | |
| CPC分类号 | A61B5/204 G06T2207/30044 A61B8/0858 A61B8/0866 A61B8/14 A61B8/4472 A61B8/483 A61B8/565 G01S7/52065 G01S15/8993 G06K9/32 G06K9/34 G06K2209/05 G06T7/0012 G06T7/0083 G06T7/0087 G06T7/0091 G06T7/602 G06T2207/10136 G06T2207/20061 G06T2207/30004 A61B5/4343 G06T7/12 G06T7/143 G06T7/155 G06T7/62 | | |
| 优先权 | 60/470525 2003-05-12 US<br>60/566823 2004-04-30 US<br>60/400624 2002-08-02 US<br>60/423881 2002-11-05 US | | |
| 其他公开文献 | US7520857 | | |
| 外部链接 | Espacenet USPTO | | |


摘要(译)

公开了一种手持式3D超声仪器，其用于非侵入性地且自动地测量子宫中的羊水量，需要最少的操作者干预。使用2D图像处理算法，仪器向用户自动反馈获取3D图像集的位置。用户获取覆盖子宫中所有羊水的一个或多个3D数据集，然后使用优化的3D算法处理该数据，以输出针对任何胎儿脑头体积贡献校正的总羊水量。